Optical Dating of Tsunami Deposits

by

Marc René Baril
B.Sc., University of Toronto, 1994

A THESIS SUBMITTED IN PARTIAL FULFILLMENT
OF THE REQUIREMENTS FOR THE DEGREE OF
MASTER OF SCIENCE
in the Department
of
Physics

SIMON FRASER UNIVERSITY
February 1997

APPROVAL

Name: Marc René Baril

Degree: Master of Science

Title of thesis: Optical Dating of Tsunami Deposits

Examining Committee: Dr. Michael Plischke
Professor, Department of Physics
Chair

Dr. David J. Huntley
Professor, Department of Physics (Supervisor)

Dr. George Kirczenow
Professor, Department of Physics

Dr. Robert F. Frindt
Professor, Department of Physics

Dr. John J. Clague
Senior Research Scientist, Geological Survey of Canada

Date Approved: 17 February 1997

Summary

A tsunami generated by a Cascadia subduction zone earthquake deposited sands in marshes on Vancouver Island and the coast of Washington 300 years ago. Similar deposits were left in marshes on Vancouver Island by the tsunami produced by the 1964 Alaska earthquake. Samples of one or more of these and other sand layers were collected from marshes on Vancouver Island at Fair Harbour, Koprino Harbour, Neroutsos Inlet and Zeballos, and at the Niawiakum River in Washington State. At some sites samples of material considered to be analogous to the source material for the sand layers were also collected.

A new luminescence detection chamber was constructed for the measurement of these young samples and an improvement in detection efficiency over 4 times that of the old chamber was attained.

The two samples collected from Koprino Harbour yielded optical ages of 60±20 years and 270±50 years, consistent with the known ages of 32 and 300 years respectively. The remaining samples all yielded ages considerably older than the independent age estimates. Optical ages for the 300-year-old sands at the remaining sites were: 920±170 years at Fair Harbour, 2100±500 years at Neroutsos Inlet and 540±90 years at the Niawiakum River. The purported 300-year-old tsunami layer at Zeballos yielded an optical age of 11,700±700 years. At Fair Harbour, a sand layer that was probably deposited by a flood less than 500 years ago yielded an optical age of 5300±700 years. Samples of modern tidal-channel sediments at Fair Harbour and Koprino Harbour yielded near-zero equivalent doses. A non-zero equivalent dose was obtained for modern river bottom sediment at the Niawiakum River.

These and previous results indicate that some of the sands received poor exposure to sunlight prior to burial whereas others were sufficiently exposed. The discrepancy is probably due to the differing depth of tsunami scour of the source sediments at different sites. A correlation is also suggested between sites at which anomalously old ages were obtained and the extent of the mud flats fringing the marsh.

Acknowledgements

My foremost thanks are due to my senior supervisor Dr. D. J. Huntley, for his unfailing vision and guidance in bringing this project to fruition. I am particularly grateful for his critical reading of the manuscript in its earlier stages. This project would have been unapproachable without the collaboration of John J. Clague of the Geological Survey of Canada, and Boyd Benson of the Department of Earth Sciences at the University of British Columbia. For their assistance in identifying suitable sample sites, illuminating the geological problems associated with this project, providing transportation and lodging on our Vancouver Island field trip and their undampened good nature in a wet salt-marsh, I am greatly indebted. Special thanks are due to Brian F. Atwater of the U.S. Geological Survey at the University of Washington for his aid in collecting samples at the Niawiakum River, especially in obtaining the channel bottom cores at this site. I am also grateful to George Morariù for his invaluable assistance in preparing the samples and to Dr. Albert Curzon and Ken Myrtle for their generous devotion of time in producing the SEM fluorescence maps. I would also like to thank Michael Short and my other colleagues in the Physics Department for countless instructive and entertaining discussions over the period of my stay at Simon Fraser University.

Dedication

To Pam the potbellied pig,

our most dedicated student of dirt.

Contents

List of Tables

List of Figures

Chapter 1

Introduction

1.1 Overview

Over the past ten years a large body of geological evidence has been accumulating for the occurrence of prehistoric large earthquakes in coastal Oregon, Washington and southern British Columbia. Much of the evidence for these events has been found in coastal marshes where past sudden subsidence is recorded in the stratigraphy as an abrupt transition between a low marsh and high marsh environment. Often, thin sand layers are found at the high/low marsh transitional horizon; these have been interpreted as deposits left by a local tsunami generated at the time of the earthquake-induced subsidence. The most widely observed subsidence event along the west coast occurred around 300 years ago; however, evidence has been found for several other sudden submergence events in the past 5000 years (Shennan *et al.*, 1996; Mathewes and Clague, 1994; Atwater, 1992; Clarke and Carver, 1992; Darienzo and Peterson, 1990). Recurrence intervals for the subsidence events range from a few hundred years to a thousand years, depending on the site at which the submergence is recorded (Atwater *et al.*, 1995).

This work follows up on a pilot study by Huntley and Clague (1996) on the suitability of the optical dating technique for dating the tsunami-laid sediments. In keeping with Huntley and Clague's groundwork, the 3.1 eV luminescence emission

of K-feldspars was measured during 1.4 eV (infrared) excitation. Several new samples of tsunami-laid sands were collected; their geological settings are described in Chapter 2. Due to the youthfulness of the samples, a luminescence detection chamber with improved sensitivity over the existing one was constructed; the design of this chamber is discussed in Chapter 3. The dosimetry calculations are presented in Chapter 4. The luminescence measurements and corresponding optical ages are presented in Chapter 5.

The introduction consists of two parts; the first is a review of the geological setting relevant to this study and provides a broader perspective of the motivation behind this work. The second part is devoted to optical dating with specific emphasis on dating using 1.4 eV (infrared) stimulated luminescence in K-feldspar.

1.2 Geological background

1.2.1 Tectonic setting

Geological evidence collected over the last decade indicates that large prehistoric earthquakes have occurred along the Cascadia subduction zone, a 1000 km long region extending from Cape Mendocino in northern California to central Vancouver Island. In this region the Gorda, Juan de Fuca and Explorer oceanic plates meet the North America plate along a large thrust fault, where oceanic crust is subducted below North America. Geodetic and tide gauge data from Washington (Savage and Lisowski, 1991) as well as GPS[1] monitoring of crustal deformation in southern British Columbia (Dragert and Hyndman, 1995) indicate an accumulation of strain related to locking of the North America and Juan de Fuca plates. The earthquake which would result from the slip of the entire Juan de Fuca plate could affect a length of populated coastline nearly 1000 km long.

The Cascadia subduction zone is peculiar in that, unlike other subduction zones, it has not suffered any great thrust earthquakes within the last 200 years of written history. The Cascadia subduction zone also differs from other subduction regions

[1] Global positioning system

in that it lacks recently uplifted terraces along its coast with the exception of Cape Mendocino in California (West and McCrumb, 1988), central Vancouver Island (Friele and Hutchinson, 1993; Clague *et al.*, 1982) and possibly at Cape Blanco, Oregon (West and McCrumb, 1988; Atwater *et al.*, 1995). This lack of Holocene shoreline uplift features led to some early contention concerning the earthquake-generating potential of the Cascadia subduction-zone (Atwater *et al.*, 1988). Most evidence shows that past subduction-zone earthquakes were accompanied by abrupt subsidence rather than uplift along the Cascadia margin. That this episodic subsidence resulted from large (moment magnitude M_w 8 or greater) earthquakes is now certain, however the extent of the rupture along the locked margin of the subduction zone which could occur during such a quake remains a contested matter. This question is of primary concern in assessing earthquake hazards along the Cascadia margin. A single large rupture of the entire length of the subduction zone would result in a much larger quake than would occur if the slip were to take place during several smaller, temporally extended seismic events.

Coastal subsidence along the margin of the subduction zone may be understood in terms of the simple model sketched in Figure 1.1 (Hyndman and Wang, 1993). During the period of interseismic strain accumulation, land which is some distance inland from the leading edge of the continental plate is thrust upwards whereas the edge of the continental plate, itself, is drawn downwards. This is caused by locking of the subduction zone somewhat inland of this front[2]; motion of the oceanic and continental plates inland from this locked margin is by aseismic slip. Still further inland from the locked region, material in the subducting plate is plastic and the sliding motion of the plates is continuous. Once the accumulated strain exceeds the frictional force coupling the plates, the plates slip, thrusting the seaward edge of the continental plate upward while regions inland from the previously locked margin subside.

Geodetic and tide gauge data have shown that the coast of Washington and Oregon

[2]Hyndman's interpretation of this is that the deformation front occurs in unconsolidated accreted sediments in which slip is aseismic. The stick-slip region is further inland where the more consolidated materials of the oceanic and continental plates meet.

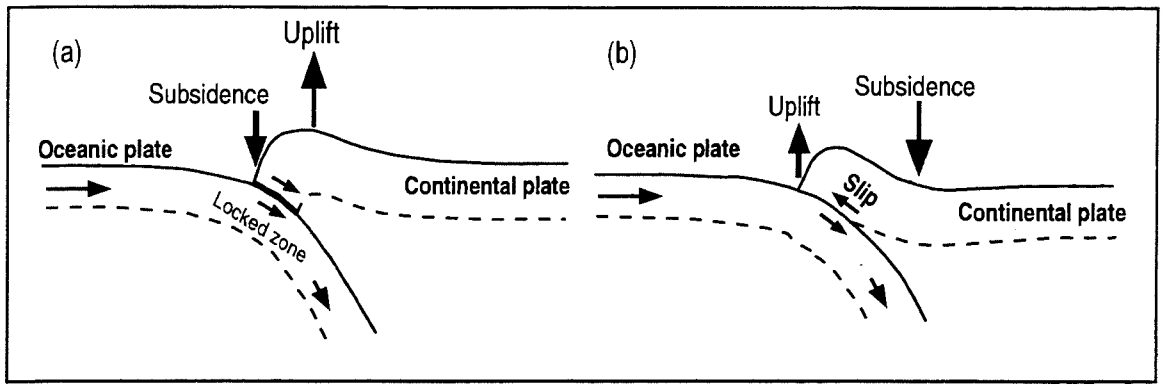

Figure 1.1: Schematic diagram showing the directions of uplift and subsidence during the period in which the oceanic and continental plates are locked and accumulate strain (a), and following seismic rupture (b) (after Hyndman and Wang, 1993).

is being uplifted at a rate varying from 0 to 5 mm a year (decreasing inland), consistent with the picture of interseismic strain accumulation described above (Mitchell *et al.*, 1994). The locked seismogenic zone has been estimated using thermal and geodetic data to be at least 40 to 100 km wide (Hyndman and Wang, 1995). Were the full width of the locked zone to rupture along its entire length (~1000 km) the rupture area would be of the order 10^5 km^2. According to the empirical equation of Wells and Coppersmith (1994) which relates earthquake magnitude to rupture area, this would give an earthquake magnitude of $M_w = 8.9$.

1.2.2 Review of evidence for past large earthquakes along the Cascadia subduction zone

The argument for the past occurrence of M_w 8 or larger earthquakes is based largely on the evidence found in marshes along the coasts of Washington, Oregon and Vancouver Island. Many of these marshes show clear signs of having undergone abrupt subsidence in the past[3]; in a few cases uplift has been reported, most notably at Cape Mendocino in California, Cape Blanco in Oregon (contested) and at Puget Sound in Washington.

[3]With the exception of northern Vancouver Island, Benson (1996).

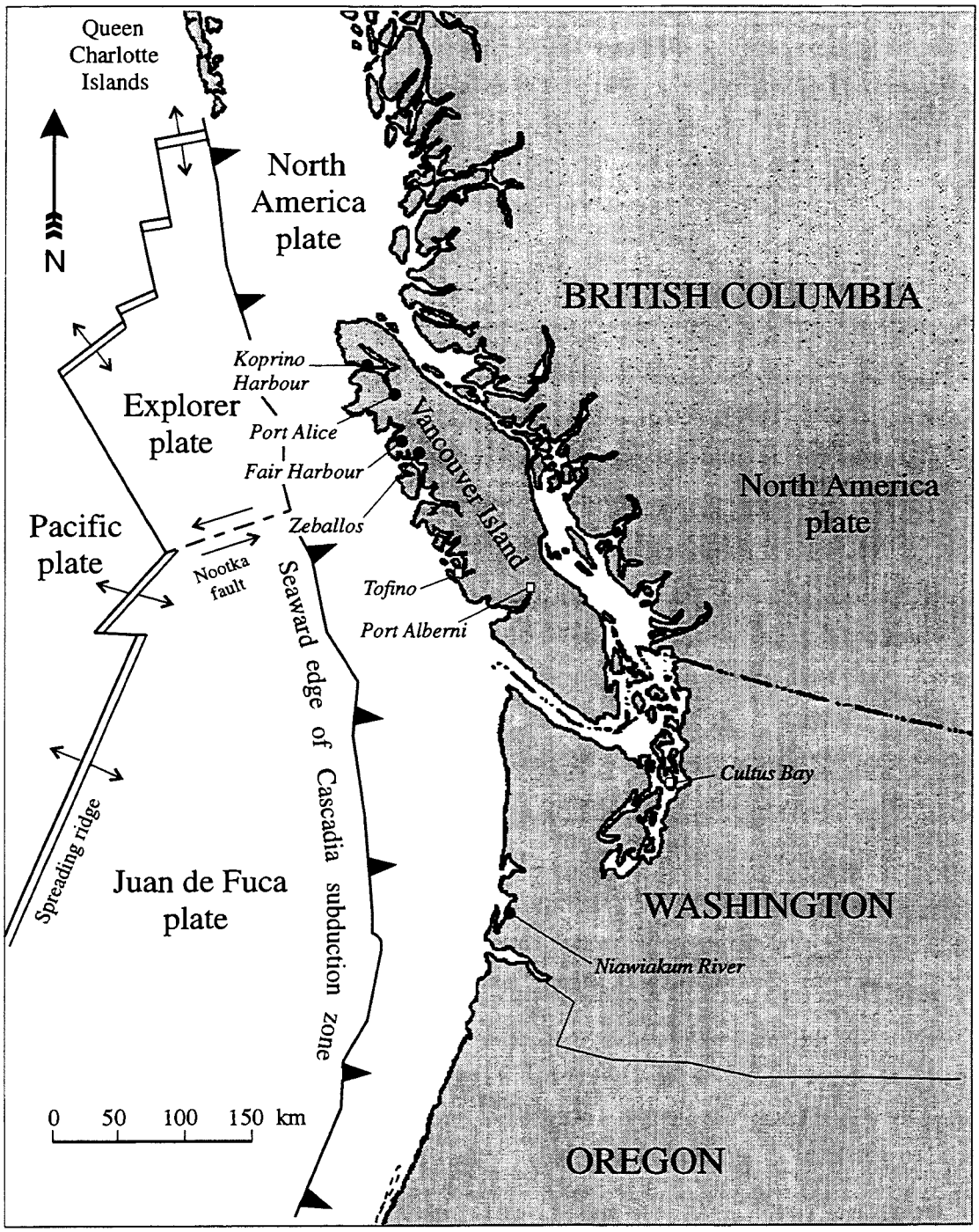

Figure 1.2: The Cascadia subduction zone showing plate names and some of the survey sites discussed in the text. Closed circles indicate sites that were sampled for optical dating by the author; open squares indicate sites dated by Huntley and Clague (1996).

In at least one of these locations (Puget Sound) uplift was due to failure along smaller faults in the North America plate, which may or may not have coincided with Cascadia boundary rupture (Bucknam *et al.*, 1992).

Seismic shaking

Strong shaking during an earthquake may cause water saturated sand or gravel to become fluid and to possibly flow to the surface as a "sand blow". Cross sections of two such sand blows were found, along with other smaller sandy intrusions, along the Copalis River, Washington (Atwater, 1992). Woody roots and sticks found lying on the peaty soil over which the sand erupted yielded radiocarbon ages in the range 900–1300 years. Sand blows have also been found in marshes along the lower Columbia River; these appear to be coeval with the subsidence of the marsh around 300 years ago (Atwater *et al.*, 1995).

Turbidites[4] found off the coast of Oregon and Washington may have been caused by seismically induced liquefaction and slumping of sediments from the top of the continental slope (Adams, 1990). Cores taken at the base of the continental slope show that 13 such events have occured since the Mount Mazama eruption 7660±100 years ago[5], at intervals of 590±170 years on average. The youngest of these turbidites was estimated to have been deposited 300±60 years ago.

Other evidence for seismic shaking includes landslides into lakes and trees drowned by these same landslides or by rock avalanches damming streams; see for example Jacoby *et al.* (1992), Atwater and Moore (1992), Bucknam *et al.* (1992), Schuster *et al.* (1992). These events were probably related to an earthquake along the Seattle fault 1000–1100 years ago which led to sudden subsidence north of the Seattle fault in Puget Sound (as was found at Cultus Bay by Atwater and Moore, 1992) and abrupt uplift in regions south of the fault.

[4]An underwater deposit from a turbid water current, *e.g.* as might occur during a slumping of offshore sediments or a landslide into a lake.

[5]Calendar age from ^{14}C ages.

Subsided marshes and tsunami sands

Evidence for earthquake-induced subsidence is found in tidal marshes and from northern California to central Vancouver Island. The subsidence may be deduced from the relative concentrations of various plant and microfossil remains found at different levels in the buried marsh stratigraphy. Tidal marsh vegetation is particularly sensitive to changes in water salinity; for example, subsidence may cause a low marsh environment to become a tidal mudflat and freshwater grass or shrub-land to become a tidal marsh. Changes in salinity also strongly affect the concentration of certain species of diatoms and foraminifera[6]. Fossil foraminifera concentrations in the buried marsh peat act as an accurate marker for past elevation change in the marsh relative to sea-level (Guilbault *et al.*, 1995, 1996, Mathewes and Clague, 1994).

The presence of sand layers at the interface of the high and low marsh sediments is often best explained by deposits left by a locally generated tsunami at the time of the earthquake induced subsidence. For example, at Koprino Harbour on Vancouver Island the absence of potential for a large flood and the fact that the marsh is well protected from Pacific storm surges favors the interpretation of a tsunami origin for the sands. The tsunami sand layers typically thin and fine inland (Clague and Bobrowsky, 1994) and are in some places graded, with the coarser grains overlain by the fines (*i.e.* as one would expect for grains settling out of suspension). Along the Niawiakum River at Willapa Bay, Washington, one such sand deposit (dated at around 300 years ago) consists of approximately five thin superposed layers of mud and sand. These layers have been interpreted as deposits left by five separate waves of the same tsunami (Atwater and Yamaguchi, 1991). At the same site, fossil grass tufts rooted in the paleo-marsh surface were found in the sand layer, apparently flattened by a strong inland-directed flow as one might expect from a tsunami.

[6] *Foraminifera* (kingdom *protista*) are a phylum of microscopic marine organisms with hard, pore studded shells (called tests) usually composed of cemented granules of calcium carbonate. The tests are often multichambered, the typical appearance being that of a clump of spheres, but may also be single chambered. Foraminifera (also known as "forams") live predominantly in sand or attached to stones, algae or other organisms, however there are also two families of free-swimming forams. Diatoms (phylum *diatoma*, kingdom *protista*) are microscopic organisms with halved tests (shells) composed of cemented silica. Fresh-water and marine diatoms are both common.

It should be emphasized that there are several other explanations for sand layers in tidal marshes; it is possible for instance that the sand was deposited during a flood or a storm surge. Even when the possibility of a storm or flood deposit is ruled out, as would be the case in a sheltered inlet with little fluvial input, the possibility remains that the sand layer was deposited by a *distantly* generated tsunami.

It is well known that tsunamis can have severe effects even at great distances from their source. This was exemplified at the head of Alberni Inlet on Vancouver Island after the great Alaska earthquake of 1964. A large tsunami generated by this earthquake severely damaged the town of Port Alberni and left a thin sand sheet in the nearby marsh (Clague *et al.*, 1994). Measurement of cesium-137 concentrations in the strata surrounding this sand layer are consistent with the interpretation that this sand was deposited during the 1964 Alaska tsunami[7] (Clague *et al.*, 1994).

1.2.3 Summary of the chronology for past subsidence events along the Cascadia margin

There is only one past seismic event, approximately 300 years ago, for which extensive evidence is found along the entire length of the Cascadia subduction zone. However, evidence for earthquake induced subsidence with recurrence intervals ranging from a few hundred to a thousand years have been found for the last 5000 years. At Johns River in Washington, Shennan *et al.* (1996) report eight abrupt subsidence events over the last 5000 years. Mathewes and Clague (1994) have reported two subsidence events $\sim$ 3400 and $\sim$2000 ^{14}C years ago in southern British Columbia.

The most recent compilation of radiocarbon ages for the 300-year-old event is provided in the paper by Nelson *et al.* (1995). The ages presented in this paper were obtained from coastal sites in Washington (Copalis R., Niawiakum R., Naselle R.), Oregon (Nehalem R., Netarts Bay, Salmon R., Coquille R.), California (Mad River Slough) and Vancouver Island (Port Alberni). Dated samples consisted either of plant fossils found at the top of the buried marsh surface or stumps rooted in the buried

[7] ^{137}Cs provides a convenient (though grim) marker for post-1960's depositional events. Atmospheric concentrations of ^{137}Cs peaked in the late 1950's and early 1960's when atmospheric testing of nuclear weapons was at its height.

soil (presumably killed upon subsidence of the forest floor). The large variation in the ^{14}C calibration curve (which permits correction for variations in atmospheric ^{14}C content with time) for ^{14}C ages less than 1000 years means that most of the calibrated ^{14}C ages could only be narrowed down to a few hundred years. At best, the outer tree ring and herb ages indicate that subsidence occurred no earlier than A.D. 1660. However by correlating calibrated ^{14}C ages ranges of different tree rings within the same stump, the time of tree death for a stump collected at Mad River Slough was narrowed down to A.D. 1700–1720.

Lack of written accounts of earthquakes at the Cascadia margin precludes subsidence events after European settlement of the region around 1800. If we assume that the subsidence at each site was from a single earthquake then the most likely time for this event given the radiocarbon evidence would be A.D. 1700–1720, as concluded by Nelson *et al.* (1995). If the rupture occurred during a series of smaller earthquakes rather than a single large event, these must have occured within a time range of at most 150 to 350 years ago (taking all the data into account). However, such temporally extended sequential rupturing is not supported by the ages found for tree stumps separated by nearly 700 km in Washington, the Nehalem River, Oregon and in northern California, (Nelson *et al*, 1995). This lends support to the possibility that rupture along over 1000 km of the subduction zone occurred during a single large earthquake 300 years ago.

Historical accounts

Although there are no written European accounts of large earthquakes in Cascadia there exists a widespread oral tradition among the aboriginal peoples of the Northwest coast which suggests the past occurrence of such an event (Heaton and Snavely, 1985; Sproat, 1987, pp. 124–125; Clague, 1995). Many of these accounts refer to a flood accompanied by shaking which came from the sea in the middle of the night. Japanese records indicate the passage of a large tsunami on the night of January 27–28, A.D. 1700 (gregorian calendar); which is within the geologically predicted window for the last large earthquake in Cascadia. By analyzing the descriptions of tsunami

damage along the Japanese coast, Satake *et al.* (1996) inferred that the tsunami was probably of far-away origin. Assuming that this tsunami was generated by a Cascadia quake and given that the travel time of a tsunami wave from Cascadia to Japan is about 10 hours, Satake *et al.* determined the time of the quake to be 9:00 pm (Pacific Standard Time) on January 26, 1700. This is consistent with American aboriginal accounts that the tsunami hit in the middle of a winter night.

1.2.4 Motivation for present work

Problems with ^{14}C dating of young samples

There are several problems associated with ^{14}C dating of young marsh fossils to determine the time of an earthquake; these were addressed in a paper by Nelson (1992). Errors may arise for example if a herb sampled for dating did not die within a few years of marsh subsidence; in such a case an erroneously young age for the earthquake would be obtained. The use of sticks and branches buried at the level one wishes to date poses problems because they are of unknown provenance, and indeed may have died long before burial. The inclusion of modern organics in the dated sample is particularly insidious, especially for shallow buried samples. Roots from living vegetation may penetrate to depths of 1 m in the marsh, contaminating plant fossils used for dating. Problems of the type mentioned above are referred to as association uncertainties, their magnitude is often difficult if not impossible to determine.

Other uncertainties arise in the analytical process of determining the age (*i.e.* measuring ^{14}C to ^{12}C ratios). These uncertainties are typically of the order 50 years for materials 300 years old or younger (see for example Nelson, 1992)[8]. Finally, uncertainties usually expand upon conversion of the ^{14}C age to calendric age using the ^{14}C age calibration curve. For young samples this is the greatest source of uncertainty. As mentioned earlier the large deviations in the calibration curve below 1000 years means that several age ranges may be obtained for a single ^{14}C age.

In the case of ^{14}C dating of tree rings one may narrow down the age range by

[8]Uncertainties of 10 to 20 years have been quoted by Atwater *et al.*, (1995). This is the result of the exceptionally precise technique of M. Stuiver which is by no means typical of usual ^{14}C dating.

obtaining ^{14}C ages for two or more portions of the tree and requiring that these ages match expectations from the known age difference of the portions sampled. This technique, known as "wiggle" matching, has been used by Nelson *et al.* (1995) to accurately date a tree believed to have been killed consequent to the 300-year-old Cascadia earthquake. A narrow range of A.D. 1700–1720 was obtained for the time at which the tree died using this method; in contrast the calibrated ^{14}C age for the youngest tree ring ranged from A.D. 1720 to A.D. 1950.

Direct dating of the tsunami sands using optical dating

Optical dating provides an alternative method for dating subsidence events at marsh sites where tsunami sediment was deposited at the time of subsidence. All that is required is that the source sediment be sufficiently exposed to sunlight prior to the time of deposition and that it be buried quickly after deposition, that is, over a time scale much smaller than the total deposition time. If the tsunami sediment originated from shallow mud flats and tidal channels, then the first requirement, that of sufficient sunlight exposure, may possibly be satisfied. The channel and tidal flat sediments receive light exposure because they are constantly being reworked by mud-dwelling animals, tidal currents and waves. The second requirement may be easily met; after deposition the tsunami sediment is covered by mud in the space of a couple of years or less (*i.e.* over a time scale much shorter than the time of burial, which in this case is of the order of a few hundred years) and thereby shielded from sunlight. Reworking of the tsunami deposits, by bioturbation or waves for example, is not likely to have a large effect on the optical age since these processes probably only occur during the first few years after deposition. Faillure of this last assumption would lead to erroneously young optical ages.

There are primarily two reasons why this project was worth undertaking. Although it is impossible to conclusively demonstrate the simultaneity of subsidence events recorded along the Cascadia margin by any single dating method, it was hoped that optical ages of the tsunami sands could narrow the time range over which these events occured. Agreement of the optical ages and the radiocarbon estimates would

lend support to the optical dating procedure, especially as concerns the dating of geologically young sediments. Very few optical ages have been produced for sediments as young as those studied here. This is in part due to the relatively low photo-stimulated luminescence intensity of such samples but is also related to the sparsity of young geological samples of known age against which the optical dating method may be tested.

1.2.5 Pilot study of the optical dating of tsunami deposits

Three tsunami deposits were chosen for optical dating by Huntley and Clague (1996). One deposit was from Cultus Bay in Puget Sound, Washington; it was laid down by a tsunami generated by an earthquake on a fault in the North America plate between 1000 and 1100 years ago. Its age was well known from high-precision radiocarbon ages at this site and other sites along Puget Sound (Atwater and Moore, 1992). For this reason, the sample from this site served as a good test of the optical dating technique. The two other deposits dated were from southern Vancouver Island at Tofino and Port Alberni. These date to between 150 and 400 years ago, probably by a tsunami generated during a plate-boundary rupture at the Cascadia subduction zone 300 years ago. In addition, sand and mud collected from the tidal flats and tidal channels at Cultus Bay and Tofino were measured to determine the level of solar resetting of these hypothetical "modern analogues" of the source sands for the tsunami deposits.

In all three cases the optical ages were consistent with the ^{14}C age estimates. At Cultus Bay the optical age obtained was 1285±95 years. The ages obtained for the two Tofino samples were 325±25 years and 260±20 years, whereas the sand layer at Port Alberni yielded an age of 355±45 years. The equivalent doses[9] obtained for modern source sands at the Tofino and Cultus Bay sites indicate a level of solar bleaching in the source material barely sufficient to produce a correct age. The equivalent doses of the source sands ranged between 0% and 10% (increasing with depth below the surface) of the equivalent dose obtained for the buried sand layers. The ages for the Tofino and Cultus Bay sands quoted above have been corrected for the non-zero

[9]This term is defined in the following section.

equivalent doses of the modern source sand analogues.

1.3 Optical dating

1.3.1 Determination of the equivalent dose

Optical dating is a technique that dates the last exposure of a mineral, typically quartz or feldspar, to light. The process relies on the presence of electron traps in the mineral which are readily emptied by daylight yet are thermally stable on a geological time scale. The primary assumption is that the mineral has been exposed to light just prior to, during or shortly after deposition in the environment. The exposure must be sufficient that all of the electron traps (or at least the fraction that is later sampled in the laboratory) have been emptied. Once the mineral is deposited it must be shielded from sunlight within a time much shorter than the time since deposition. The electron traps fill up gradually with time due to a radiation dose from naturally occurring sources of ionizing radiation, from radio-isotope decay in the surrounding sediment and within the mineral grains themselves and from cosmic rays. Energetic alpha, beta and gamma particles traversing the crystal impart large energies to electrons, ejecting them from the stable valence band. The energetic electrons suffer a series of collisions through which they lose energy, partly as heat (through the excitation of lattice vibrations) but also by evicting other electrons from the valence band. Eventually all of the excited electrons become thermalized and they may then be captured by traps. This process is shown schematically in the band structure diagram of Figure 1.3.

The trapped electrons may be sampled by heating (as one does in thermoluminescence dating) or by irradiation of the mineral with light of the appropriate photon energy (optical dating). In either case, the excitation ejects electrons from their traps and this will be followed by the emission of light if the electrons recombine at luminescence centres. The luminescence centres are typically metallic impurities in the ionic crystal such as Ag^{2+} or Mn^{2+} ions. When an ejected electron recombines at one of these impurities, the prompt de-excitation of this state produces emission of

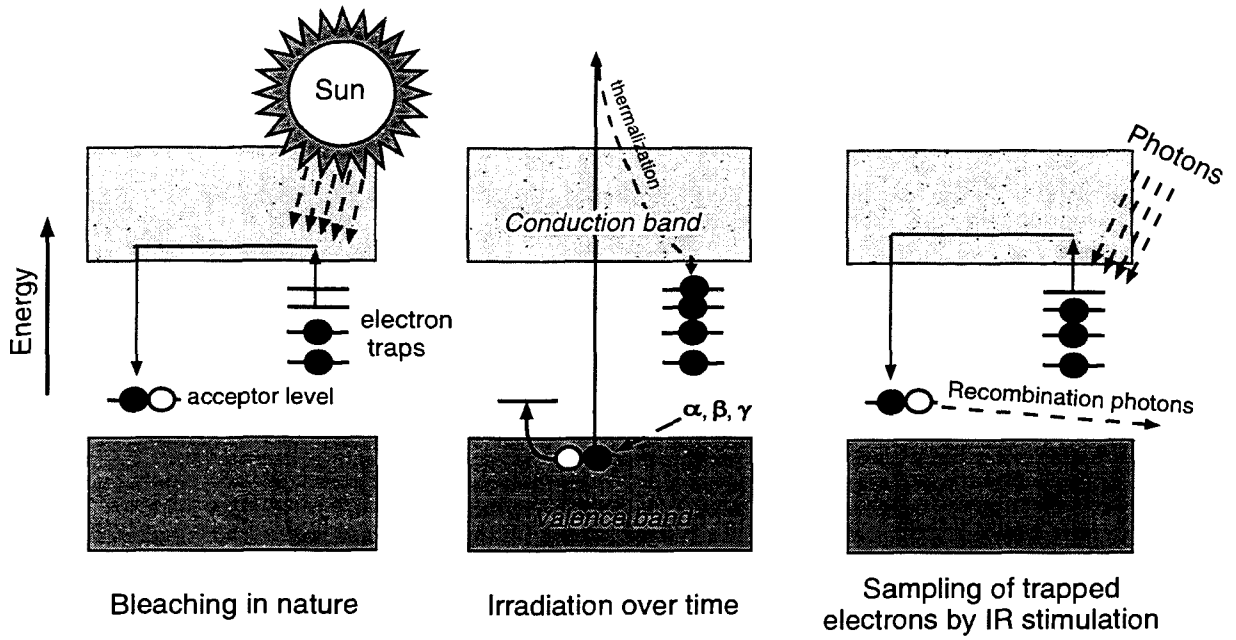

Figure 1.3: Schematic band structure and defect centres in a mineral. *Left*: Electrons are ejected from the traps during sunlight exposure. *Centre*: Over time α, β, γ and cosmic radiation leads to filling of some of the electron traps. *Right*: Trapped electrons are sampled in the laboratory by counting the number of recombination photons emitted by the mineral under optical stimulation. The recombination luminescence intensity is a measure of the past radiation dose.

a photon. Consequently, the energies of the emitted photons are not related to the depth of the trapped state but depend only on the properties of the luminescence centre. One should note that, unlike ordinary photoluminescence, the energies of the recombination photons may be greater than those of the incident photons. This is of great practical significance since it allows the luminescence photons to be easily isolated from scattered excitation photons and photons resulting from ordinary photoluminescence.

The total number of recombination photons obtained upon optical eviction of electrons from their traps is proportional, but not equal, to the number of trapped electrons in the mineral sample. This is due to the possibility of electrons wandering into shallower traps (where they may remain or suffer re-eviction) or recombine non-radiatively at so-called "killer" centres, the excess energy in this case being released as heat. The transfer of electrons from deep traps to shallow ones during irradiation manifests itself as the residual luminescence which is often observed to persist after removal of the stimulation source. This phosphorescence arises from the thermal release of electrons from shallow traps at room temperature.

The laboratory equivalent to the radiation dose received in nature, called the *paleodose equivalent*, is usually determined by one of two techniques; (1) an additive dose method, (Figure 1.4) or (2) a regeneration method, (Figure 1.7). The natural radiation dose rate is determined from measurements of concentrations of radioactive isotopes and calculation of the cosmic ray dose rate in the environment. The time since the electron traps were emptied in nature and subsequent (hopefully prompt) burial of the mineral grains is simply obtained by dividing the paleodose equivalent by the environmental dose rate. Here we have assumed that the environmental dose rate is constant over time, however if the dose rate changed over the period of burial, then this must also be taken into account when calculating the age. We will use the more common term *equivalent dose* interchangeably with the term "paleodose equivalent" in what follows.

The additive dose method

In this method various doses of ionizing radiation are given to different groups of aliquots[10] of grains prepared from a sample. This has the effect of increasing the population of traps and hence the level of stimulated luminescence observed relative to that of the natural sample. For small radiation doses the increase in luminescence is linear, however as the dose increases the luminescence approaches a plateau due to the finite number of traps in the sample. The laboratory dose which produces

[10]The term aliquot is used to refer to a weighed amount of sample grains.

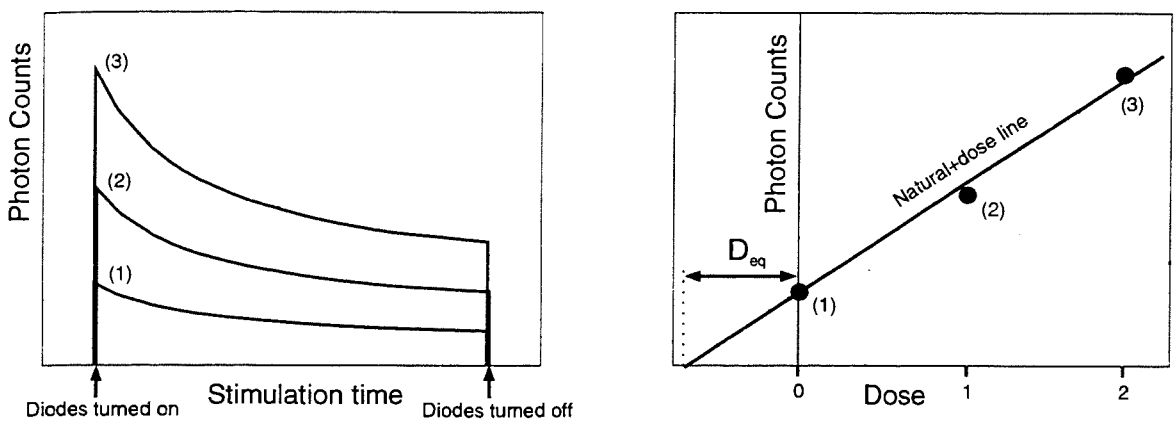

Figure 1.4: Illustration of the additive dose method for extrapolating the equivalent dose received by a mineral sample in nature (no thermal transfer correction applied). The left diagram shows the idealized decay curve for 3 aliquots; (1) is a natural undosed aliquot, (2) has been give 1 unit of laboratory dose and (3) has been given 2 units of laboratory dose. By plotting the integrated luminesence intensity versus dose (right diagram) the equivalent dose D_{eq} may be determined from the extrapolated natural+dose line.

the same level of luminescence as the environmental dose, the *equivalent dose* or D_{eq}, may be obtained by extrapolating the line of stimulated luminescence intensity versus applied dose to zero intensity, as shown in Figure 1.4 (this is not quite correct as will be discussed shortly).

In practice one would produce such a plot by taking several groups of aliquots of the mineral sample, exposing each group to a known laboratory radiation dose and then measuring the photo-stimulated luminescence. The luminescence may be measured for example by irradiating the aliquot with monochromatic light of a particular photon energy and counting the emitted recombination photons with a photo-multiplier tube. The measured luminescence intensity decays with time as the electron traps are emptied.

There are several complications to the optical dating process which need to be addressed at this point in the discussion. The first is that of thermal fading; this arises from the thermal depopulation of shallow traps which are filled during the short but

intense laboratory irradiation. In nature these shallow traps are not appreciably populated since the radiation intensity is so low that the unstable traps empty as fast as they are filled. If one were to compare the optically stimulated luminescence intensity of the mineral sample obtained directly after irradiation and say a few days after irradiation one would find that the luminescence signal decreased over this time period. The simplest manner to remove the unstable thermal component of the luminescence produced by irradiation is to subject the sample to a mild heating, usually 100°C to 200°C for several hours; this process is referred to as *preheating*. This effectively depopulates the shallow, thermally unstable traps but also produces an interesting secondary effect. It is often found that when one preheats a natural zero-age mineral sample that has not been subjected to a laboratory dose, the level of photostimulated luminescence in the preheated sample exceeds that of the unpreheated mineral. This effect is most easily explained by the transfer of charge from traps which do not readily respond to optical excitation yet are easily emptied during heating, to traps which are easily sampled by the optical excitation. This interpretation suggests that there exists two broad categories of traps; "optical traps" which are readily emptied by optical excitation but are thermally stable and "thermal traps" which are emptied by heating but do not yield so readily to optical stimulation[11].

A correction for this thermal transfer of charge which occurs during preheating must be applied in order to obtain the correct D_{eq}; it is achieved in the following manner. The photostimulated luminescence signal of a sample which has received significant insolation (or has been *bleached* in common parlance) should be close to zero, or more precisely close to the background photon count rate of the detection system. After preheating of this well-bleached sample, its measured luminescence signal is non-zero due to the thermal transfer of charge into light sensitive traps. The photo-stimulated intensity is a measure of the amount of thermal transfer which has occured during the preheat, it depends on the number of electrons in the traps which are responsible for the thermal transfer. Since the traps that are the source of the thermally transferred electrons are not susceptible to eviction by light exposure,

[11]These categories of traps have been referred to as "principal" and "secondary", respectively, by Huntley and Berger (1995).

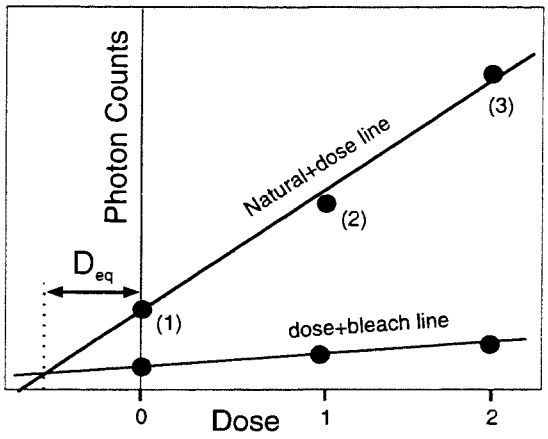

Figure 1.5: Additive dose method to which the thermal transfer correction has been applied. The lower line is the line of dose+bleached aliquot intensities. The equivalent dose D_{eq} is determined by extrapolating the intersection of the dose+bleach line with the upper dosed aliquot line.

then a substantial fraction of these may be occupied at the time of deposition. After deposition this "thermally transferable" fraction of electrons increases due to the radiation dose. The thermal transfer component of the luminescence measured at the present day therefore contains a component acquired over time as well as a component which was present in the sample at deposition. One may isolate the thermal transfer signal by bleaching and then preheating the sample. The thermal transfer component which was present at deposition may be determined by subjecting different portions of sample to different doses, bleaching and preheating the lot and then extrapolating the measured luminescence growth curve back to the paleodose equivalent. This is the basis of the thermal transfer correction introduced by Huntley *et al.* (1993a); it is shown schematically in Figure 1.5.

There is some question as to the type of laboratory bleach one should use in order to determine the thermal transfer correction. The laboratory bleach should be designed to empty only those traps that were emptied by environmental sunlight exposure and that are sampled by the particular excitation wavelength used in the laboratory. The use of a sunlight bleach would be reasonable, for example, in aeolian

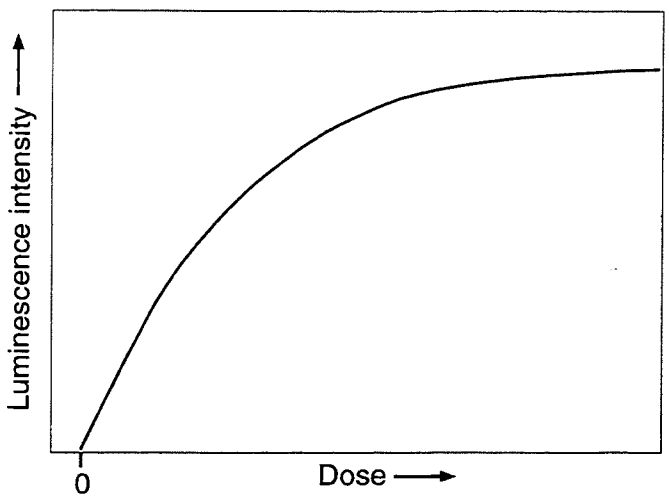

Figure 1.6: At high doses the luminescence saturates due to filling of available electron traps. In this case the data are best fit to a saturating exponential.

samples, however there are instances when a sunlight bleach would be inappropriate. In underwater sediments, for instance, the red and blue-violet ends of the sunlight spectrum are filtered out. A sunlight bleach of such sediments in the laboratory could result in the emptying of traps other than those emptied in nature. This could lead to an optical transfer of charge from deep traps that were not emptied during the natural period of insolation to shallower traps during laboratory bleach. This effect was observed in a modern sand collected from a tidal flat at Tofino by Huntley and Clague (1996). It was found in this case that the luminescence intensity of the young sunlight-bleached sand exceeded that of the unexposed sample; usually bleaching would reduce the level of photo-stimulated luminescence intensity in a natural sample. The subsequent use of a long-wavelength (red–infrared) bleach rather than the sunlight bleach brought the bleached aliquot intensity down to a level below that of the unbleached sand. Bailiff and Poolton (1991) reported a similar optical transfer in feldspars bleached at wavelengths shorter than 450 nm.

Nonlinearity of the luminescence sensitivity

Since the number of stable traps that may be occupied is finite, for very high radiation doses (*i.e.* as one would have in old samples) the fraction of populated traps approaches 1 and the luminescence saturates. In this case the luminescence data is best fit to a saturating exponential,

$$I(D) = I_{sat}[1 - e^{-D/D_o}] \tag{1.1}$$

In the above, D is the dose, I_{sat} is the saturation intensity and the parameter D_o determines the onset of saturation. A linear fit to data for which there is significant curvature in the dose response would lead to an overestimate of the D_{eq}.

The regeneration method

In this method aliquots of the sample are bleached and subsequently given various radiation doses in addition to the aliquots which have only been treated with a laboratory radiation dose (the latter being referred to as the Natural+dosed aliquots). The equivalent dose is obtained from the resulting luminescence growth curve by finding the dose at which the luminescence intensity equals that of the natural sample as shown in Figure 1.7.

Normalization of the aliquot luminescence intensities

It is found that for aliquots containing even several thousand grains the luminescence sensitivity to a radiation dose varies considerably from aliquot to aliquot, even if each contains an equivalent amount of material. This is due to the fact that the bulk of the luminescence is produced by a small fraction of the grains in each aliquot. In order to reduce the scatter this causes the luminescence in each aliquot is usually normalized. Normalization values are obtained by measuring the luminescence of each aliquot for a short exposure to optical stimulation and dividing this luminescence intensity by the average intensity for all of the aliquots used in the particular experiment. The optical excitation flux and exposure time are chosen in such a way that the "short shine" measurement produces a decay of at most only a few percent in the natural

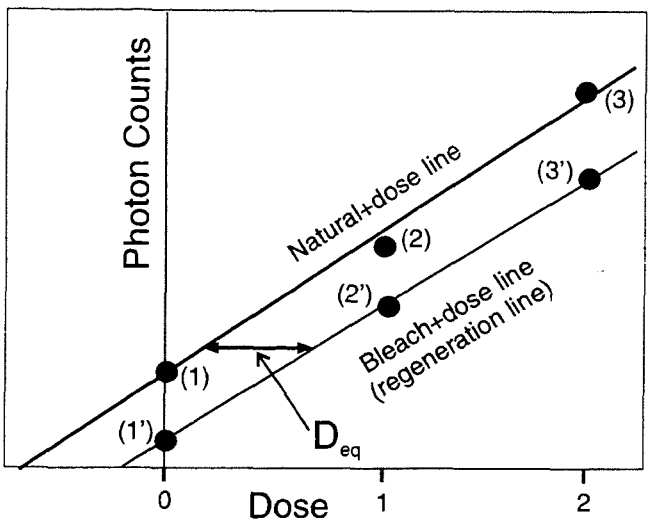

Figure 1.7: The regeneration methods for determining the paleodose. Labels (1), (2) and (3) refer to the aliquots described in Figure 1.4. Aliquots labeled (1′), (2′) and (3′) were bleached and then received the same doses as (1), (2) and (3).

luminescence intensity. One may later correct for the reduction this produces in the measured equivalent dose.

In the short shine normalization method the luminescence is measured before the sample has been subjected to any treatment. The aliquot intensities may also be normalized after the main luminescence measurements have been made as follows. One subjects all aliquots to a bleach, a radiation dose and a preheat treatment; finally the luminescence from each aliquot is measured. After the bleach, no luminescence should be measured from each aliquot, hence the luminescence intensity measured after the dose and heating should accurately reflect the luminescence-producing sensitivity of each planchet. This "post-measurement normalization" method has the advantage that no correction is needed for the initial decay of the aliquot intensities. A post-measurement normalization may be more suitable for samples that consist of a mixture of well-bleached and unbleached grains, as will be discussed in Section 5.2.1. It has the disadvantage that different aliquots have had different histories, and these differences could cause changes to the sensitivity.

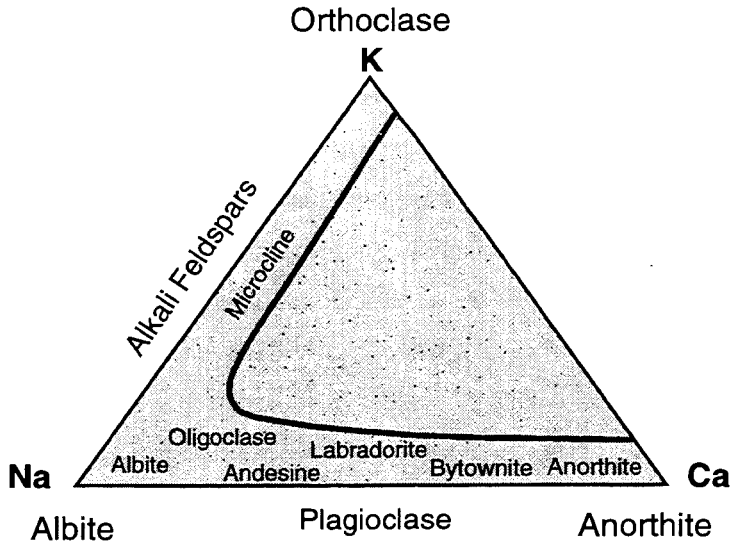

Figure 1.8: The compositional range of feldspars represented in a ternary diagram, after Deer *et al.* (1973).

1.3.2 Luminescence properties of quartz and feldspars

The actual structural or impurity defects responsible for the luminescence in quartz and potassium feldspars have not yet been elucidated, in fact the electron trapping and eviction mechanism itself remains poorly understood. This is largely due to the difficulty of associating physically measurable effects to the responsible defects in the mineral. Another complicating factor is that one finds an enormous variation in the luminescence properties of mineral samples of different geological provenance, even if they are of similar nominal composition. In particular, if we may speak of a luminescence generating efficiency or "brightness" (*i.e.* in the sense of the luminescence count-rate produced per unit applied radiation dose) then one finds a considerable range of brightnesses even for feldspars of identical nominal composition.

Feldspars are aluminosilicate minerals which are classified in terms of the mole percentages of three end members; orthoclase ($KAlSi_3O_8$), albite ($NaAlSi_3O_8$) and anorthite ($CaAl_2Si_2O_8$) as shown in Figure 1.8. Feldspars of composition intermediate between orthoclase and albite are termed alkali, whereas members lying along the

calcium-sodium axis are referred to as plagioclase. A number of studies have been made on the thermoluminescence emission spectra of feldspars of different compositions; I cite in particular the paper by Prescott and Fox (1993) in which spectra in the range 1.5 eV to 5.0 eV (830 nm to 250 nm) for 27 samples of differing composition are compared . It was found that the end members of the feldspar ternary diagram exhibit strong thermoluminescence emission in the following wavelength regions; a strong peak at ~3.1 eV (400 nm) for high orthoclase members, a peak at ~4.5 eV (275 nm) with weaker emission at 2.2 eV (570 nm) for high sodium (albite) feldspars and 1.5–2.0 eV (600–800 nm) emission in calcium-rich feldpars. The high calcium plagioclase feldspars (over 50% anorthite) are noted for their low thermoluminescence-producing efficiency relative to other plagioclase and alkali feldspars. Feldspars of intermediate composition were found to exhibit emission features intermediate between those of the end members, suggesting a mixture of feldspathic phases within the samples. Alkali feldspars with high albite content, on the other hand, produced an infrared peak similar to the emission observed in mid-range plagioclases.

These results are of immediate relevance to optical dating since they show that it is possible to isolate the emission of a specific feldspar from that of other feldspars in the sample. For the purposes of dating, K-feldspar is the most convenient on account of its bright blue emission near 3.1 eV as well as its strong luminescence response when subjected to infrared radiation around 1.4 eV (880 nm).

This response in K-feldspar was reported by Hütt *et al.* (1988) in a study of K-feldspar excitation spectra and was interpreted as evidence for the existence of a trap (or class of traps) distinct from other traps sampled in the mineral. In a study of optical excitation in the 1.6 eV to 2.8 eV range, Ditlefsen and Huntley (1994) suggested the existence of at least two more traps in K-feldspar, one near an excitation photon energy of 2.1 eV and a second at 2.3 eV or deeper. This is in strong contrast to what was found in quartz where one could easily explain the observed optically stimulated luminescence behaviour by the existence of a single trap.

Bailiff and Poolton (1991) measured the infra-red stimulated luminescence of feldspar samples which had been given a β dose, followed by a near-monochromatic bleach, for bleaching wavelengths in the range 1.0–2.5 eV (500–1200 nm). These

"bleaching spectra" differ from Hütt *et al.*'s excitation spectra in that Bailiff's experiment essentially measured the response of the *infra-red sensitive* traps to photons of different wavelengths whereas Hütt's excitation spectra contained luminescence components from *every* level of trap emptied by a photon of particular energy. Nevertheless, Bailiff and Poolton's bleaching spectra show the same features found in Hütt *et al.*'s excitation spectra; an excitation peak at 1.4–1.5 eV (850–900 nm) and a rise in the luminescence at shorter wavelengths. Bailiff and Poolton did not observe the decrease in luminescence at photon energies above 2.1 eV (600 nm) reported by Hütt *et al* (1988); instead the luminescence was found to continue to rise rapidly at photon energies above 2.1 eV as was also found in Ditlefsen and Huntley's (1994) study.

Bailiff and Poolton (1991) also produced excitation spectra in the range 2.7–5.0 eV (250–450 nm) for feldspar samples that had been previously bleached under 1.3 eV (950 nm) light for sufficient time to reduce the infra-red stimulated luminescence to a negligible level. For excitation energies above 3.1 eV (400 nm) luminescence was observed; this was attributed to the transfer of charge from deep traps that are not emptied by the 1.3 eV bleach.

Spooner (1993) produced bleaching spectra similar to Bailiff and Poolton's for five feldspars of different compositions. In particular, he plotted the bleaching energy required to reduce the luminescence caused by 1.4 eV excitation to a particular fraction of the initial level versus the bleaching wavelength. Spooner found that for photon energies above 1.6 eV the bleaching response was approximately exponential; below this energy a "resonance" was observed around 1.4–1.45 eV, as had been seen in Bailiff and Poolton's earlier work. The photon energy at the resonance, as well as the general form of the bleaching spectrum, did not appear to depend strongly on the feldspar composition of the five measured feldspar samples.

Spooner explained the form of the bleaching spectra in terms of the model proposed by Hütt *et al.* (1988) in which 1.4 eV excitation raises the trapped electron to an intermediate excited state before excitation to the conduction band, whereas for incident photon energies above $\sim$1.6 eV direct optical excitation or "photoionization", of the trapped electron to the conduction band is the dominant electron detrapping mechanism. It should be emphasized that the details of this process or even the

validity of this model have not yet been shown.

Thermal stability

The fact that 1.4 eV photons could excite electrons out of thermally stable traps was not expected on the basis of Mott and Gurney's (1948) simple model. According to this model the ratio of the energy required for direct photoionization to the conduction band to that necessary for thermal eviction from the trap is approximately equal to the ratio of the static and optical dielectric constants. The static dielectric constant for feldspars varies according to composition; in microcline it is about 5.6 (at 50 Hz) whereas in orthoclase it is somewhat lower, 4.5 (at 100 Hz) (Parkhomenko, 1967). The optical dielectric constant is easily obtained from the square of the refractive index which is roughly $(1.52)^2$=2.31 in most alkali feldspars (Deer *et al.*, 1973). The ratio of the static to optical dielectric constants in potassium feldspar is thus approximately 2.2 (taking the average of the static dielectric constant in microcline and orthoclase). The activation energy for direct photoionization to the conduction band is roughly 1.6 eV to 1.7 eV, as determined from the onset of the absorption regime in Spooner's (1993) bleaching spectra, from which can be deduced a thermal activation energy of 0.75 eV (*i.e.* this is the energy required for thermal excitation out of the impurity state to the conduction band). The thermal lifetime of a trap is given by (Aitken, 1985),

$$\tau = s^{-1} e^{+E_t/kT} \tag{1.2}$$

where E_t is the thermal activation energy and s is the frequency factor which is material dependent. In feldspar the frequency factor for the stable thermal traps (*i.e.* the traps that are not readily emptied by heating up to 100°C or more) is of the order 10^{13} s^{-1} (Aitken, 1985)[12] Given a thermal activation energy of 0.75 eV, the thermal lifetime for the traps sampled during 1.6 eV excitation at room temperature would be of the order 1 s. Therefore, from these simple arguments alone one would not expect to detect any luminescence signal in natural samples under 1.6 eV excitation. This indicates that the situation prevailing in the crystal is more complicated than depicted

[12]Note that this is of the order of the lattice vibration frequency, *i.e.* 10^{13} s^{-1}.

above. In the above calculation, I assumed that the traps are emptied by direct photoionization to the conduction band, whereas evidence suggests that detrapping occurs by transition to one or more excited states of the trap before the conduction band is reached, as proposed by Hütt *et al.* (1988). However, this model similarly fails to explain the observed thermal stability of the trapped states. The optical activation energy in this case would be less than 1.6 eV (Hütt suggested 1.4 eV), however the thermal excitation energy for direct transition to the conduction band would remain of the order 0.75 eV, using the previous argument. Another possibility is that the transition from the trapped state to the conduction band occurs by multiple optical transitions as suggested by Godfrey-Smith *et al.* (1988).

The thermal stability of the traps sampled by 1.4 eV radiation may be estimated at least empirically by comparing optical ages for old samples with ages obtained by other methods. Optical ages for samples near or older than the average trap lifetime should be consistently lower than the "true" age. Lian *et al.* (1995) reported optical ages that are consistent with radiocarbon and other age estimates for organic-rich samples up to 100 ka old. One sample that had been dated to $\sim$1 Ma by the fission track method gave an optical age of 660$\pm$120 ka, which may indicate instability of the sampled traps over this period. Duller (1994) obtained similar results from coarse-grained K-feldspar samples from New Zealand. Only two of the twelve samples yielded optical ages that were thought to be genuine underestimates of the geological estimates; optical ages of 235$\pm$16 and 300$\pm$30 years were obtained for samples believed to be older than 350$\pm$40 ka. Duller concluded that reliable optical ages could be obtained for samples up to 130 ka using 1.4 eV excitation in K-feldspars. Ages obtained from a loess profile at Dolní Vestonice in the Czech Republic by Musson and Wintle (1994) are lower than ages expected from correlation of the soil stratigraphy with deep-sea oxygen isotope records. The authors suggested that this might be due to the decay of luminescence centres over a period of 150 ka. Thermal fading for samples less than 1000 years old is therefore not expected to be significant.

The problem of anomalous fading

When a sample is irradiated in the laboratory it may receive the same dose in 20 minutes as it did over several thousand years of burial. This poses serious problems in the dating process since the distribution of filled traps, that is the fraction of filled traps at a particular depth below the conduction band, will undoubtedly be different for the natural and laboratory irradiated samples. In particular, artificial radiation leaves charge in shallow traps that would normally be empty in nature due to thermal instability. For this reason it is necessary to either wait a sufficiently long time for the shallow traps to empty or to evict the electrons from these traps by preheating, usually at a temperature between 100°C and 150°C (waiting is preferable but is not always practical). This is the thermal fading discussed earlier in the context of the thermal transfer correction. There is, however, a fading component to the luminescence signal that cannot be erased by heating which shows up weeks to months after sample irradiation; this effect is termed anomalous fading.

A comprehensive study of anomalous fading in feldspars was undertaken by Spooner (1992, 1994); he demonstrated the presence of anomalous fading in feldspars of a wide range of compositions. For this reason experiments that monitor the magnitude of this fading are required in the optical dating of feldspar samples. The anomalous fading process is athermal in the sense that the temperature dependence of the process does not show up through the usual $e^{-\Delta E/kT}$ term.

1.3.3 Review of optical dating in geological contexts

Here I review studies of the applicability of the optical dating technique using 1.4 eV excitation in K-feldspar to dating geological samples. A recent review of optical dating has been published by Aitken (1994). The concept of using the optically stimulated luminescence from minerals for dating was first introduced by Huntley *et al.* (1985) and since that time has become established as a method for dating sediments that have had exposure to sunlight. The accuracy of this method was first demonstrated on a pond silt that had been dated at 58.8±.3 ka (^{14}C) and 64±12 ka (thermoluminescence, TL); the optical age of 62±8 ka is in agreement with both the TL and ^{14}C estimates

(Huntley *et al.*, 1985).

Coarse material

Dry aeolian deposits that are relatively free of organic material lend themselves particularly well to the optical dating technique since it is in these samples that solar resetting is likely to be most complete. It is for these samples also that the optical dating technique is most needed since the lack of organic material precludes the possibility of ^{14}C dating. Ollerhead *et al.* (1994) dated a sequence of young (less than 1000 year old) sand dunes at Buctouche Spit, New Brunswick. The optical ages obtained were consistent with the TL ages as well as estimates based on geomorphic evidence. In this case, the use of the thermal transfer correction was critical in obtaining a zero age for the zero age sample.

Optical dating was used in a study of Holocene dune activity in the Great Sand Hills region of Southern Saskatchewan (Wolfe *et al.*, 1995). The lack of materials datable by ^{14}C and the young ages of several of the dunes meant that optical or thermoluminescence dating was the only option available for dating the deposits. Unfortunately no independent ages are available for comparison of the youngest optical ages obtained at this site.

Duller (1994) obtained satisfactory optical ages from coarse-grained K-feldspar extracted from a sequence of sand dunes from southern North Island, New Zealand. Duller suggested that the underestimation of the age of the oldest of the samples might be due to long term fading of the luminescence signal over a period greater than 130 ka.

Inclusions, probably feldspars, in quartz grains from a series of stranded beach dunes in southeast South Australia have been dated by Huntley *et al.* (1993a). The optical ages are consistent with the expected seriation for the dunes as well as the ages deduced from oxygen isotope correlation over a time span of 0–400 ka. This is the only study in which accurate optical ages have been obtained for samples over 100 ka[13].

[13]TL dates up to 800 ka have been reported by Berger *et al.* (1992) and Huntley *et al.* (1993b).

Fine material

Loess[14], being of aeolian origin, should lend itself well to optical dating. Musson and Wintle (1994) (see Section 1.3.2) consistently obtained age underestimates for Czech loess samples that had been geologically estimated to be ~100 ka. The authors attributed this to a possible decay of the luminescence centres over the time of deposition (~100–150 ka). In loess samples collected at 5 different sites around the world, Li and Wintle (1992) found that all samples displayed similar stability in their infrared stimulated luminescence and TL signals. Comparison of a Chinese loess sample with a coarse-grained K-feldspar sand separate from New Zealand indicated that the latter was the more stable when subjected to storage at elevated temperature. Li and Wintle believe that this reflects the difference in mineral composition of the two extracts; the loess samples contains a significant amount of Na-feldspar as well as K-feldspar.

Satisfactory optical ages were obtained for $\lesssim$100 ka organic-rich sediments by Lian *et al.* (1995). The fine peaty sediments chosen for this study were deposited by slow moving water so that it is likely that the minerals obtained sufficient exposure to sunlight prior to deposition. Optical dating of sediments deposited by high-energy fluvial processes (*e.g.* floods) is more problematic since the level of solar resetting may be insufficient, particularly if the sediment charge in the river is high. Incomplete bleaching of glaciofluvial outwash sediments has been reported by Duller (1994) and Li (1994). Lang (1994) obtained anomalously old ages for poorly bleached flood deposits; the poor bleaching was attributed to high suspended sediment loads and the coagulation of clay around the sand grains. Aitken and Xie (1992) suggested subtracting later portions of the luminescence decay curve from the initial decay in an attempt to isolate the easily bleached component of the luminescence. Fuller *et al.* (1994) made an unsuccessful attempt at dating poorly bleached alluvial sediments from the Danube using a "partial bleach"[15] methodology similar to that used in TL

[14]Aeolian silt deposits

[15]In the partial bleach method a dose+bleached line is constructed as in the thermal transfer correction, however the laboratory bleach should be less complete than that received in nature. The partial bleach should not be confused with the the thermal transfer correction; the motivations for the two are different despite their similarities.

dating.

Underwater bleaching

Ditlefsen (1992) performed a laboratory experiment in which the underwater bleaching of suspended K-feldspar grains was measured. Ditlefson found nearly complete bleaching for dilute grain suspensions of less than 0.02 g/l after 20 hours of artificial insolation. In suspensions of density greater than about 0.05 g/l very little reduction in the natural luminescence signal occurred, even after 20 hours of bleaching. A similar study was undertaken by Rendell et al. (1994) on quartz and K-feldspar grains exposed to an underwater sunlight bleach at different water depths. The results of this experiment however are difficult to interpret since the bleach was undertaken under natural conditions (in the English Channel near Plymouth) and the turbidity of the water was not known. Three hours of sunlight exposure at a water depth of 10–14 m resulted in a nearly complete bleach.

There are four points in the above discussion that are particularly relevant to my study and should be emphasized. One should note that there has been very little work done on <1000 year old samples and consequently there is little or no evidence that correct ages may be obtained for 300 year old sediments. Thermal fading has only been observed (possibly) in samples of the order 100 ka old, so that thermal fading should not be a problem for samples younger than 1 ka. On the other hand, anomalous fading of the luminescence stimulated by 1.4 eV excitation has been consistently observed in feldspars and is a problem that must be considered in any dating experiment. Finally, light exposure prior to deposition is critical in water-laid samples. For this reason, an assessment of the level of solar resetting present in the source materials of the dated deposits should be undertaken as a control measure whenever possible.

Chapter 2

The Samples

2.1 Sample sites and stratigraphy

The objective of this part of the study was to sample sand layers deposited by tsunamis. Since sand may be deposited during storms or floods the sampling sites must be carefully selected to avoid the likelihood of sampling such deposits. The west coast of Vancouver Island has numerous long inlets and channels, the longest being Alberni Inlet which traverses no less than 2/3 of the width of the island. Since the heads of these fjords are far removed from the coast they are immune for the most part from the effects of Pacific storms. For this reason, the deposition of sand or mud in the lowlands or marshes at the head of of these inlets as a result of a Pacific storm is unlikely. In this case, the only source for mud and sand deposits in these marshes, aside from tsunamis, is from floods (if a river happens to be near the marsh). It is in such tidal marshes that the Vancouver Island tsunami samples were collected. In the absence of fluvial input, a sand deposit in such a marsh is best explained by an earthquake-generated tsunami, as occurred at Port Alberni in 1964 (Clague *et al.*, 1994). The possibility of fluvial input at most of the sites studied could not be ruled out. Some sites, notably Zeballos, Fair Harbour and the Niawiakum River are near streams. At the Niawiakum River in Washington, the purported tsunami sand layer was sampled from the embankment of a river cutting through a tidal marsh.

The sampled Vancouver Island sites were at Fair Harbour, Koprino Harbour, Neroutsos Inlet and Zeballos. The locations of these sites as well as the Niawiakum River site in Washington are shown in Figure 1.2. The stratigraphies of the marshes at Fair Harbour, Koprino Harbour and Neroutsos Inlet were extensively mapped and studied by Benson (1996). At the Vancouver Island sites two thin sand sheets are found embedded in the marsh peat. The uppermost sand layer is typically found at a depth of 5 to 10 cm, the lower sand layer being found at a depth of 30 to 70 cm. The sand sheets are typically less than 2 cm thick and consist of massive to normally graded fine to coarse sand (Benson, 1996)[1]. In some locations the sand layer comprises two or three sand/mud couplets (Benson, 1996). Each of these couplets consists of normally graded sand overlain by sandy mud or peat. These couplets are best explained by deposits left by a series of tsunami surges. There was no straightforward evidence for land-level change at the time of the sand deposition of the lower sand sheet at the sites described by Benson. Diatom assemblages in the peat layers above and below the sands both indicate a middle tidal-marsh environment.

Benson made the following observations with regards to the stratigraphy at the Fair Harbour, Koprino Harbour and Neroutsos Inlet marshes:

- Each sand layer covers an old marsh surface with relief similar to that of the present-day marsh surface.
- The sand sheets thin and fine landward, away from the tidal channels.
- The 300-year-old sand layer at Fair Harbour contains marine microfossils which are not found on the modern marsh.
- In some locations the sand sheets are normally graded or comprise two or more sand–mud couplets. This indicates one or more discrete surges of water followed by settling of sediments out of suspension.

These characteristics are consistent with one or more tsunami sources for the deposits and are not fully consistent with other depositional processes such as floods or storm surges. A flood deposit would not contain a significant amount of marine

[1]Massive refers to ungraded sediment of uniform density and grain size composition. Normally graded refers to sediment which fines upwards, as is found in sediment which has settled out of water.

microfossils thus, at Fair Harbour a marine origin is indicated. Benson points out that storm surges tend to erode shoreline material rather than lead to landward deposition of sediment. This, along with the fact the marsh sites are well sheltered from Pacific storms means that deposition of the sands during a storm surge is unlikely. The sand sheets at the Fair Harbour, Koprino Harbour and Neroutsos inlet sites are therefore best explained by tsunami deposition.

A summary description of the samples collected is given in Table 2.1 and the stratigraphy at each site is depicted in Figure 2.1. Maps of the sample sites are shown in Figures 2.4–2.6.

2.1.1 Washington coast: the Niawiakum River

The Niawiakum River flows into a shallow estuarine bay (Willapa Bay), the river mouth being situated directly east of the town of Bay Center, Washington, U.S.A. The mouth of the river is shielded from the Pacific by a long low peninsula, directly west of the river across Willapa Bay, which can easily be breached during a large storm. The river cuts through a brackish marsh, exposing the uppermost several metres of sediments along its banks. At a depth of 60 cm below the modern marsh surface, one finds a series of 4 to 5 sand–mud couplets approximately 1 cm thick. Each couplet comprises normally graded fine to coarse sand overlain by fine sand or mud. These sand layers are depicted as a single sand layer in Figure 2.1. This sequence of sand–mud couplets is overlain by a layer of mud that grades into peat near the marsh surface. Directly below the sand layers is a dark peaty soil similar to that of the modern marsh. The contact between the lower peat and the sand layers is sharp. This stratigraphy implies the past sudden change from a high marsh environment to an intertidal mud-flat environment. The sand-mud couplets are best explained as deposits left during the passage of a tsunami wave train, each wave having left a separate, graded deposit (the coarser material having fallen out of suspension before the fines) (Atwater, 1987; Reinhart and Bourgeois, 1989). At each successive bend in the river, the sand layer is thickest at the seaward side of the bend, thinning in the upriver direction (B. F. Atwater, written communication May 1995). This

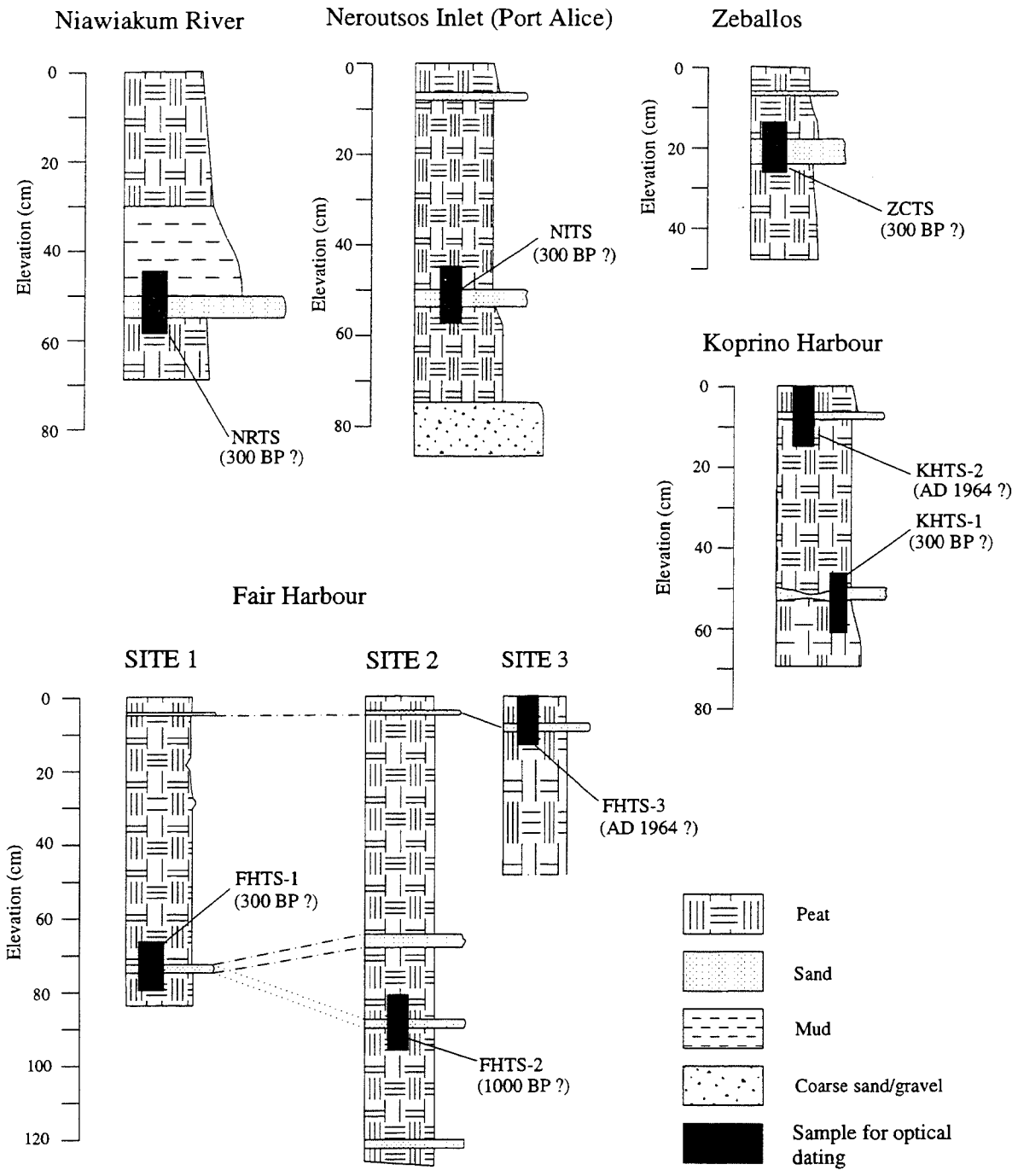

Figure 2.1: Stratigraphy of uppermost marsh sediment at locations shown in Figure 1.2. Based on field notes of J.J. Clague (personal communication, 1995).

Table 2.1: West coast tsunami deposits collected for optical dating

Sample name	Sample site and collection date	Description
NRTS	Niawiakum River, WA May 21/95	Monolith collected 100 m east of Hwy. 101 at the Niawiakum R. bridge from outcrop on north side of the river (46° 37.89' N, 123° 55.17' W). Sample was stored in a 4 *l* paint tin. Comprises 4 or 5 sand/mud layer couplets bounded by fine mud above and muddy peat below. Total thickness of sandy interval is approximately 5 cm. Top of sand layer is 60 cm below the modern marsh surface. Expected age is 300 years.
NRCB	Niawiakum River, WA Aug. 16/95	Collected at low tide from the deepest part of the river (4 m below water surface at low tide) by pushing an opaque 6 m long PVC pipe into the channel mud. Location was 50 m downriver from the NRTS sample section. Collected under supervision of Brian F. Atwater.
NITS	Neroutsos Inlet, BC (Port Alice) June 10/95	Monolith was cut from outcrop in tidal marsh channel (50° 20.4' N, 127° 26.0' W) and placed in 4 *l* paint tin. Sampled sand layer is 4 cm thick. Top of sand layer is 50 cm below marsh surface. Expected age is 300 years.
KHTS-1	Koprino Harbour, BC June 11/95	Monolith cut from outcrop in tidal channel (50° 30.3' N, 127° 49.9' W) and placed in 4 *l* paint tin. Sand layer is sporadic through the marsh and of variable thickness (less than 1 cm typically). Sampled zone includes a 5 cm thick sand layer. Top of sand layer is 30 cm below the modern marsh surface. Expected age is 300 years.
KHTS-2	Koprino Harbour, BC June 11/95	Monolith cut from outcrop in tidal channel (50° 30.3' N, 127° 49.9' W) and placed in 4 *l* paint tin. 1.5 cm sand layer is bounded by peat above and below. Top of sand layer is 6 cm below the marsh surface. Hypothesized to be a tsunami deposit from the 1964 Alaska earthquake.

Table 2.1 (continued)

Sample name	Sample site and collection date	Description
KHCB	Koprino Harbour, BC June 11/95	Sample from the channel floor collected 15 m west of KHTS-2. Obtained by pushing a 1 *l* paint tin into the sediment.
ZCTS	Zeballos, BC June 13/95	Monolith cut from wall of a pit dug approximately 50 m south from most easterly tidal channel (49° 58.9' N, 126° 50.8' W) and placed in 4 *l* paint tin. Fine sand layer 8 cm thick is overlain by muddy peat. Upper contact is 17 cm below marsh surface. Expected age is 300 years.
FHTS-1	Fair Harbour, BC June 15/95	Monolith cut from outcrop in main tidal channel 200–300 m west of the Kaouk River (50° 3.6' N, 127° 5.8' W) and placed in 4 *l* paint tin. Sand layer is 3 cm thick and lies 73 cm below the modern marsh surface. Sand is bounded by peat above and below. Expected age is 300 years.
FHTS-2	Fair Harbour, BC June 15/95	Monolith cut from outcrop in small tidal channel northeast of FHTS-1 and placed in aluminum foil and plastic bag. The 2-cm-thick sand deposit is overlain and underlain by peat and is 90 cm below the modern marsh surface. Expected age for this deposit is < 500 years.
FHTS-3	Fair Harbour, BC June 15/95	Monolith cut from outcrop in main tidal channel approximately 50 m southwest of FHTS-1, and placed in aluminum foil and plastic bag. Sand layer lies 6 cm below the marsh surface, is 1.5–2 cm thick and is bounded by peat. Hypothesized to be a tsunami deposit from the Alaska 1964 earthquake.
FHCB	Fair Harbour, BC June 15/95	Channel-bottom sample collected approximately 20 m west of FHTS-1 along the main channel. Obtained by pushing a 1 *l* paint tin into the sediment.

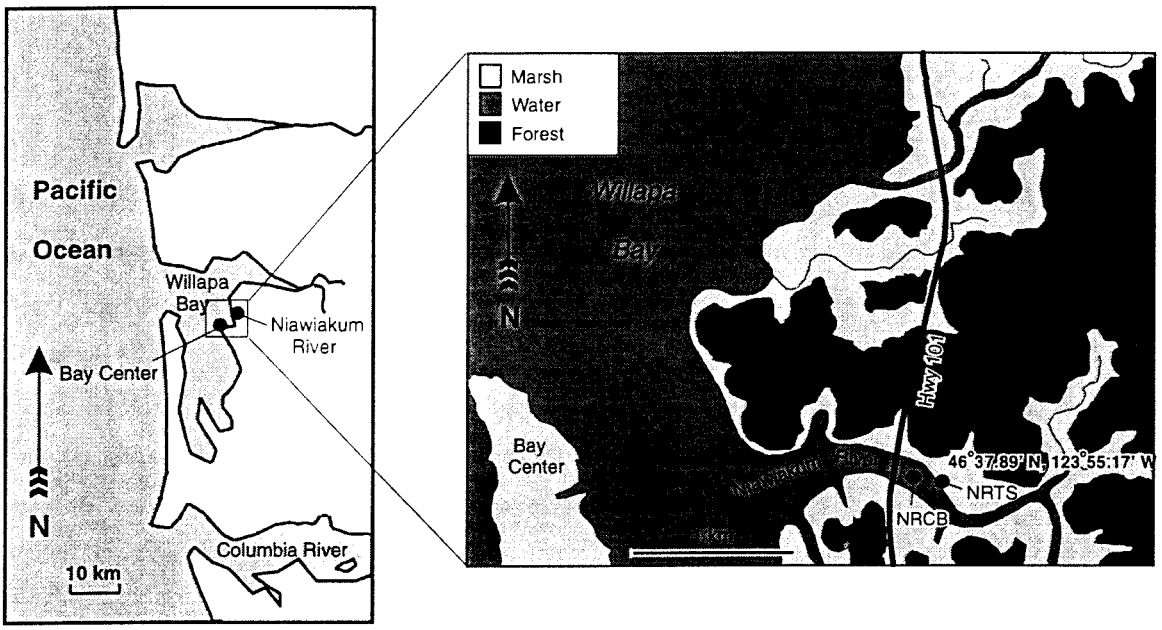

Figure 2.2: Niawiakum River estuary showing locations of collected samples. NRTS is a sample of the tsunami deposit, NRCB is a channel-bottom sample collected by B. F. Atwater.

is suggestive of deposition by a landward surge of water. As the water breached successive bends in the river, sand was deposited on the seaward side of each bend. Radiocarbon ages obtained from 3 spruce stumps at the Niawiakum River and at nearby Bay Center beach gave a most likely age range for the time of tree death between A.D. 1695 and A.D. 1710 (Atwater and Yamaguchi, 1991).

The water in the river at this site is particularly turbid, the river banks and bed being composed of mud. Sediment in the bottom of the channel was sampled for optical dating (sample NRCB) to determine the level of solar resetting in this material. This was of interest given the possibility that the tsunami-deposited sands may have originated from material scoured from the bottom of the river. The sample for optical dating, NRTS, was cut from the northern bank of the river approximately 100 m east of Highway 101.

2.1.2 Vancouver Island sites

Fair Harbour

The marsh at Fair Harbour is located at the mouth of the Kaouk River. Numerous Islands and winding channels protect this site from the open ocean 20 km away. Two sand sheets are found throughout the marsh in the approximately 1 m thick peat bed. The topmost at a depth of $\sim$ 6–10 cm averages at 0.5 to 1.0 cm thick while the lowermost lies at a depth of 60–70 cm below the marsh surface and is 1.5 to 2.0 cm thick on average (Benson, 1996). The typically massive lower sand sheet consists of fine to coarse sand but is locally comprised of 2 to 3 sand/mud couplets. The clean, coarse basal sand in each couplet is overlain by fine sand or mud (Benson, 1996). The upper sand sheet is typically massive but locally contains up to 3 couplets of coarse to fine sand overlain by mud (Benson, 1996). The sand sheets thin and fine away from the tidal channels towards the forest edge, which suggests deposition during a landward directed surge flowing out of the tidal channels.

Two other sand sheets are found depths of 90 cm and 123 cm but are restricted to the vicinity of one of the smaller tidal channels in the marsh (see the FHTS-2 sample site in Figure 2.3). The sand sheet at 90 cm depth had no noticeable grading, was approximately 2 cm thick and consisted of fine to coarse sand intermixed with peat. These sand sheets were probably deposited during a flood in a nearby gully rather than a tsunami, although this was not known at the time the layer at 90 cm depth was sampled (sample FHTS-2).

There is no stratigraphic evidence for land-level change at the time of deposition of the 60-cm-depth sand sheet. Diatom assemblages in the peat directly above and below this deposit indicate a middle-marsh environment (Benson, 1996). The 60-cm-depth sand layer contains marine diatoms that are not found in the modern marsh peat, suggesting a marine rather than fluvial origin (Benson, 1996).

The peat bed of the marsh is underlain by sand and gravel. Radiocarbon ages of a stick found at the peat-gravel interface indicates that peat accumulation in the marsh began less than 550 calibrated ^{14}C years ago (Benson, 1996). Radiocarbon ages of sticks found near the 60-cm-depth sand layer are consistent with an age of less than

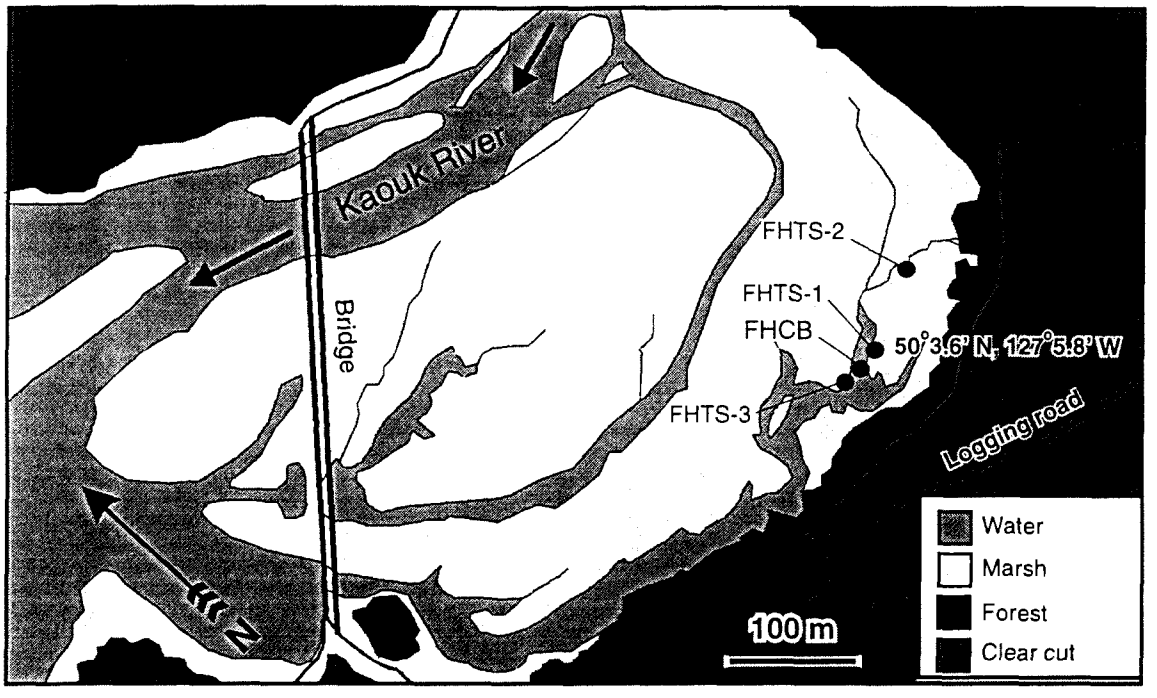

Figure 2.3: Marsh at Fair Harbour showing locations of samples collected for optical dating. FHTS-1 and FHTS-3 are samples of tsunami deposits, FHCB is a sample of channel bottom mud. FHTS-2 is a sample of a flood deposit originally believed to be a tsunami deposit.

500 years for this deposit (Table 2.2).

Measurements of cesium activity in the upper peat revealed a marked increase in ^{137}Cs activity near the upper sand sheet (Benson, 1996). This increase in ^{137}Cs activity is due to atmospheric testing of nuclear weapons which began in the early 1950's and peaked around 1964. This is consistent with the hypothesis that the upper sand sheet was deposited by the tsunami generated by the 1964 Alaska earthquake[2].

Samples of the 60-cm-depth sand, FHTS-1, and the uppermost sand sheet, FHTS-3 were collected from outcrops in the main tidal channel cutting through the marsh (see Figure 2.3). A sample of the channel bottom sediment, FHCB, was collected 20 m downstream from the FHTS-1 sampling site. The purpose of this last sample was to

[2]The 1964 tsunami destroyed two bridges crossing the Fair Harbour marsh (Benson, 1996).

Table 2.2: Radiocarbon ages for deposits at Fair Harbour, Koprino Harbour and Neroutsos Inlet, after Benson (1996), reproduced with permission. Radiocarbon age uncertainties are quoted at 1 σ unless marked by a † which indicates a 2 σ uncertainty.

Location	Laboratory number[1]	Radiocarbon age (^{14}C yr B.P.)	Calendar age range (yr A.D.)	Dated material and stratigraphic position
Neroutsos Inlet	TO-5314	230±50	1444–1950	Bark fragment on lower sand
Koprino Harbour	TO-5315	40±50	1659–1950	*Triglochin* leaf bases in lower sand
Koprino Harbour	QL-4806	161±16	1670–1950	*Triglochin* leaf bases in lower sand
Fair Harbour	GSC-6006	510±80, 420±80 †	1331–1628	Stick, 6–10 cm above lower sand
Fair Harbour	TO-5317	6930±80	6115–5599 B.C.	Stick, 0.5 cm above lower sand
Fair Harbour	GSC-6018	270±80 †	1444-1950	Stick, 2–3 cm below lower sand
Fair Harbour	GSC-6030	300±80, 290±80 †	1449-1950	*Juniperus* stick at base of peat
Fair Harbour	TO-5316	60±50	1653–1950	*Tsuga heterophylla* cone on lower sand

[1] GSC: Geological Survey of Canada; TO: Isotrace Laboratory; UW: University of Washington

determine the level of solar resetting present in this material. This was of interest given the possibility that the channel bottom sediments were the source of the tsunami deposits. A sample of the 90-cm-depth sand from the small tidal channel 100 m east-north-east of the FHTS-1 sample site was collected and designated FHTS-2.

Koprino Harbour

Koprino Harbour is located on the north side of Quatsino Sound, less than 20 km away from the open ocean and 12 km east of Winter Harbour. A small marsh in Koprino Harbour is protected by an island (Schloss Island) as well as a ~600 m long peninsula which almost isolates the marsh from Koprino harbour. A tidal channel runs the length of the marsh ending in a small creek at the marsh's eastern limit; I designate this the "main tidal channel".

Two sand layers are present in the ~70 cm thick peat bed of the marsh (Benson, 1996). The uppermost sand sheet is 0.5 cm thick, consists of fine sand and lies 5–8 cm below the marsh surface on average (Benson, 1996). On the basis of stratigraphic position, this sand sheet is probably contemporaneous with the sand sheet deposited at Fair Harbour by the 1964 tsunami. The lowermost sand layer is 1.0 cm thick on average (locally up to 5.0 cm thick), lies 60–70 cm below the marsh surface and consists of fine to very coarse sand (Table 2.2). A radiocarbon age on *Triglochin* leaf bases rooted in the lower sand indicates that this sand layer was deposited less than 340 years ago (Benson, 1996). Both sand sheets thin and fine away from the main tidal channel (Benson, 1996).

Samples for optical dating of the upper and lower sand layers were cut from outcrops in the main channel approximately 100 m from the eastern extremity of the marsh. These were designated KHTS-2 and KHTS-1 respectively. The lower sand layer here was 5 cm thick, much thicker than the typical 1 cm thickness of this sand sheet in other parts of the marsh. A sample of the channel bottom sediment, KHCB, was collected 15 m east of the KHTS-2 sample site.

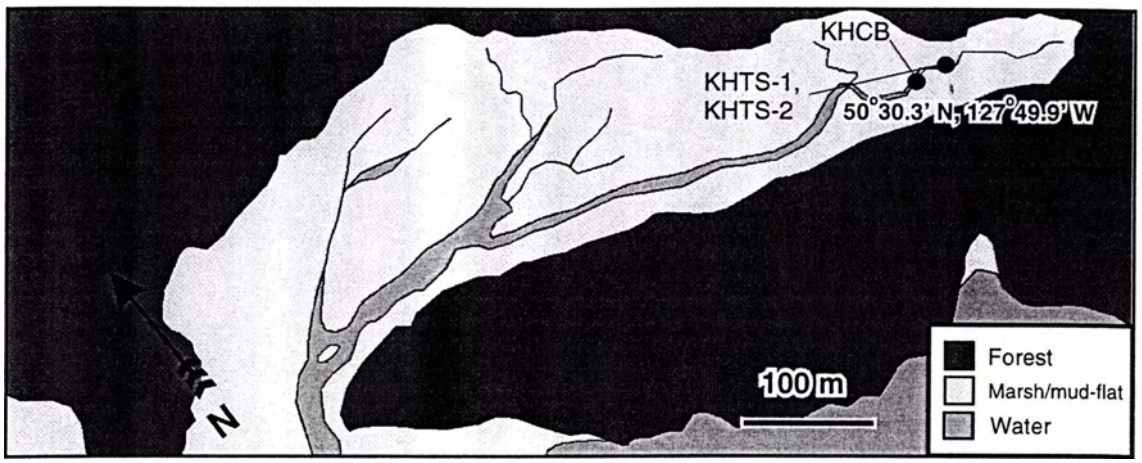

Figure 2.4: *Top:* The marsh at Koprino Harbour showing locations of samples collected for optical dating. KHTS-1 and KHTS-2 are samples of tsunami deposits, KHCB is a sample of the channel-bottom sand/mud. *Bottom:* Stratigraphy of the sampled section at Koprino Harbour. Knife handle (left and up from center) indicates the 1964 tsunami sand layer. The 300-year-old layer is most clearly seen to the lower right as a dark gray sediment. Lens cap in photo is 6 cm in diameter.

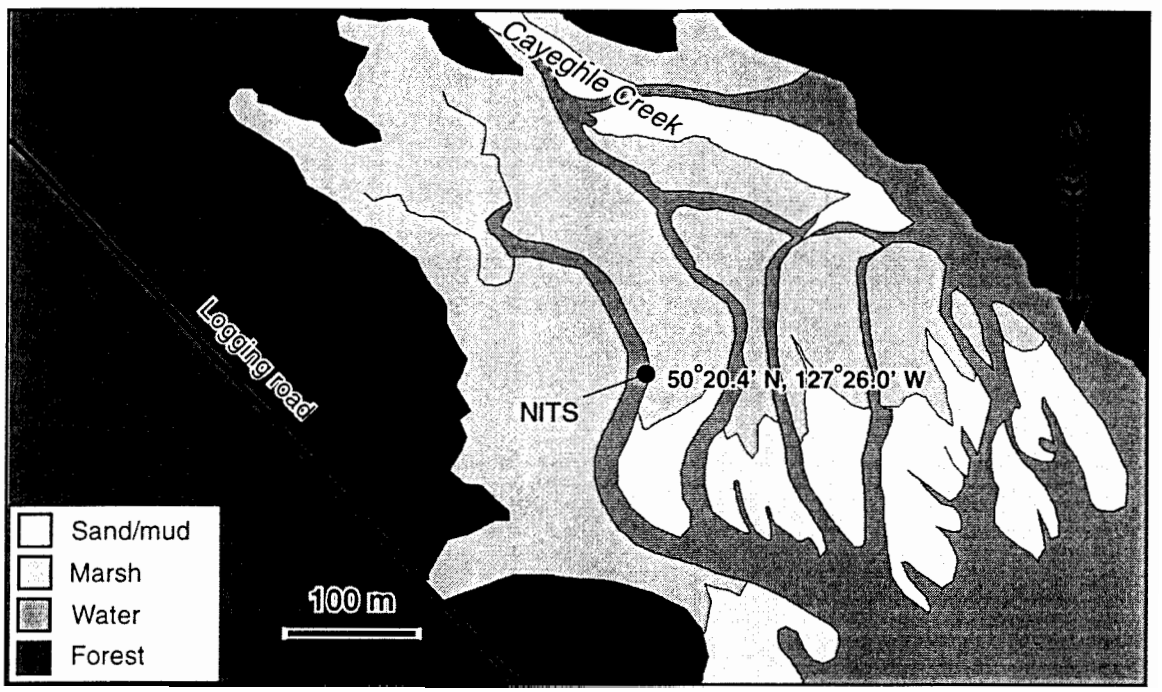

Figure 2.5: Marsh at Neroutsos Inlet showing location of sample collected for optical dating, NITS.

Neroutsos Inlet

Neroutsos Inlet is a 20 km long fjord which branches southward off the eastern extremity of Quatsino Sound. At the southern extremity of Neroutsos inlet a marsh is found near the mouth of Cayeghle Creek (approximately 5 km south of the town of Port Alice). Over 50 km of narrow inlets and channels isolate this site from the mouth of Quatsino Sound, sheltering it from Pacific storms.

Two sand sheets are found at this site. The uppermost layer consists of fine to coarse massive sand 0.5 to 2 cm thick which lies 4 to 12 cm below the marsh surface (Benson, 1996). The lower sand layer is typically massive but is locally normally graded and consists of medium to very coarse sand 1 to 2 cm thick at a depth of 40 to 60 cm below the marsh surface (Benson, 1996). A bark fragment on the lower sand yielded a calibrated radiocarbon age between 0 and 550 years (Table 2.2). The upper

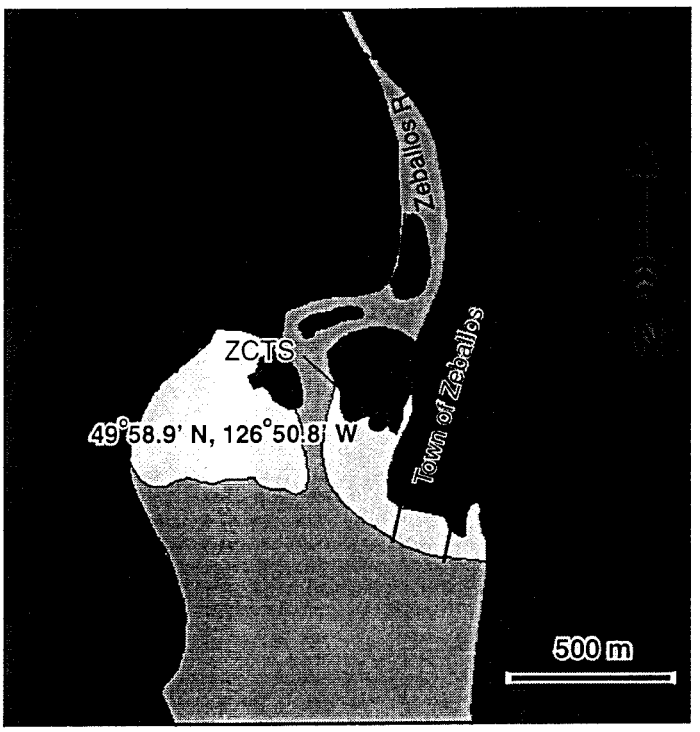

Figure 2.6: Zeballos estuary showing location of sample collected for optical dating, ZCTS.

sand layer was probably deposited by the 1964 tsunami given the similarity in the stratigraphic position of this deposit with the upper sand sheets at Fair Harbour and Koprino Harbour.

Only the lower sand layer was sampled for optical dating at this site. The sample, designated NITS was removed from the bank of a large tidal channel on the northeast side of the marsh, away from Cayeghle Creek.

Zeballos

Zeballos is a town at the northern end of Zeballos inlet which branches northward off Esperanza Inlet. The marsh west of the town is divided by the Zeballos River which flows south into Zeballos Inlet; fluvial input is therefore a possibility at this site. The site is well protected from the open ocean by 25 km of narrow inlets and a

few small islands.

The stratigraphy at Zeballos differs considerably from the other Vancouver Island sites. Two sand layers were observed. The upper sand layer is only distinguished with great difficulty ~8 cm below the marsh surface. The lower sand layer was both much thicker and finer grained than at the previously mentioned sites. It is sharply bounded by underlying peat and is approximately 10 cm thick. The upper contact of the sand layer is gradational into the overlying peat. Unexpectedly large quantities of freshwater diatoms were found in this sand layer, suggesting a fluvial rather than marine source[3]. The lower layer was sampled from the wall of a pit dug 50 m east of the most easterly tidal channel. This sample was designated ZCTS.

2.2 Sample collection

The samples were collected as monoliths cut from the walls of tidal channels or dug pits. Care was taken to include a large section of the bounding peat or mud for dosimetry measurements and to prevent the sample from crumbling during transport. Samples were wrapped in aluminum foil, placed in a sealed bag and stored in 4 *l* paint tins to prevent exposure to light[4]. Separate samples were collected for analysis of water content of the peats above and below the sands due to the possibility that water might drain from one section of the monolith to another during transport or storage. Water contents of the sands were measured in the laboratory (at most 5 months after collection) by using a 1-cm-diameter by 10-cm-long coring tool; this would preferably have been done in the field to avoid the problem of water draining from the sand during the storage period.

In most cases the sand layers were 1 cm to 3 cm thick and contained large amounts of peat and silt. This had two important consequences for dating. Firstly, the amount of material available for dating was very small. This was important because, for some samples, there was just enough material for a single evaluation of the equivalent dose

[3]J. J. Clague, personal communication, 1997.

[4]Placing the sample in a plastic bag prior to wrapping in foil would have been better as salt water rapidly corroded the aluminum foil.

and an anomalous fading experiment (sample NITS for example). The thinness of the sand layers also meant that the dosimetry calculations for the sand were relatively complicated. Radioisotope concentrations and water contents were required for the bounding sediments as well as the sand itself. Uncertainties in the geometries of the samples proved important when assessing the error limits of the calculated dose rates.

2.3 Sample preparation

In the laboratory, the outermost centimeter of each monolith was discarded to avoid inclusion of sand exposed to light during sampling. In most cases the sand layer, including up to 0.5 cm of the bounding sediment layers, was cut out of the sample block and rinsed until most of the finer silt had been decanted away. This proved to be a wasteful use of material since much of the sand was embedded in peat. Rinsing the samples on a 90 μm sieve proved to be more efficient; the amount of sand remaining in peaty clumps after rinsing was negligible. The rinsed sand was left in a $\sim$10% HCl solution overnight to remove any carbonates (present in relatively small amounts in most samples), followed by overnight treatment (or longer as appropriate) with $\sim$10% H_2O_2 to remove most of the remaining, often significant, organic fraction. The clean sand was then dried at 60–70°C and the 125–180 μm grain size fraction isolated by sieving; in the absence of sufficient material of this grain size, the 90–125 μm or 180–250 μm fraction was used. The selected grains were subjected to a second $\sim$10% H_2O_2 treatment to remove any remaining organics. A high-potassium feldspar content fraction was extracted using a density separation with a 2.58 g/ml solution of sodium polytungstate. Quartz, albite and anorthoclase have densities >2.58 g/ml and therefore sink in the sodium polytungstate solution whereas orthoclase floats. This density separation was repeated in order to obtain a purer K-feldspar fraction. This fraction was then etched for 3–4 minutes in $\sim$5% HF, followed by a rinse in $\sim$10% HCl to remove fluorites produced by the HF etch. The etched grains were rinsed over a 100 μm sieve (for the 125–180 μm fraction) to remove any smaller grains that may have been produced by the disaggregation of clumps of grains during the HF etch. The grains were then passed through a magnetic separator to remove strongly

Table 2.3: Grain mass yields at different steps in the separation process. Listed samples are representative of the different types of samples processed by the author. NRTS consists of sand intermixed with clay and silt. FHTS-1 and FHTS-3 are samples in which coarse sand is mixed with peat, FHTS-1 containing somewhat more sand than FHTS-3. NITS is notable for the low K-feldspar to quartz content ratio obtained after the density separation.

	NRTS	FHTS-1	FHTS-3	NITS
Estimated initial mass of sample (g)	500	1000	500	400
Total mass after rinsing and drying (g)	39	314	201†	195
Mass of separated grain-size fraction (g)	7.73	28.4	46.6	15.7
Mass of K-feldspar separate, 1^{st} separation (g)	2.94	—	2.36	1.60
Mass of K-feldspar separate, 2^{nd} separation (g)	2.15	2.03	1.46	1.03
Mass of etched and wet sieved separate (g)	0.420	1.190	0.608	0.269
Mass of non-magnetic fraction (g)	0.266	1.131	0.573	0.230

† Sample initially rinsed over a 90-125 μm mesh sieve.

paramagnetic grains. The grains remaining after this process will be referred to as the "K-feldspar" fraction, although, as will be seen, this fraction contained a significant amount of quartz and other minerals.

Grains thus prepared were ready for luminescence measurements. Prepared aliquots consisted of approximately 5–10 mg of the separated K-feldspar fraction evenly spread on 1 cm diameter aluminum planchets. The planchets were coated with a thick layer (*i.e.* deep enough to cover the grains) of 500 cs silicone oil prior to deposition of the grains.

Table 2.3 shows the mass remaining after each step in the separation process. This table has been included to provide an indication of the low yield of datable material obtained for each sample; this imposed a severe limitation on the number of separate planchets that could be measured for some of the samples.

Chapter 3

The Luminescence Detection Chamber

3.1 Optical design

Since the samples used in this study are young, with ages ranging from 30 to 1000 years old, much effort was made to design a luminescence detection chamber with improved sensitivity over the old single aliquot measurement chamber[1]. There are three ways to increase the photo-stimulated luminescence count rate: (1) by improving the light collection efficiency, (2) by increasing the infrared (IR) illumination flux at the aliquot, or (3) by warming the aliquot. My approach was to use the first two methods. The third method requires careful control of temperature and has never been used (to my knowledge) in photo-stimulated luminescence dating, but merits attention in future work.

The new chamber is shown in Figure 3.1; the distinguishing feature is its short-focus ellipsoidal-mirror collecting element. This mirror intercepts 82%[2] of the radiation emitted from a sample planchet. For comparison, the mirror in the older apparatus intercepted only 14.5%[3] of the radiation at best, with the IR diode block

[1] A schematic diagram of the old apparatus is shown in Figure 4 of Ollerhead *et al.* (1994).
[2] A 6% loss due to the central hole in the mirror is included in this figure.
[3] 1.7% loss due to the central hole is included.

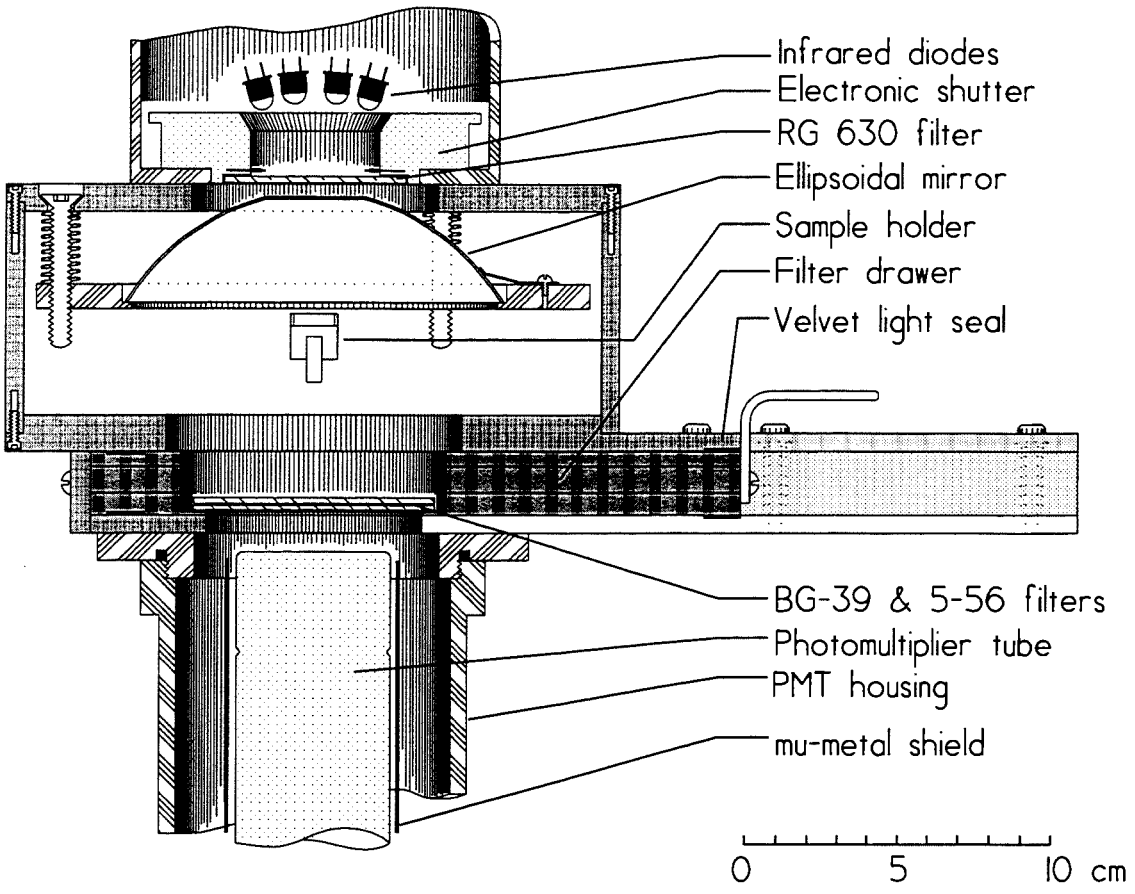

Figure 3.1: A cross-sectional view of the luminescence detection chamber.

removed.

A sample planchet is placed in the primary focal plane, P_1, of the mirror so that light emitted by the sample is brought within the vicinity of the secondary focal point Q', where it is detected by a photomultiplier tube (PMT) (see Figure 3.2). The mirror acts as a crude projection system with an object-to-image height ratio of

$$F_2/F_1 \approx 3.0 \tag{3.1}$$

where F_1 and F_2 are defined in Figure 3.2. This implies that unless additional optical elements are used, the diameter of the PMT photocathode must exceed that of the sample by roughly a factor of 3.

This light collection system only images light rays emerging near the primary focal point on the optical axis. Specifically, near-paraxial rays that emanate at a distance h from the optical axis in the plane P_1 (*e.g.* the ray labelled (a) in Figure 3.2) will cross plane P_2 at a distance further from the optical axis than would be the case for non-paraxial rays emerging from the same point. Imaging aberrations of this kind are of little concern since it is only the light-concentrating properties of the mirror that are of interest. One would like to know, however, the distribution of light projected on the detection plane P_2.

To investigate the properties of the collection mirror, some simple computer ray tracing was performed. The luminescent sample was modeled as an array of point sources uniformly distributed over a 1.2 cm diameter disc (this is the typical size of the aluminum planchets used to hold mineral aliquots). This array of point sources was centered at the first focus of the mirror. Each point source was in turn represented by a set of unit ray vectors, $\mathbf{r}_{inc}$, with isotropically distributed orientations. Each ray was subjected to the following computational procedure.

First, the intersection point of the ray with the ellipsoidal surface of the mirror was computed. From this, the unit normal vector $\mathbf{N}$ to the mirror surface at this intersection point was determined ($\mathbf{N}$ points out of the reflecting surface). The reflected vector, $\mathbf{r}_{ref}$, was then obtained by applying the vector reflection transformation[4],

$$\mathbf{r_{ref}} = (2\mathbf{N} \cdot \mathbf{r_{inc}})\mathbf{N} + \mathbf{r_{inc}} \tag{3.2}$$

[4]See for example p.10–13, Welford and Winston (1989).

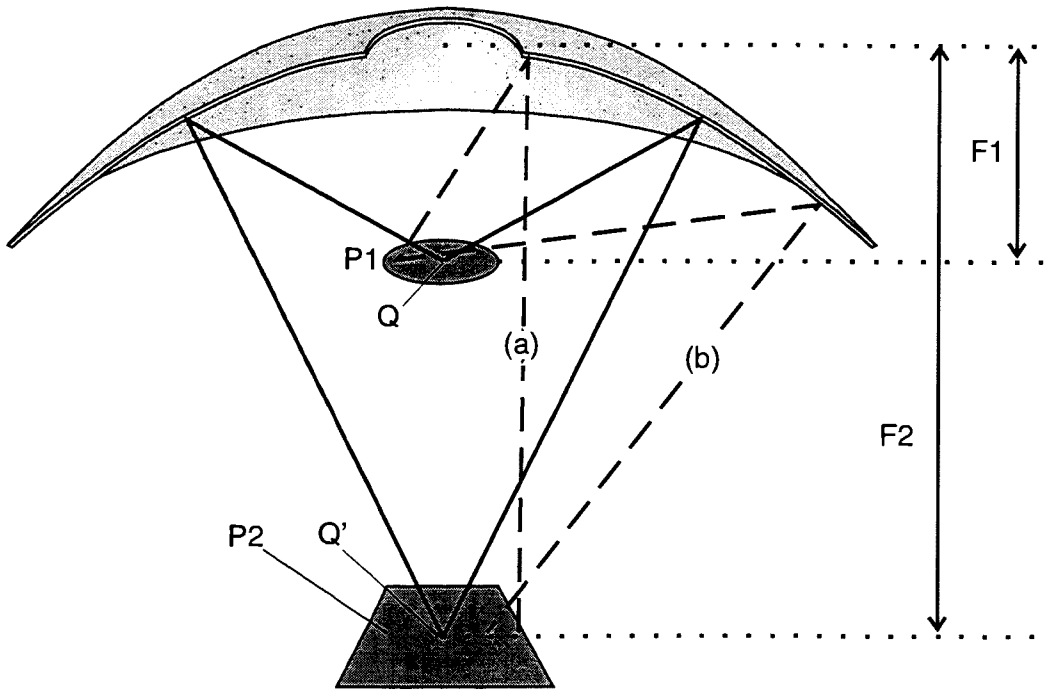

Figure 3.2: Geometry of the ellipsoidal mirror. P_1 and F_1 are the primary focal plane and focal length, respectively. P_2 and F_2 are the secondary focal plane and focal length. All rays emanating from the primary focal point Q are brought to a secondary focal point Q'. Off-axis rays (a) and (b) are not brought to the same point in the plane P2 despite their common origin in the plane P1.

It is understood in the above equation that the unit vector $\mathbf{r}_{inc}$ is directed *towards* the reflecting surface while the reflected unit ray vector points *away* from the mirror. The intersection of the reflected ray, defined by the vector $\mathbf{r}_{ref}$, with the second focal plane P_2 (see Figure 3.2) was then computed and the coordinates plotted. If this process is repeated for each ray vector emanating from the sample disk, one obtains a plot which represents the distribution of light projected on the plane P_2.

The result of such a computation is shown in Figure 3.3. The results indicate that a 4-cm-diameter PMT window would intercept almost all light emitted by the sample incident on the mirror. The diameter of the PMT window that was actually used is 5 cm. Note also that the distribution of light at the photocathode is most uniform in a plane *inside* or *outside* the focal plane. Diffusing the light in this manner may be beneficial to the operation of the PMT especially when operated at high photocurrents.

The IR illumination was originally provided by 18, OD 50L diodes[5] set in an aluminum block. The manufacturer's data sheet for these diodes shows an emission peak at 1.4 eV (880 nm) with cutoffs at 760 nm and 980 nm. The peak emission of the diodes corresponds to the 1.4 eV luminescence excitation resonance of orthoclase. The diodes were aligned for a brightest uniform illumination 7 cm from the centre of the diode block. This arrangement provided an irradiation flux at the sample of 12 mW/cm^2 with the diodes operated at 20% their maximum rated current of 500 mA and 21 mW/cm^2 at 200 mA[6]. Typical operation was at 200 mA to avoid excessive heating of the diodes. A Schott RG-630 filter was used to block the small visible component of light emitted by the diodes.

The diode block described above was not entirely suitable for the new apparatus, having been originally designed for use in the old chamber. Nevertheless, this diode configuration was used for all the normalization measurements. It was subsequently replaced by the diode block shown in Figure 3.4 which was used for all the

[5]Manufactured by the Opto Diode Corp., 914 Tourmaline Dr., Newbury Park, CA 91320, USA.

[6]Power measurements were obtained by placing a calibrated silicon photodiode detector at the sample holder.

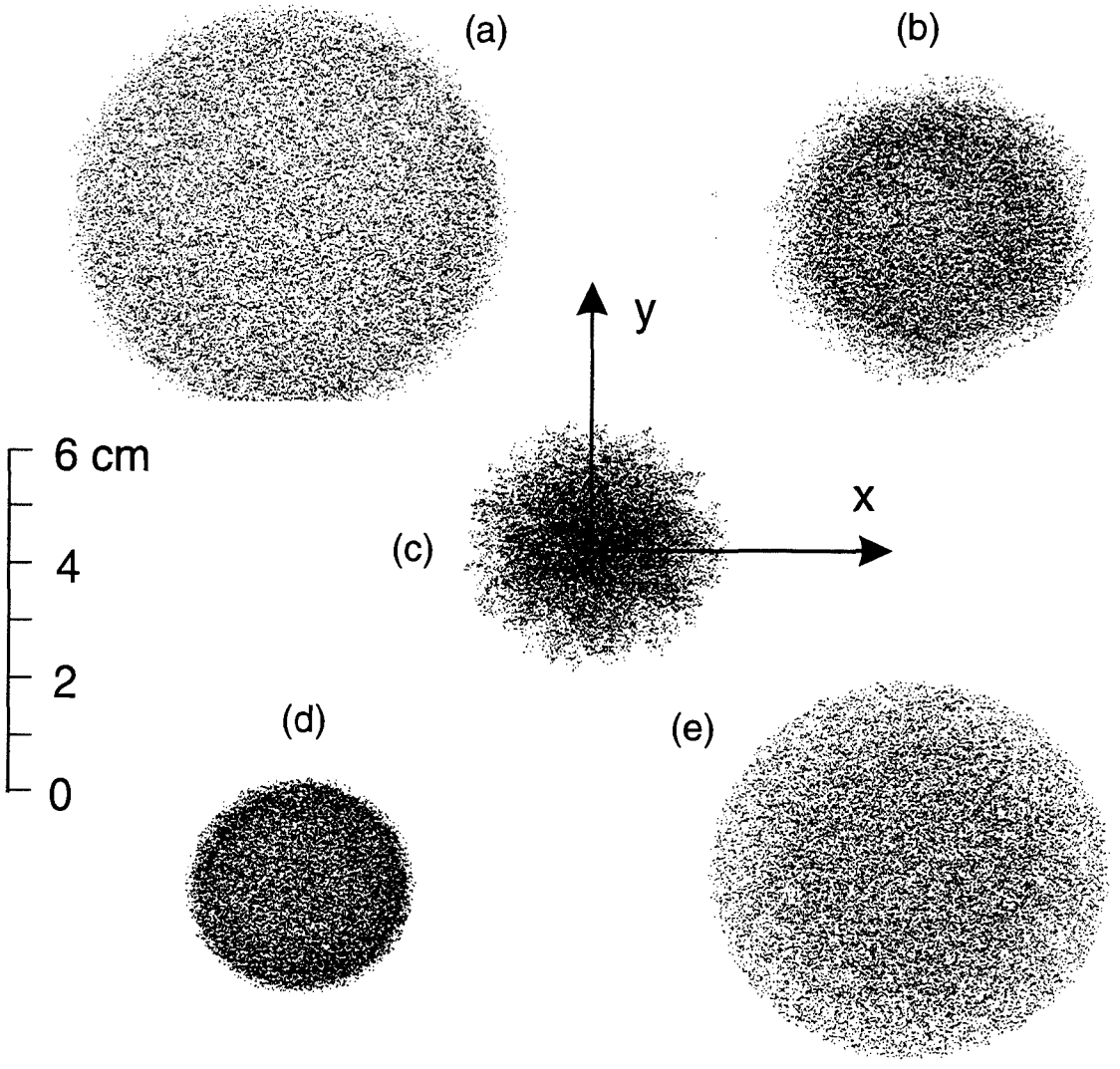

Figure 3.3: Distribution of light in the plane of the PMT photocathode ("x" and "y" refer to directions in this plane, *i.e.* perpendicular to the optical axis). Ray tracing was for an isotropically emitting, uniform disk 1.2 cm in diameter. The disk was modeled by 500 point sources, each represented by 50 isotropically oriented ray vectors. Points represent the intersection of a ray with a plane (a) 4 cm *outside* the focal plane P_2, (b) 2 cm *outside* the focus, (c) exactly at the focus, (d) 2 cm *inside* the focus and (e) 4 cm *outside* the focus. Note that the distribution of light at the focal plane P_2 is not uniform.

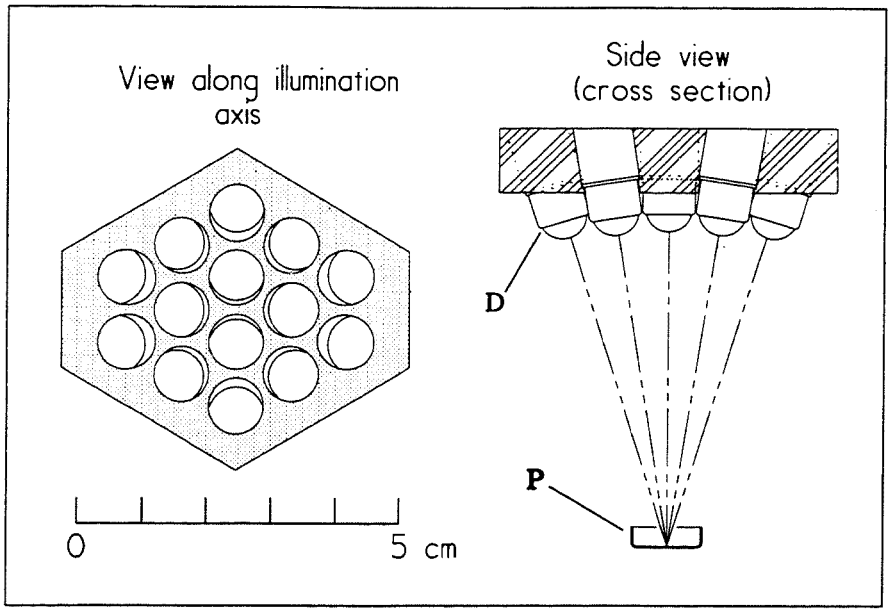

Figure 3.4: The infrared diode block. The diodes **D** illuminate the planchet **P**.

post-treatment measurements. This diode block only provided a modest improvement in illumination power – 15 mW/cm^2 with the diodes operated at 100 mA and 26 mW/cm^2 at 200 mA. The photomultiplier tube is an EMI 9635 QB with a nominal peak wavelength response at 3.3 eV (380 nm) and a cutoff at 1.9 eV (650 nm). Kopp 5-56 and Schott BG-39 filters were placed before the PMT to prevent detection of scattered 1.4 eV light from the diodes and to allow measurement of the 3.1 eV (400 nm) emission band from K-feldspar while excluding the 2.2 eV (570 nm) emission band from albite (Figure 3.5).

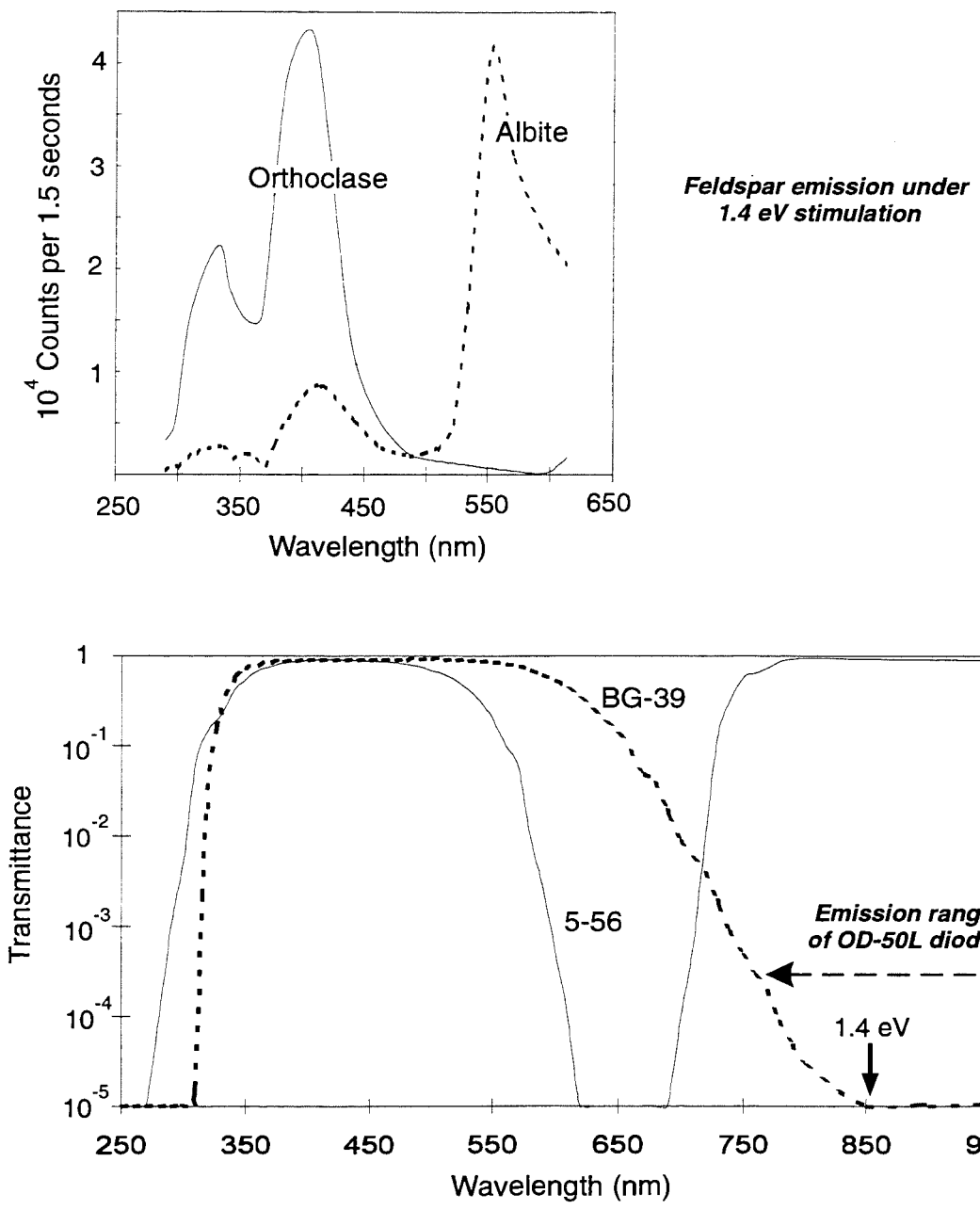

Figure 3.5: *Top*: Emission spectra of orthoclase (solid line) and albite (dashed line) under 1.4 eV (infrared) illumination (based on data provided by M.A. Short). *Bottom*: Transmission spectra of the BG-39 and Kopp 5-56 filters; these allow transmission of the blue orthoclase signal while blocking the orange emission from albite. Note also that the quantum efficiency of the EMI 9635Q photomultiplier tube at 570 nm is ~15% of that at 400 nm.

3.2 Mechanical design and electronics

Output from the PMT preamp was input to an amplifier and discriminator, and the NIM pulses from the latter were counted using a multi-channel scaling card[7] in a microcomputer. Existing software was modified to suit this new card. Control of the illumination shutter was provided via the parallel printer port on the PC. This facility circumvents the need to turn off the diode current between the measurement of each aliquot, thereby improving the power stability of the diodes.

Both the sample drawer and filter drawer are light sealed and the entire construction designed to minimize entry of light into the chamber (*eg.* all the joints between walls in the chamber are rabbetted). Particular attention was paid to the light seal on the filter drawer to allow easy interchange of filters. The positions of the mirror and diode block were made fully adjustable by mounting each on three spring-loaded screws. The IR diode housing may be easily removed to change excitation illumination sources.

Optical alignment was performed in two steps. First, the mirror was adjusted to obtain a maximum count rate at the PMT using a uniformly phosphorescing aliquot as the source. Note that this adjustment resulted in optimum detection efficiency rather than an exact geometrical alignment of the optical components; this is due in part to the variation in response across the surface of the photocathode. The orientation of the IR diode block was adjusted in a similar manner using a bright aliquot as the source and a diode power sufficiently low that the decay in luminescence was small over the time required to make the adjustment.

[7]MCS II from "Tennelec/Nucleus, Inc.", 601 Oak Ridge Turnpike, Oak Ridge, Tennessee, U.S.A. 37830, rated at 200 MHz, replacing the previous PCA board from the same manufacturer, rated at 10 MHz.

3.3 Performance of the luminescence detection chamber

A simple comparison of the solid angle subtended by the mirror with respect to the sample in the new chamber and the old apparatus[8] would suggest the detection sensitivity was improved by a factor of 5.7 times in the new design. The actual improvement in sensitivity was a factor of 4.5 ± 0.5. This difference was expected because the calculation assumed that the light emanating from the sample was uniformly distributed over a solid angle of 2π. The emission, however, is probably concentrated in a cone of solid angle less than 2π due to shadowing by the aluminum planchet walls and by the grains themselves. The simplest immediate improvement to the new detection chamber would be to increase the IR diode illumination power. The use of diodes with smaller cases[9] would allow a larger number of diodes to be mounted in the fairly restricted area of the shutter aperture.

[8] See the figures quoted in Section 3.1

[9] The OD 50L's are larger than the newer diodes of similar power that are now available.

Chapter 4

Radiation Dosimetry

4.1 Components of the radiation dose rate

The contributions to the dose rate for K-feldspar grains are the following, listed in roughly decreasing order of importance;

1) *External* β dose rate from the surrounding sand, particularly from the decay of ^{40}K to ^{40}Ca and ^{40}Ar.
2) *Internal* β dose rate from K^{40} and a small amount from Rb^{87}.
3) *External* γ dose rate from surrounding sediment from the decay of K^{40}, and from the radioactive decay series of uranium and thorium in roughly equal amounts.
4) Cosmic rays.
5) *Internal* α rays from the uranium and thorium decay chains.

In the above, the label *external* refers to radiation particles originating outside a grain, that is from the surrounding sediment. The *internal* dose is that due to radioactivity within a grain, as arises for example from the ^{40}K present in alkali feldspars.

Because γ rays have a relatively long range, typically 0.3 m in sediment, the bulk of the γ dose comes from the mud or peat surrounding the sample. Unless the sand layer is thick, the sand layer itself contributes little to its own γ dose. In what follows it will be seen that the γ dose rate is highly dependent on the geometry of the sample. In

the case of a sand layer bounded by mud or peat layers (as is the case for the present samples) the gamma dose rate contributed by the upper and lower layers must be computed separately, as well as the small self dose rate from the sand layer itself.

The range of β particles in sediment of density $2g/cm^3$ is of the order 1 mm for β's from the uranium and thorium series. The β dose acquired from sediment surrounding the sample (*i.e.* the upper and lower bounding sediment layers) is therefore negligible since all sampled sand layers are at least 1 cm thick. The β dose rate in the sand layer was taken to be that of a uniform sediment of infinite extent. The error introduced by this approximation is less than 5% based on Aitken's estimate for a 1 cm thick layer (Aitken, 1985, p. 295).

The typical range of α particles produced in the decay chains of uranium and thorium in soil (assumed density of $2g/cm^3$) is between 15 and 50 μm. For this reason, only α emitters within the grains and in the material immediately surrounding the grains could contribute significantly to the α dose rate.

The analytical results used in the computation of the dose rates are given in Table 4.1. The significance of these will be discussed in the following sections as the details of the computation of the γ, β, α and cosmic-ray dose rates are discussed separately. The results of the dose-rate calculations are summarized in Table 4.2.

Thorium and rubidium contents were obtained by neutron activation analysis (NAA) at the Slowpoke Reactor Facility of the University of Toronto. Uranium contents were determined by delayed neutron analysis (DNA), at the Saskatchewan Research Council, while potassium contents were determined by atomic absorption analysis, at Chemex Labs Ltd., North Vancouver. The term Δ in Table 4.1 is the water content expressed as the weight of water divided by the dry weight. The Δ_{sat} is the saturation water content obtained in the laboratory by immersing the sediment in water for several days until no more water was absorbed (determined by weighing). The *in situ* Δ is the water content determined from the weight of the wet sediment prior to immersion in water in the laboratory.

Table 4.1: Bulk sample analytical results used in calculating dose rates. Thorium contents for the upper and lower peats are assumed to be 2.0 $\mu g \cdot g^{-1}$; this is based on typical values found for this type of sediment; see for example, Huntley and Clague (1996).

	ZCTS	NRTS	NITS	FHTS-1
Upper mud or peat	mud	mud	peat	peat
In situ Δ	0.41	0.69	3.74	3.78
Δ_{sat}	0.41	0.72	4.03	3.81
K (%)	1.04±.05	1.64±.08	0.51±.03	0.54±.03
Th ($\mu g \cdot g^{-1}$)	[2.0]	[2.0]	[2.0]	[2.0]
U ($\mu g \cdot g^{-1}$)	0.99±.08	3.00±.1	15.2±.2	8.8 ±.2
Wet ρ ($g \cdot cm^{-3}$)	1.78	1.55	1.04	1.15
Layer thickness (cm)	22±1	60±1	50±1	73±1
Bulk sand				
In situ Δ	0.41	0.57	0.46	0.30
Δ_{sat}	0.41	0.60	0.56	0.30
K (%)	1.09±.05	1.62±.08	0.91±.05	1.05±.05
Th ($\mu g \cdot g^{-1}$)	2.0±0.1	7.0±0.1	1.5±0.1	1.9±0.1
U ($\mu g \cdot g^{-1}$)	1.2±0.09	4.0±0.1	2.4±0.1	3.8±0.1
Rb ($\mu g \cdot g^{-1}$)	29±2	64±6	28±4	24±2
Wet ρ ($g \cdot cm^{-3}$)	1.83	1.01	0.79	2.34
Layer thickness (cm)	3.0±0.5	2.0±0.25	3.0±0.5	2.75±0.25
Lower peat				
In situ Δ	3.48	1.77	5.82	3.28
Δ_{sat}	3.67	1.90	6.23	3.43
K (%)	0.27±0.01	0.89±0.05	0.30±0.02	0.66±0.03
Th ($\mu g \cdot g^{-1}$)	[2.0]	[2.0]	[2.0]	[2.0]
U ($\mu g \cdot g^{-1}$)	14.2±0.2	21.7±0.2	20.9±0.2	10.3±0.2
Wet ρ ($g \cdot cm^{-3}$)	1.06	1.12	0.95	0.99

Table 4.1: continued...

	FHTS-2	**FHTS-3**	**KHTS-1**	**KHTS-2**
Upper peat				
In situ Δ	3.75	1.96	3.49	3.12
Δ_{sat}	3.90	2.03	3.73	3.12
K (%)	0.5±0.03	1.60±0.05	0.79±0.04	0.76±0.04
Th (μg·g^{-1})	[2.0]	[2.0]	[2.0]	[2.0]
U (μg·g^{-1})	7.6±0.2	7.6±0.2	9.8±0.2	8.0 *pm* 0.2
Wet ρ (g·cm^{-3})	1.05	1.18	1.04	1.12
Layer thickness (cm)	90±1	6.0±0.5	50±1	3.5±0.5
Bulk sand				
In situ Δ	0.73	0.75	0.65	0.76
Δ_{sat}	0.85	0.77	0.65	0.76
K (%)	.92±.05	1.00±0.05	1.11±0.05	1.24±0.05
Th (μg·g^{-1})	1.2±0.1	1.6±0.1	1.3±0.1	1.4±0.1
U (μg·g^{-1})	2.1±0.1	3.3±0.1	[3.7±0.1]	3.7 *pm* 0.1
Rb (μg·g^{-1})	21±3	24±2	16±2	22±3
Wet ρ (g·cm^{-3})	0.88	1.82	1.93	1.49
Layer thickness (cm)	1.5±0.25	2.5±0.25	2.5±0.25	3.0±0.5
Lower peat				
In situ Δ	3.56	2.83	3.33	3.02
Δ_{sat}	3.62	2.96	3.39	3.07
K (%)	0.51±0.03	0.73±0.04	0.79±0.04	0.79±0.04
Th (μg·g^{-1})	[2.0]	[2.0]	[2.0]	[2.0]
U (μg·g^{-1})	8.5±0.2	9.5±0.2	8.8±0.2	19.3±0.2
Wet ρ (g·cm^{-3})	1.12	1.08	1.12	1.14

Table 4.2: Beta, gamma and cosmic ray contributions to the dose rate. An assumed internal α dose rate of 0.08 Gy/ka has been included in the total dose rate.

	ZCTS	**NRTS**	**NITS**	**FHTS-1**
Gamma (Gy/ka)				
Upper mud	0.075±0.004	0.096±0.008	0.015±0.002	0.011±0.001
Sand	0.064±0.004	0.071±0.008	0.024±0.004	0.108±0.005
Lower mud	0.021±0.003	0.064±0.005	0.021±0.003	0.028±.003
Beta (Gy/ka)				
External	0.70±0.03	1.19±0.04	0.69±0.03	1.06±0.03
Internal (K)	0.39±0.04	0.42±0.06	0.12±0.01	0.7±0.1
Internal (Rb)	0.11±0.01	0.26±0.05	0.14±0.02	0.15±0.02
Cosmic ray (Gy/ka)	0.27±0.02	0.24±0.02	0.25±0.02	0.24±0.02
Total (Gy/ka)	1.71±0.06	2.42±0.09	1.33±0.04	2.40±0.12
	FHTS-2	**FHTS-3**	**KHTS-1**	**KHTS-2**
Gamma (Gy/ka)				
Upper mud	0.020±0.003	0.024±0.003	0.014±0.002	0.0052±0.0007
Sand	0.010±0.004	0.018±0.002	0.05±0.02	0.041±0.004
Lower mud	0.029±0.003	0.038±0.004	0.032±0.003	0.036±0.003
Beta (Gy/ka)				
External	0.55±0.02	0.62±0.02	0.75±.08	.81±.02
Internal (K)	0.64±0.09	0.64±0.09	0.59±0.05	0.7±0.1
Internal (Rb)	0.15±0.02	0.15±0.02	0.09±0.01	0.12±0.02
Cosmic ray (Gy/ka)	0.23±0.02	0.29±0.02	0.25±0.02	0.29±0.02
Total (Gy/ka)	1.72±0.11	1.84±0.10	1.86±0.10	2.06±0.11

4.2 The β dose rate

The dose rate is the rate at which energy is deposited per unit mass of sample. If a disintegration occurs in which a β particle of energy ε is emitted and the specific β activity of the parent nucleus is c_β (*e.g.* expressed in units of Bq/kg), then the dose rate for a large sample is simply $\varepsilon \cdot c_\beta$. The quantity $\varepsilon \cdot c_\beta$ averaged over all β emissions from a particular isotope is commonly referred to as a dose conversion factor. The absorption coefficients for a wide range of dry soils are almost identical so that inhomogeneities in soil composition have little effect unless water is present. The reduction in the dose rate due to the presence of water is more than that from the effect of its mass alone since the β absorption coefficient for water is 25 % higher than that for a typical dry soil. If the water content is expressed as the weight of water divided by the dry weight, Δ, then the dose rate is,

$$\dot{D}_\beta = \frac{\sum_i \varepsilon_i c_{i,\beta} C_i}{1 + 1.25\Delta} \tag{4.1}$$

where the sum is over the respective quantities for each contributing radioisotope (K,U and Th) and C_i is the mass fraction of each isotope.

There are two contributions to the β dose rate to a grain, one from radioactive decay within the grain and a second from β particles originating outside the grain. These are discussed below.

4.2.1 The external β dose rate

The penetration depth of β particles of energy typical of radioactive decay is typically less than 1 mm in soil. All sand layers sampled in this study are over 1 cm thick so that the error introduced by neglecting the dose from the adjacent mud or peat is negligible. However, an additional factor must be included to take into account the attenuation of β radiation within the grains. The β attenuation factors used are those quoted by Mejdahl (1979).

A problem often encountered in young, organic-rich sediments is that there is an

Table 4.3: TSAC rates for the bulk sands and TSAC-derived thorium and uranium contents. Thorium and uranium contents from neutron activation analysis (NAA) and delayed neutron analysis (DNA) are included for comparison.

Sample	TSAC rate ($cm^{-2}{\cdot}ks^{-1}$)	Th (TSAC) ($\mu g{\cdot}g^{-1}$)	Th (NAA) ($\mu g{\cdot}g^{-1}$; ± 0.1)	U (TSAC) ($\mu g{\cdot}g^{-1}$)	U (DNA) ($\mu g{\cdot}g^{-1}$; ± 0.1)
NRTS	0.423±0.007	5.3±0.4	8.3	1.8±0.1	3.9
NITS	0.170±0.002	1.4±0.2	1.5	0.91±0.07	2.4
FHTS-1	0.233±0.005	2.0±0.3	1.85	1.2±0.1	3.8
FHTS-2	0.146±0.005	1.4±0.2	1.15	0.72±0.08	2.1
FHTS-3	0.221±0.004	1.3±0.2	1.55	1.36±0.07	3.3
KHTS-2	0.237±0.005	1.5±0.2	1.5	1.43±0.08	3.7

uptake of uranium from groundwater in the sample and adjacent layers. The thick-source α counting (TSAC) results (Table 4.3) indicate a lower amount of alpha activity from the uranium decay chain than would be present if there was secular equilibrium (for the dry bulk sand). This becomes evident upon comparison of the thorium and uranium contents calculated from TSAC and those obtained analytically from neutron activation analysis (NAA) and delayed neutron analysis (DNA) respectively. In most cases the calculated and measured thorium contents are approximately the same, whereas the uranium contents derived from TSAC are consistently smaller, by a factor of two or more, than the analytical values. If secular equilibrium prevailed the uranium contents derived from both methods should be the same.

The approach used to deal with this problem is identical to that used by Huntley and Clague (1996). Let U_{ex} denote the "uranium excess", that is the uranium that has been absorbed since the time of deposition. Although U_{ex} is not known, a reasonable estimate may be obtained by assuming that the uranium which is in secular equilibrium is 1/3 of the thorium content. This estimate is based on the observation that uranium typically accompanies thorium in a 1:3 ratio in most volcanic rocks of oceanic origin (Faure, 1991). Since thorium does not accompany the recently acquired uranium, one must only use the decay energy of the uranium chain up to ^{230}Th; for β

emission from the uranium decay chain this is 41% of the full chain energy (Aitken, 1985, p. 284). However, the time at which the U_{ex} was acquired is not known, thus an estimate based on the average of two extreme scenarios was used; either U_{ex} was acquired quickly, and contributes the full 41% of the pre-^{230}Th chain energy, or it was absorbed at a constant rate over time and contributes half of the pre-^{230}Th chain energy. One thus arrives at a value of 30±5% (5% covers both extremes at 2σ) for the fraction of the full chain energy to use in computing the U_{ex} contribution to the β dose rate.

4.2.2 The internal β dose rate

The internal β dose rate arises from potassium and, to a lesser extent, rubidium. There is some question as to what potassium content to use for the grains since the fraction of the K-feldspar grains contributing significantly to the 400 nm emission is not known. Spectral studies on feldspars of a wide range of compositions (see for example Prescott and Fox, 1993) indicate that there is strong emission in the 400-480 nm bandwidth for alkali feldspars of intermediate or higher potassium concentration.

The fraction of the grains in the K-feldspar fraction that are actually K-feldspar was determined by element mapping of 100–200 of the grains sprinkled onto a 1 cm graphite disk. This was achieved using a scanning electron microscope (SEM) fitted with an X-ray flourescence detector. Maps of K, Na, Si and Al content were made for each set of grains and the compositions of each grain compared qualitatively; for example, a grain with bright potassium, silicon and aluminum X-ray fluorescence was assumed to be orthoclase; if a grain also contained sodium it was designated alkali feldspar. A grain in which only silicon was bright was taken be quartz. The mineral fractions of orthoclase, alkali, albite, quartz and other unknown fractions were obtained by counting the number of grains that satisfied the X-ray fluorescence signature expected for each particular mineral. The SEM maps indicate that, in most samples, a large fraction of the grains are not pure K-feldspar, a significant fraction being either quartz or some type of aluminosilicate mineral, albite for example. The mineral fractions obtained from the SEM maps are given in Table 4.4.

Table 4.4: Mineral compositions of the separated K-feldspar grains. The term "orthoclase" is used to designate the high K-feldspar fraction determined from SEM.

	ZCTS	**NRTS**	**NITS**	**FHTS-1**
Size (μm)	170±50	100±40	230±80	180±50
K content of "K-feldspar" grains %	3.76±0.05	8.29±.05	0.76±0.05	—
Orthoclase fraction % (SEM)	33±4	42±4	35±4	28±4
Alkali feldspar fraction % (SEM)	22±4	9±3	17±4	5±3
Albite fraction % (SEM)	26±4	14±3	10±4	28±4
Other % (SEM)	18±4	25±4	38±4	38±4
K content of "orthoclase" %	8.5±0.8	18±2	2.2±0.3	—
Rb content of "orthoclase" (μg/g)	230±30	550±100	70±10	320±60
	FHTS-2	**FHTS-3**	**KHTS-1**	**KHTS-2**
Size (μm)	160±50	160±50	160±50	170±50
K content of "K-feldspar" grains %	—	4.70±0.05	5.69±0.05	3.94±0.05
Orthoclase fraction % (SEM)	22±5	22±4	37±4	20±4
Alkali feldspar fraction % (SEM)	38±5	24±4	15±4	15±4
Albite fraction % (SEM)	32±5	40±4	21±4	46±4
Other % (SEM)	8±5	14±4	26±4	19±4
K content of "orthoclase" %	—	14±2	13±1	14±2
Rb content of "orthoclase" (μg/g)	320±70	340±60	190±30	250±50

The potassium content of the actual K-feldspar grains in the "K-feldspar" fraction was first calculated by dividing the K content of the K-feldspar fraction obtained from atomic absorption analysis[1], by the orthoclase fraction computed from the SEM maps. The potassium contents obtained in this manner far exceed the maximum potassium content of 14% in pure orthoclase (both NRTS and KHTS-2 yielded potassium contents near 20%). This method is expected to overestimate the K contents because the K in the "alkali feldspars" is ignored. A better approximation can be obtained by adding 50% of the alkali feldspar fraction to the orthoclase fraction. Here one finds more reasonable values for the potassium contents; these are the values quoted in Table 4.4. In particular, note that the K contents of the K-feldspar grains for KHTS-1 and KHTS-2 are not significantly different, whereas in the original reckoning these values differ (15±2% and 20±4% respectively). The K-contents for KHTS-1 and KHTS-2 are expected to be nearly identical since they were collected from the same site and presumably are of similar geological provenance. These results indicate that a careful revision of the criteria for determining mineral fractions using SEM X-ray fluorescence maps is required.

The K-contents of the K-feldspar grains from FHTS-1 and FHTS-2 were taken as that of FHTS-3, namely 14±2%; for NRTS the potassium content was taken as 14%. The β dose rates are given in Table 4.4. The potassium content for NITS was anomalously low and should therefore be viewed with suspicion. The conversion factors used are those quoted in Nambi and Aitken (1986); no radon or thoron loss in the uranium and thorium decay series respectively was assumed.

It is assumed that rubidium accompanies potassium in the separated grains. The Rb content of the "actual" K-feldspar grains (*i.e.* that determined though SEM analysis and labeled "orthoclase" in Table 4.4) was determined under the assumption that the Rb/K ratio in the grains is the same as that of the bulk sand. The Rb content of the grains from FHTS-1 and FHTS-2 is assumed to be the same as that of FHTS-3. The analytical K-content of the separated grains from NITS is suspect and for this reason a typical Rb content of 300±50 μg/g is assumed.

[1]Analysis by Chemex Laboratories Ltd., North Vancouver, B.C.

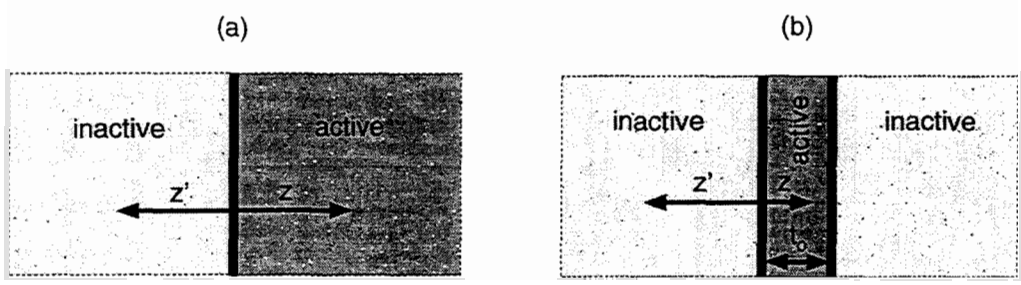

Figure 4.1: Geometry of the sediment layers. The sediment extends to infinity beyond the dotted lines; solid lines are the layer boundaries. Figure (a) shows an inactive (*i.e.* containing no radionuclides) semi-infinite layer bounded by a semi-infinite active layer; (b) shows an active layer of thickness t_o bounded by a semi-infinite layer on each side.

4.3 The gamma dose rate

The γ dose rate is computed in the same manner as the β dose rate, except that the absorption coefficient for water is 14% larger than that of a typical dry soil. The equation used previously for the β dose rate now reads for the γ dose rate,

$$\dot{D}_\gamma = \frac{\sum_i \varepsilon_i c_{i,\gamma} C_i}{1 + 1.14\Delta} \tag{4.2}$$

where the sum is over the respective quantities for each contributing radioisotope (potassium, uranium, thorium and their decay products), C_i is the concentration by weight of each isotope and Δ is the water content expressed as the ratio of the water mass to the dry mass. The above equation is valid for a sample that is homogeneous over a distance greater than 30 cm, which is the typical range of a γ ray in sediment.

For samples which consist of layers of different composition and water content, the computation of the γ dose rate is more complicated. Consider for example a soil section of semi-infinite extent. If the soil section is bounded by an inert soil (*i.e.* containing no radionuclides), then the dose rate at the interface is exactly 1/2 of that deep within the soil far from the boundary; see Figure 4.1 (a) . If the "dose rate fraction", f(z), is defined as the ratio of the dose rate received at depth z to that in a sample of infinite extent, then it is expected that f(0)=1/2 while $\lim_{z\to\infty}$ f(z)=1. The

fraction, f(z), has been calculated for a soil of typical composition by L. Løvberg of the Risø National Laboratory and the tabulated results may be found in Table H.1 of Aitken (1985).

Now consider the dose rate fraction, g(z'), at a depth z' in the inert layer; from the principle of superposition[2],

$$g(z') = 1 - f(z') \tag{4.3}$$

Next consider the situation of Figure 4.1(b). The dose rate fraction at depth z in an active layer of thickness t_o bounded by inactive material may similarly be shown to be (Aitken, 1985, p.292),

$$f_{int}(t_o, z) = f(z) + f(t_o - z) - 1 = 1 - g(z) - g(t_o - z) \tag{4.4}$$

The dose rate fraction at a distance z' outside this same layer is,

$$f_t(t_o, z') = f(z' + t_o) - f(z') = g(z') - g(z' + t_o) \tag{4.5}$$

In cases where the wet density differs from the density of 2 g/cm^3 used in Løvberg's calculations, Løvberg claims that the dose rate fractions may be obtained by scaling z with the density (i.e.: $z \rightarrow z\rho$ / 2 g·cm^3).

Since all of the grains within a layer of thickness t are sampled for luminescence, the relevant dose rate fraction is actually the *average* for the grains within the sampled layer rather than that at a particular depth within the layer. To simplify the calculation of these averages, a three-parameter fit was made to the f(z) data of Table H.1 in Aitken (1985), using the sum of two decaying exponentials[3]. The three-parameter fits thus obtained agree with Løvberg's data to better than 1%. The following two average dose fractions were computed using the fitted curves:

1) The average dose rate fraction for grains in a layer of thickness t due to an adjacent external layer of semi-infinite extent; this quantity is denoted by $\tilde{g}(t_o)$. This

[2]See for example Appendix H of Aitken, (1985).

[3]To a first approximation the probability of a γ penetrating to a depth z drops off exponentially, whence the choice of fitting Løvberg's data to a sum of decaying exponentials.

is the average of g(z) from z=0 to t_o and is shown in Table 4.5 for thicknesses t between 0 and 10 cm.

2) The average dose rate fraction for grains within a layer of thickness t_o due to the layer itself, as computed from the average of $f_{int}(t_o,z)$ from z=0 to t_o. This quantity is denoted as $\tilde{f}_{int}(t_o)$ and is shown in Table 4.6.

The average dose rate fraction in a layer of thickness t due to an adjacent layer of thickness t_o may be computed from the average of f_{ext} from z=0 to t. However, it is straightforward to show that this quantity, which will be denoted by $\tilde{h}(t_o,t)$, can be expressed directly in terms of the previously calculated $\tilde{g}(z)$ as,

$$\tilde{h}(t_o,t) = \tilde{g}(t) - \frac{t_o \cdot \tilde{g}(t_o+t) - (t_o+t)\cdot \tilde{g}(t_o)}{t} \tag{4.6}$$

The above quantity is useful in situations where a layer of sediment has been excluded from the sample and the dose in the sampled layer due to the excluded layer is desired. This was only required for the NRTS sample in which the lowest centimetre of the sand was excluded from the dated sediment section. The three quantities $\tilde{g}(t_o)$, $\tilde{f}_{int}(t_o)$ and $\tilde{h}(t_o,t)$ are the only geometric factors required to calculate the γ dose rate from any sediment section in which the stratigraphy consists of well defined horizontal layers in which the water content and radioisotope concentrations are uniform for each layer.

The calculated gamma dose rates

There are three significant contributions to the gamma dose rate in the samples: the gamma dose rate from the upper mud or peat; the dose rate from the lower peat; and the dose rate from the sand layer itself. In the case of the NRTS sample the dose rate from the discarded sand layer was also computed (despite its small overall contribution); the fractional dose for this contribution was computed using the expression for $\tilde{h}(t_o,t)$ given above and the data in Tables 4.5 and 4.6 (here t_o is the thickness of the sampled layer and t the thickness of the discarded layer). It was assumed that Løvberg's suggested scaling for wet densities other than 2 g·cm^{-3} for use with his f(t) data is applicable to the calculation of $\tilde{g}(t_o)$, $\tilde{f}_{int}(t_o)$ and $\tilde{h}(t_o,t)$. In

Table 4.5: Average dose rate fraction for grains within a layer of thickness t_o due to an adjacent semi-infinite layer, denoted by $\tilde{g}(t_o)$. t_o is appropriate for soil of wet density 2 g/cm^3. "Average" is weighted over potassium, thorium and uranium dose rate fractions assuming 20% potassium, 50% thorium and 30% uranium contents; *i.e.* as in Table H.1 of Aitken (1985).

t_o (cm)	K	Th	U	Avg.	t_o (cm)	K	Th	U	Avg.
0.5	0.474	0.472	0.470	0.472	5.5	0.324	0.318	0.311	0.317
1	0.452	0.448	0.445	0.448	6	0.314	0.308	0.301	0.307
1.5	0.432	0.427	0.423	0.427	6.5	0.306	0.299	0.292	0.298
2	0.414	0.409	0.404	0.408	7	0.297	0.290	0.283	0.289
2.5	0.397	0.392	0.387	0.392	7.5	0.289	0.282	0.275	0.281
3	0.383	0.377	0.371	0.376	8	0.281	0.274	0.267	0.273
3.5	0.369	0.363	0.357	0.363	8.5	0.274	0.267	0.259	0.266
4	0.356	0.351	0.344	0.350	9	0.267	0.260	0.252	0.259
4.5	0.345	0.339	0.332	0.338	9.5	0.260	0.253	0.245	0.252
5	0.334	0.328	0.321	0.327	10	0.254	0.247	0.239	0.246

Table 4.6: Average dose rate fraction for grains within a layer of thickness t_o due to the layer itself, denoted by $\tilde{f}_{int}(t_o)$. Weighted average and thicknesses are as in Table 4.5.

t_o (cm)	K	Th	U	Average	t_o (cm)	K	Th	U	Average
0.5	0.052	0.056	0.060	0.056	5.5	0.352	0.365	0.378	0.366
1	0.097	0.103	0.110	0.104	6	0.371	0.384	0.398	0.386
1.5	0.137	0.145	0.154	0.146	6.5	0.389	0.402	0.417	0.404
2	0.173	0.182	0.192	0.183	7	0.406	0.420	0.434	0.421
2.5	0.205	0.216	0.226	0.217	7.5	0.422	0.436	0.451	0.438
3	0.235	0.246	0.257	0.247	8	0.437	0.452	0.466	0.453
3.5	0.262	0.274	0.286	0.275	8.5	0.452	0.466	0.481	0.468
4	0.287	0.299	0.311	0.300	9	0.466	0.480	0.496	0.482
4.5	0.310	0.322	0.335	0.324	9.5	0.479	0.494	0.509	0.496
5	0.332	0.344	0.358	0.346	10	0.492	0.508	0.522	0.509

all cases the density used in computing the scaled thickness of the layers is that of the section for which the dose rate contribution was calculated. The dose rate fraction from the upper mud or peat layer was obtained using Table 4.5 to calculate the fraction $\tilde{h}(t_o, t)$[4] and multiplying this by the burial rate correction factor, explained later in Section 4.7. The dose rate fraction for the sand layer self dose was obtained from Table 4.6, and the fraction for the contribution from the lower peat was obtained from Table 4.5. The geometric factors involved in the calculation of the gamma dose rate and the computed gamma dose rates themselves are given in Table 4.7.

The contributions from uranium recently acquired, U_{ex}, and that in secular equilibrium, U_{eq}, were treated separately, as was done for the β dose rate. Gamma emissions from the pre-^{230}Th part of the uranium decay chain contribute only 2.1% to the full γ decay chain energy. Since the rate at which U_{ex} was acquired is not known, I proceeded as before for the β dose rate. U_{ex}'s contribution to the full chain energy was estimated by taking the average of that for early absorption into the sediments (2.1%) and that for a constant acquisition rate (1%); this gives a value of 1.5±0.3 % for the fraction of the full chain uranium γ decay energy to be used for U_{ex}. The U_{ex} does not therefore contribute significantly to the the dose rate.

[4]An appropriate scaled thickness for the layer was calculated.

Table 4.7: Computation of the gamma dose rate. The burial dose rate correction is described in Section 4.7. The scaled thickness or depth is the thickness multiplied by ratio of the wet density of the sediment to 2 g/cm^3. The dose rate fraction in the case of the upper peat and the discarded sand refers to the quantity $\tilde{h}(t_o, t)$, computed with t as the scaled thickness of the sand layer and t_o as the scaled depth and the discarded layer thickness, respectively. In the case of the sand layer, the dose rate fraction is the quantity $\tilde{f}_{int}(t_o)$ with t_o as the scaled thickness of the sand layer. For the lower peat the dose rate fraction is the quantity $\tilde{g}(t_o)$ with t as the scaled thickness of the sand layer.

	ZCTS	**NRTS**	**NITS**	**FHTS-1**
Upper mud or peat	mud	mud	peat	peat
Wet ρ (g·cm^{-3})	1.78	1.55	1.04	1.15
Scaled thickness (cm)	19.6±0.9	46.5±0.8	26.0±0.5	42.0±0.7
Burial rate correction	0.72±0.01	0.84±0.01	0.71±0.01	0.83±0.01
Dose rate fraction	0.352±.007	0.349±0.025	0.336±0.025	0.209±0.01
Dose rate (Gy/ka)	0.075±0.004	0.096±0.008	0.015±0.002	0.011±0.001
Sand				
Wet ρ (g·cm^{-3})	1.83	1.01	0.794	2.34
Scaled thickness (cm)	2.75±0.2	1.0±0.1	1.2±0.1	3.2±0.3
Dose rate fraction	0.217±0.015	0.104±0.02	0.104±0.02	0.247±0.01
Dose rate (Gy/ka)	0.064±0.004	0.071±0.008	0.024±0.004	0.11±0.005
Lower Peat				
Wet ρ (g·cm^{-3})	1.06	1.12	0.950	0.990
Dose rate fraction	0.38±0.02	0.45±0.01	0.44±0.01	0.37±0.02
Dose rate (Gy/ka)	0.021±0.006	0.064±0.005	0.016±0.002	0.028±0.003
Discarded sand				
Scaled thickness (cm)	1.4±.7	—	—	—
Dose rate fraction	0.053±0.01	—	—	—
Dose rate (Gy/ka)	0.0034±0.0006	—	—	—
Total γ dose rate (Gy/ka)	*0.163±0.006*	*0.23±0.01*	*0.055±0.005*	*0.146±0.006*

Table 4.7: Continued...

	FHTS-2	FHTS-3	KHTS-1	KHTS-2
Upper mud or peat	mud	mud	peat	peat
Wet ρ (g·cm^{-3})	1.05	1.82	1.04	1.12
Scaled thickness (cm)	47.3±0.7	3.5±0.3	26.0±0.5	2.0±0.3
Burial rate correction	0.85±0.01	0.57±0.01	0.76±0.01	0.55±0.01
Dose rate fraction	0.39±0.03	0.18±0.02	0.24±0.01	0.11±0.01
Dose rate (Gy/ka)	0.020±0.003	0.024±0.003	0.014±0.0015	0.0052±0.0007
Sand				
Wet ρ (g·cm^{-3})	.880	1.18	1.93	1.49
Scaled thickness (cm)	0.7±0.1	1.5±0.15	2.4±0.5	2.2±0.4
Dose rate fraction	0.056±0.02	0.15±0.02	0.22±0.015	0.18±0.02
Dose rate (Gy/ka)	0.010±0.003	0.018±0.002	0.05±0.02	0.041±0.004
Lower Peat				
Wet ρ (g·cm^{-3})	1.12	1.08	1.12	1.4
Dose rate fraction	0.46±0.01	0.43±0.01	0.39±0.01	0.40±0.01
Dose rate (Gy/ka)	0.029±0.003	0.038±0.0035	0.032±0.003	0.036±0.003
Total γ dose rate (Gy/ka)	*0.058±0.005*	*0.079±0.005*	*0.09±0.02*	*0.083±0.005*

4.4 Thick source alpha counting

The rate at which α track length is produced in a thick[5] sample may be expressed in terms of the count rate obtained from a *thick-source* α counting experiment. Thick-source alpha counting (TSAC) is a simple, yet precise, method of determining the rate of production of α track length in a sample. It can also provide a value for the uranium-to-thorium ratio by counting the pairs produced by the decay of polonium-216 in the thorium decay chain. In TSAC a thick layer of fine powdered sample is spread over a zinc sulphide screen and the scintillations produced by the α particles impinging on the zinc sulphide screen are counted using a photomultiplier tube. Since the range of α particles in air is short and the zinc sulphide is relatively insensitive

[5] "thick" refers to a layer thicker than the ranges of all the α particles.

to β particles and γ rays, only α emissions from the sample are counted. The surface emission rate of α particles per unit area of scintillator obtained during TSAC is given by (Huntley *et al.*, 1988),

$$\lambda = \frac{1}{4}\sum_i A_i R_i \rho \tag{4.7}$$

where R_i and A_i are the the ranges and activities[6] of the various α's produced in the uranium and thorium decay chains and ρ is the sample density. In practice only a fraction of the detected PMT counts are counted. It is conventional to set the electronic threshold so that 82% and 85% of the pulses from the uranium and thorium decay chains respectively are counted, and allowances are made for this in the calculations. The constant 1/4 in Equation 4.7 is a geometric one, being the fraction of α particles emitted in a thickness $R\rho$ that reach the zinc-sulphide screen (Aitken, 1985).

TSAC rates for six bulk samples are given in Table 4.3[7]; also listed are the thorium and uranium contents derived from the TSAC rates[8]. Comparison of thorium and uranium contents obtained from TSAC with those obtained by NAA and DNA analysis, respectively, indicates that, although the thorium contents are generally in agreement, the uranium contents derived from TSAC are considerably lower than those obtained from DNA analysis. As discussed earlier, disequilibrium is to be expected when uranium has been absorbed by the sediments since deposition. TSAC was performed solely to provide this diagnostic. The "U (TSAC)" values in Table 4.3 represent the uranium content that would give the same TSAC rate as if secular equilibrium prevailed.

[6]The activity is given in terms of the number of emissions per unit time per unit mass.
[7]Bulk sand was dried, milled to a fine powder and re-dried for TSAC.
[8]TSAC was performed by D.J. Huntley

4.5 The α dose rate

An internal alpha count rate for the grains cannot be determined from the TSAC results because TSAC was performed on the *bulk* sand, not on the separated "K-feldspar" grains. I therefore only provide an estimate of the internal α count rate based on the TSAC rates of a "K-feldspar" grain separate from Buctouche Spit, New Brunswick (Ollerhead *et al.*, 1994). The average total TSAC rate is 0.25±0.02 $cm^{-2} \cdot ks^{-1}$; assuming a b-value of 1.03 $pGy \cdot m^2$ (Huntley *et al.*, 1988) yields an alpha dose rate of 0.081±0.006 Gy/ka. Corrections for geometric effects due to the size of the grains were not made since these are negligible. Grain size effects are discussed in the Appendix.

4.6 Cosmic-ray dose rate

The sea level flux of cosmic rays consists primarily of muons, electrons and γ photons which arise from interactions of protons of cosmic origin in the upper atmosphere. The cosmic rays are traditionally grouped into a "soft" component consisting mostly of electrons and photons that are easily attenuated and a "hard" component that penetrates deeply into soil or rock and is mostly muons[9]. The cosmic ray flux is dependent on elevation (the flux is roughly 10 times larger at an altitude of 10 km than at sea level), and to a lesser extent on latitude (there is a 9% variation of the hard component between the geomagnetic poles and the equator, Prescott and Stephan, 1982).

The cosmic ray dose rate was calculated using the sea-level dose-rate vs. depth data published by Prescott and Hutton (1988) and the geomagnetic latitude variation data of Prescott and Stephan (1982). The geomagnetic latitude of Prescott and Hutton's measurement site, near Mount Gambier in the south-east of South Australia, is $\sim$-47° whereas it is roughly +53° on Vancouver Island. The difference in the hard cosmic ray flux is less than 0.5% between the two sites. The latitude dependence of

[9]The hard cosmic ray component is usually defined as the component which traverses 100 g/cm^2 of lead.

the soft cosmic ray component is assumed to be similarly negligible. Calculated dose rates are given in Table 4.2.

4.7 Temporal effects

Because the mud or peat overlying the sampled layer has accumulated gradually with time, the cosmic ray dose rate decreased, and the γ dose rate from the overlying soil section increased, with time.

The γ dose rate in the sampled layer of thickness t due to an overlying layer of thickness t_o may be estimated by averaging $\tilde{h}(t_o, t)$ (see Section 4.3) for increasing active layer thicknesses. It is easily seen that this is equivalent to computing a time-averaged dose rate assuming a fixed deposition rate for the upper layer. The computed ratio between the dose expected for a constant burial rate and quick burial (refered to as the *burial rate correction*) is shown in Figure 4.2. For sampled layer thicknesses t_o greater than 10 cm, the 10 cm curve may be used without introducing any significant error in the burial rate correction. The effective average cosmic ray dose rate may similarly be obtained by averaging the data of Prescott and Hutton (1988) over the depth of the sampled section, again assuming a constant sedimentation rate for the upper soil (Figure 4.3). The data show that, for a soil of density $2g/cm^3$, the quick burial assumption leads to an overestimate of the cosmic ray dose of approximately 16% for a burial depth of 60 cm. The cosmic ray dose rates quoted in Table 4.2 were calculated under the assumption of a constant sedimentation rate (*i.e.* from the upper curve in Figure 4.3).

Although the assumption of a constant burial rate is admittedly crude, it is more reasonable, in the case of peats, than the assumption of quick burial. For the sand layers overlain by mud, the assumption of an approximately constant burial rate may not be appropriate since one can easily envisage scenarios in which this mud was deposited rapidly (*e.g.* on an abrupty subsided surface after an earthquake).

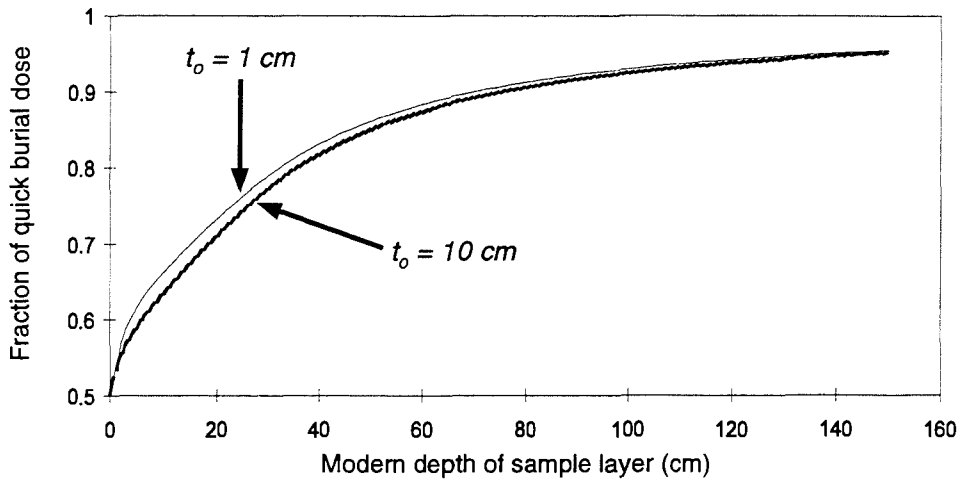

Figure 4.2: Ratio of [dose rate in a sample layer of thickness t_o due to an overlying layer being deposited at a constant sedimentation rate] to [dose rate expected for rapid burial of the layer] vs. current thickness of the overlying layer. The upper curve is for $t_o = 1$ cm, the lower curve is for $t_o = 10$ cm. For t_o greater than 10 cm, the lower curve provides a satisfactory estimate (better than 3%). Data are averaged over K, U and Th contributions as in Table 4.5 and are for soil of wet density $2g/cm^3$. Obtained from integration of curves used to produce data in Tables 4.5 and 4.6.

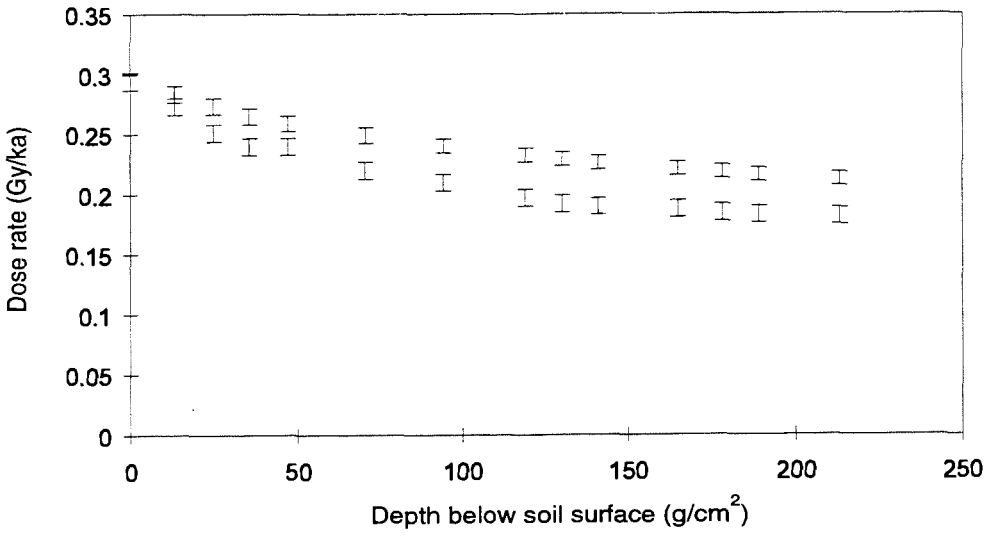

Figure 4.3: Average cosmic ray dose rate (upper points) for a constant sedimentation rate vs. soil depth assuming constant sedimentation. The lower points are Prescott and Hutton's (1988) data for the instantaneous cosmic ray dose rate as a function of soil depth.

Chapter 5

The Optical Ages

5.1 Experimental procedure

Approximately 50 aliquots, each containing 5–10 mg of grains, were prepared for each sample on 1.2-cm-diameter aluminum planchets as described in Section 2.3. Three experiments were undertaken: an evaluation of the equivalent dose using an additive dose method; an evaluation of the equivalent dose using a regeneration method; and a test for anomalous fading. Planchets were first subjected to a short (5 second) infrared illumination to normalize the luminescence from each planchet using the "short shine" method described in Section 1.3.1. Normalization values obtained from the "short-shine" luminescence are typically significantly different from the normalizations calculated from the mass of grains on each planchet. The short-shine produced a luminescence decay ranging from 5% to 16% of the natural, untreated grains (the equivalent dose was later corrected for this decay).

The paucity of K-feldspar available for dating meant that for some samples (NITS, for example) no more than 50 planchets could be prepared for measurement. A pilot experiment using 8 planchets was performed on each of the presumed oldest samples to determine a schedule of applied laboratory doses. Irradiations were performed using a ^{60}Co gamma source which provided a dose rate of 0.366 Gy/min (May 1996). Samples were bleached for 3 hours under a halogen lamp (automobile headlamp) using a long-pass filter (RG 710) to remove the shorter wavelength components (*i.e.* those below

Table 5.1: Equivalent doses and anomalous fading results for the tsunami sands. 'a.d.' refers to additive dose, 'reg.' is regeneration data. Both sets of values are from integration of the *initial* portion of the luminescence decay curve. Anomalous fading data are the ratio of the luminescence intensities of three sets of aliquots that had been given the quoted delay periods between irradiation and measurement (*i.e.* 130 days, 25 days and 4 days).

Sample	**D_{eq} a.d.** (Gy)	**D_{eq} reg.** (Gy)	**Anomalous fading** **25 days/4 days**	**130 days/4 days**
FHTS-1	2.4±0.3	2.0±0.2	0.99±0.03	0.91±0.02
FHTS-2	9.8±1.0	8.5±0.7	—	—
FHTS-3	1.4±0.3	1.0±0.1	—	—
KHTS-1	0.53±0.08	0.47±0.05	1.07±0.04	1.01±0.04
KHTS-2	0.27±0.06	0.24±0.05	—	—
	‡0.10 ±0.04	‡0.16±0.02		
NITS	3.2±0.6	2.3±0.4	0.96±0.04	0.94±0.05
NRTS	1.3±0.2	1.3±0.1	1.08±0.03	† 0.98±0.04
ZCTS	20±1	20±1	0.99±0.02	0.94±0.01

† Luminescence intensity ratio for 292 day rest period to 4 day rest period.
‡ Post measurement normalized.

~710 nm). The spectrum of this bleach source has not yet been measured. Samples were preheated at 120°C one to three days after bleaching and irradiation. All samples but NRTS and FHTS-2 were left for over 3 months (May 30 to September 10) before measurement to reduce any effect of anomalous fading. Sample NRTS was given a rest period of 2 months between preheat and measurement (July 9 to September 10). Only 10 days separated the times of preheat and measurement for FHTS-2.

Three groups of 5 aliquots were prepared; each group was given the same radiation dose, but with a different delay period between the time of irradiation and preheating. At the end of the delay periods all aliquots were simultaneously preheated and their luminescence measured on the following day. All irradiations were for 7.5 Gy and the delay period for each group of irradiated planchets was as follows: 280 days, 25 days and 4 days for NRTS; 95 days, 25 days and 4 days for all the other samples

(FHTS-1, KHTS-1 and ZCTS). The purpose of this experiment was to determine whether significant fading was present in our K-feldspar samples. After measurement all planchets were bleached, given a gamma radiation dose (~10 Gy), preheated, and their luminescence was measured. This second measurement was used to normalize the planchet intensities. The luminescence of 3 untreated and 2 bleached aliquots that had not been preheated were also measured for monitoring purposes.

Final luminescence measurements were performed using a diode current of ~0.2 A which gave an illumination power density of 25 mW/cm^2 at the sample. The intensities of the *natural+dose*[1] planchets were corrected for the decay incurred during normalization by adding to each planchet the average value of the decayed intensity of the natural, undosed planchets. Equivalent doses for the additive dose experiments were determined using a maximum-likelihood line-fitting routine to determine the intercept of the *natural+dose* and *thermal transfer correction*[2] lines. The equivalent dose was determined from the regeneration experiment by shifting the *natural+dose* line along the dose axis until it coincided with the *regeneration*[3] line; the dose shift required to do this is the equivalent dose. The regeneration and additive dose data for the tsunami sands are shown in Figures 5.2–5.14. The equivalent doses from the additive dose and regeneration experiments, as well as the results of the athermal fading experiment, are tabulated in Table 5.1.

5.2 Discussion

5.2.1 Anomalous fading

Anomalous fading results are summarized in Table 5.1. These clearly indicate that fading occured in some samples over the time the irradiated samples were allowed to rest. FHTS-1 had the largest fading, 9% over the 3 month rest period, whereas sample KHTS-1 and NRTS did not show any noticeable fading over this period. The data normalized with the natural (untreated aliquot) luminescence have very large

[1]Designates planchets that have been given a γ radiation dose followed by the preheat.
[2]Planchets that have been given a γ dose, bleached for three hours and preheated.
[3]Planchets that have been bleached, given a γ dose and preheated.

scatter as can be seen from the plots in Figure 5.1. The smallest scatter was found in sample ZCTS which is also the oldest and brightest of the samples.

Use of the post-measurement normalized values reduced the scatter for most samples. This can be accounted for as follows. If, at deposition, a sample contains some inadequately bleached grains, these will give more luminescence than they would otherwise. A planchet may contain a few such unbleached grains which contribute more than they normally would to the luminescence. If one were to use the natural luminescence intensity of this planchet for normalization, then the normalization value would be overestimated. The bright natural luminescence in this case does not indicate an inherently high luminescence-producing sensitivity in the aliquot, but is a reflection of the old optical age of a few of the grains in the particular aliquot.

This is not a problem if a post-measurement normalization is used since the luminescence from each planchet is reset close to 0 by bleaching. Subsequent irradiation and measurement should therefore yield normalization values that accurately reflect the luminescence-producing sensitivity of each planchet. The effect of the post-normalization on our samples was dramatic; the standard deviation of the planchet intensities is typically less than 4% of the average intensity for the post-measurement normalized data while the scatter in the data normalized with the natural intensities often exceeds half the value of the mean intensity (see Figure 5.1).

5.2.2 Equivalent dose measurements

Plots of luminescence intensity versus applied dose for the additive dose measurements are shown in Figures 5.2 to Figure 5.14. The scatter in the luminescence intensities, especially for the younger samples, for planchets subjected to the same treatments (e.g.: KHTS-2 and FHTS-3) is large. As was suggested for the anomalous fading samples, this may be due to uneven solar resetting of the grains. This effect may be detected by looking for a correlation between the normalization values and the luminescence intensities obtained after measurement. For example, a planchet containing a few very old and bright grains would give a relatively high normalization value even though its intrinsic brightness may be similar to the average. Upon irradiation and

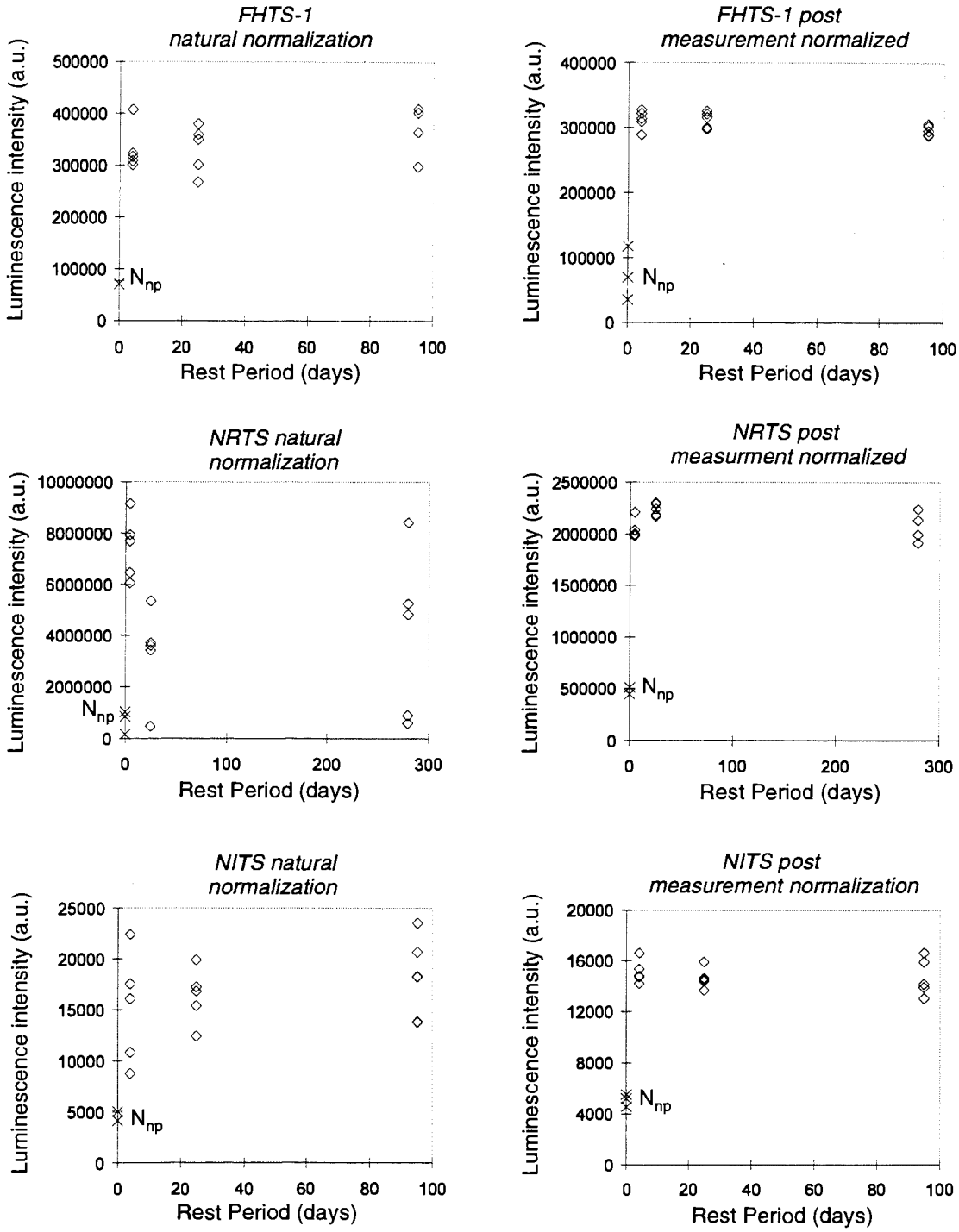

Figure 5.1: Luminescence intensities of planchets subjected to a 7.5 Gy γ irradiation and given a rest period (horizontal axis) between irradiation and measurement. Points labeled N_{np} are the natural unpreheated aliquot intensities.

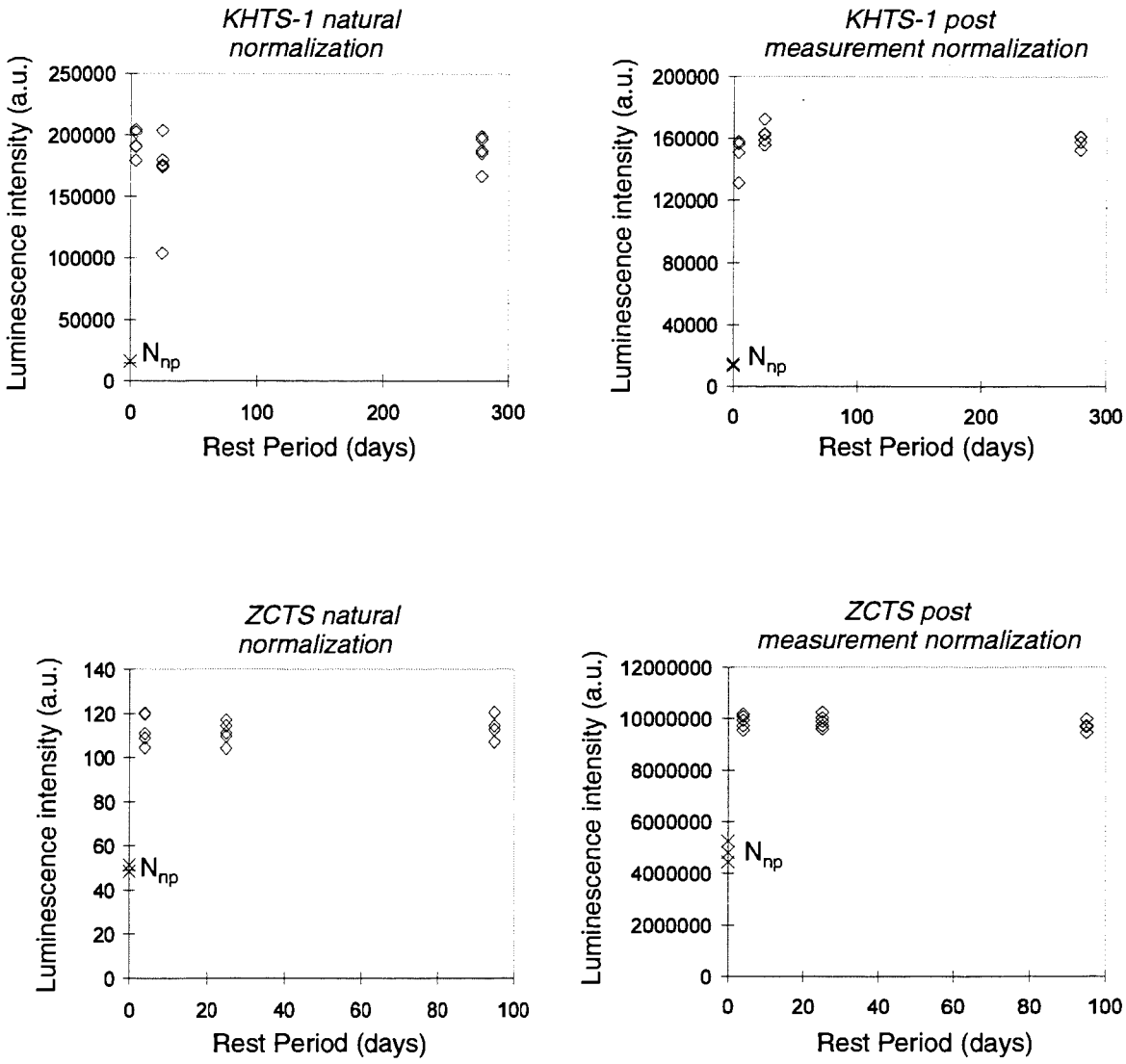

Figure 5.1: Continued... The ZCTS planchets received 26.3 Gy of laboratory γ radiation.

measurement such a planchet would give a luminescence signal comparable to the average, and thus its normalized intensity would be lower than the average (Huntley and Berger, 1995).

Illustration of this was attempted by using half-filled diamonds and squares in the luminescence versus dose plots. If the filled part of a diamond or square points "down", the normalization value for this planchet is lower than the average; if the top of the diamond or square is filled, the planchet has a higher-than-average normalization value. If solar resetting was incomplete, the planchets with relatively low normalized intensities (after irradiation) should have high normalization values (diamond or square with lower half filled), and vice-versa. However, since there were so few points (planchets) for each applied dose (usually 3) it is difficult to determine whether what is observed is due to the above effect or due to random scatter in the data. In some samples such as NRTS, FHTS-1 and possibly KHTS-2 this effect appears to be present.

Equivalent doses obtained using the regeneration method are consistently lower than those obtained using the additive dose method. There is also a noticeable dependence of the D_{eq}'s on the section of the luminescence decay curve that is integrated to determine the luminescence intensity. This was found for both regeneration and additive dose data. D_{eq}'s determined from the first part of the luminescence decay curve (*i.e.* immediately after the diodes are turned on) are lower than those obtained from the final part of the decay curve (*i.e.* 40 seconds later). This was observed for all the samples except KHTS-1 and NITS (see the inset plots in Figures 5.3 to 5.14).

This last observation can be explained by considering the different populations of traps that are emptied along the decay curve. Initially the excitation preferentially depopulates those traps with the largest photo-excitation probability. As these traps begin to empty, the fraction of the luminescence arising from traps with lower photo-excitation probability steadily increases. Thus at different times during the luminescence decay, different populations of trapped electrons are sampled. Since the most easily emptied traps are those that are most easily emptied in the environmental bleach, one might expect the optical age obtained from the early part of the luminescence decay curve to be younger than that found using later portions of the

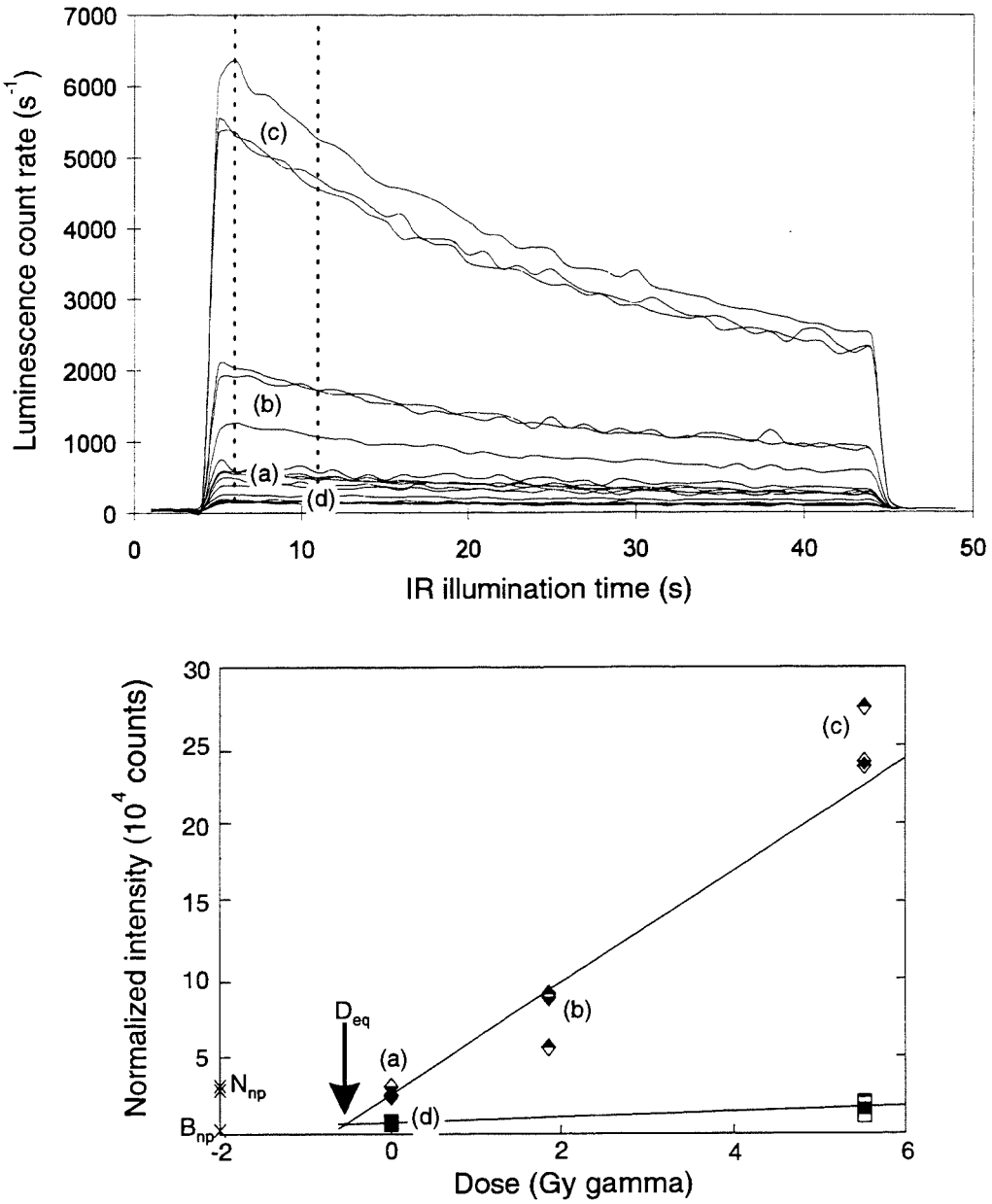

Figure 5.2: *Top:* Typical luminescence decay curve shown for sample KHTS-1; the IR diodes are turned on at 5 seconds and turned off at 45 seconds. The curves labelled (a), (b) and (c) are for the natural untreated aliquots, aliquots given 2.0 Gy γ irradiation and the aliquots that have received 5.6 Gy γ irradiation, respectively. Dotted lines indicate the section of the curve that has been integrated to obtain the additive dose plot (bottom). N_{np} and B_{np} are the natural and bleached, unpreheated planchets, respectively. Luminescence intensity was corrected for the decay incurred upon normalization as described in Section 5.1. Filling of the upper half or lower half of a symbol indicates a larger- or smaller-than-average normalization value for the aliquot, respectively.

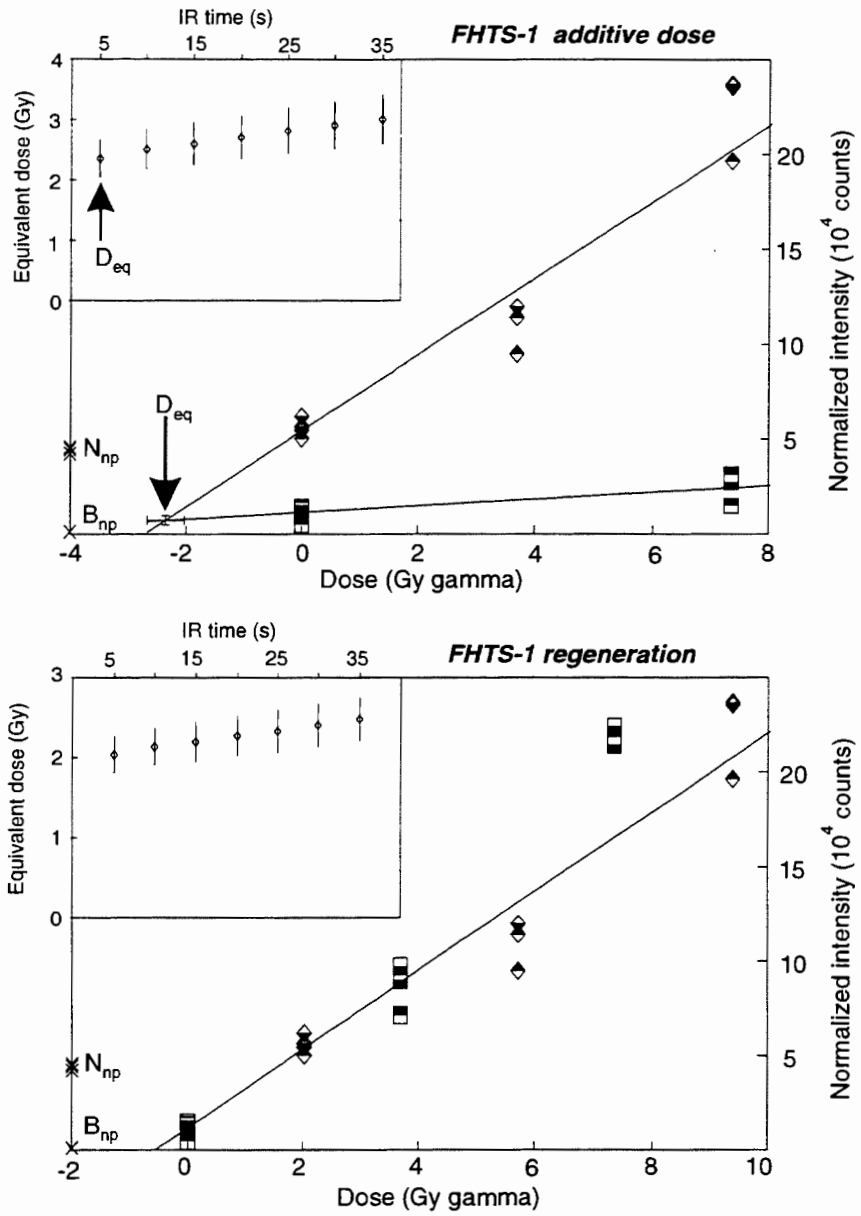

Figure 5.3: Additive dose (*top*) and regeneration (*bottom*) growth curves for FHTS-1. The main plots show the intensity integrated over the first 5 seconds of diode illumination. Insets show the variation of D_{eq} with time along the luminescence decay curve. Diamonds represent the dosed aliquots. Squares are the dose+bleached aliquots (*top*); and the bleached+dose aliquots (*bottom*). The dosed line (diamonds) in the regeneration plot has been shifted to lie on the bleached+dose line (squares), this shift is the equivalent dose at 5 s in the inset. N_{np} and B_{np} are the unpreheated natural and bleached sample intensities, respectively.

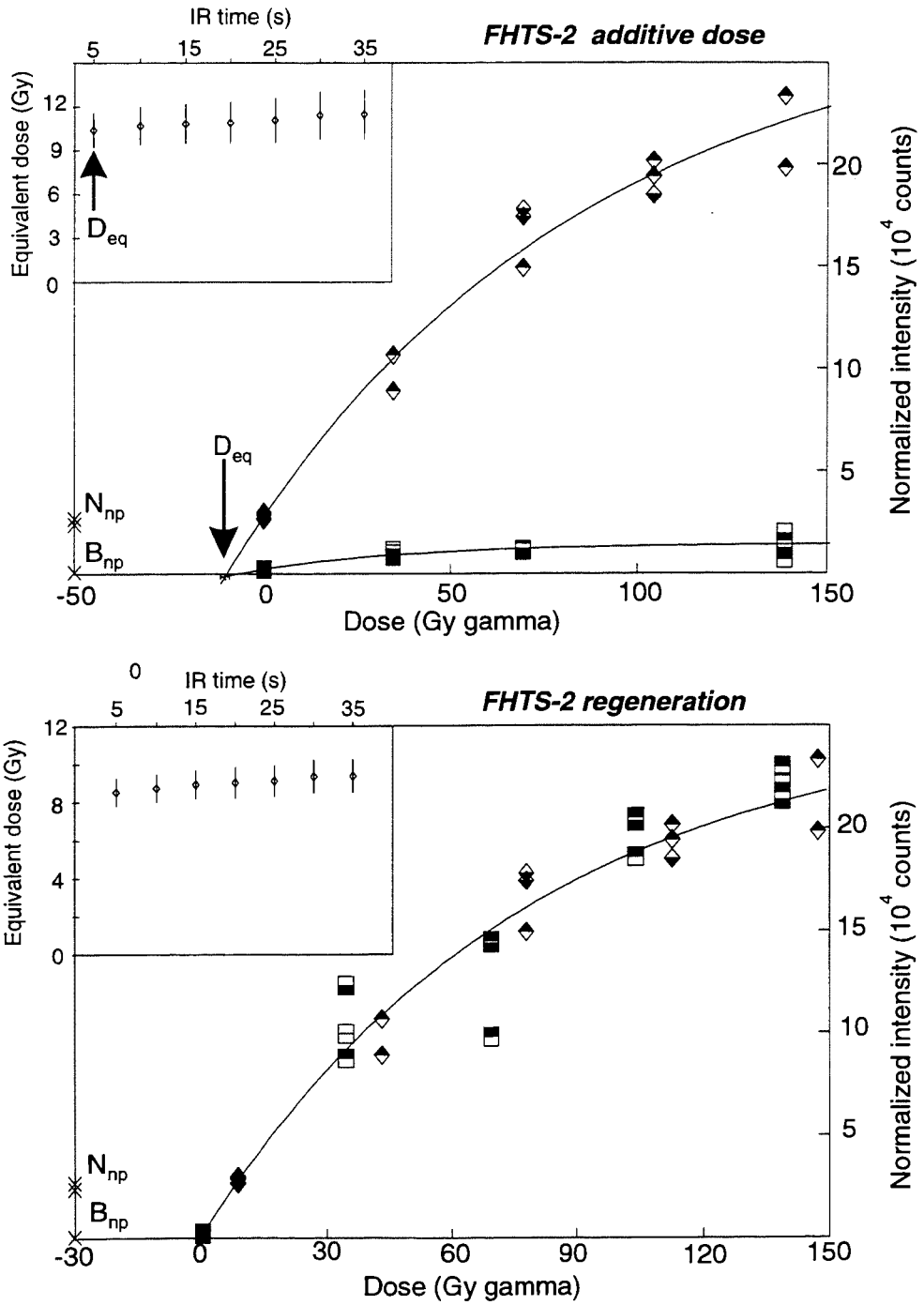

Figure 5.4: Additive dose (*top*) and regeneration (*bottom*) growth curves for FHTS-2. See Figure 5.3 for an explanation of the symbols used.

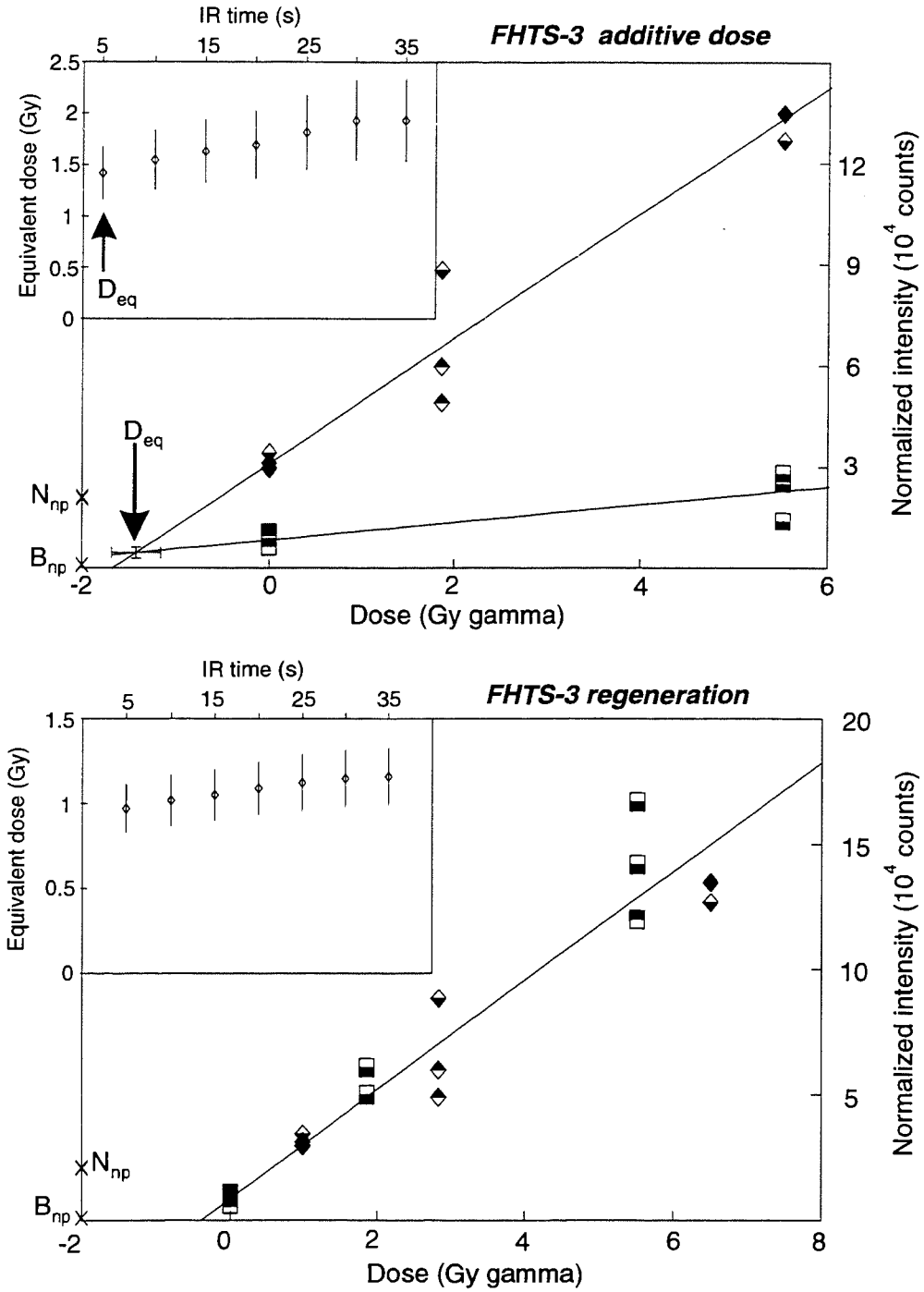

Figure 5.5: Additive dose (*top*) and regeneration (*bottom*) growth curves for FHTS-3. See Figure 5.3 for an explanation of the symbols used.

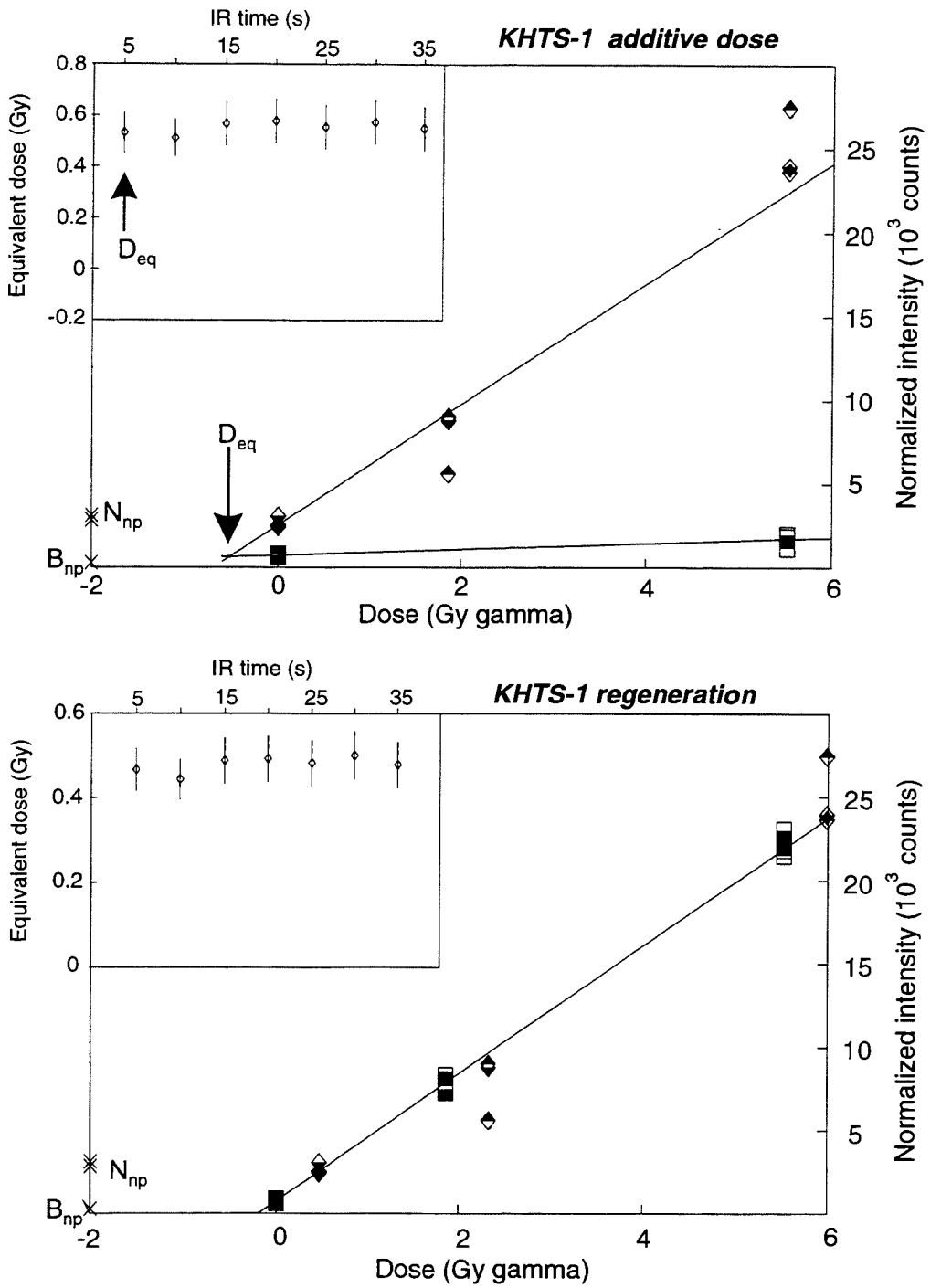

Figure 5.6: Additive dose (*top*) and regeneration (*bottom*) growth curves for KHTS-1. See Figure 5.3 for an explanation of the symbols used.

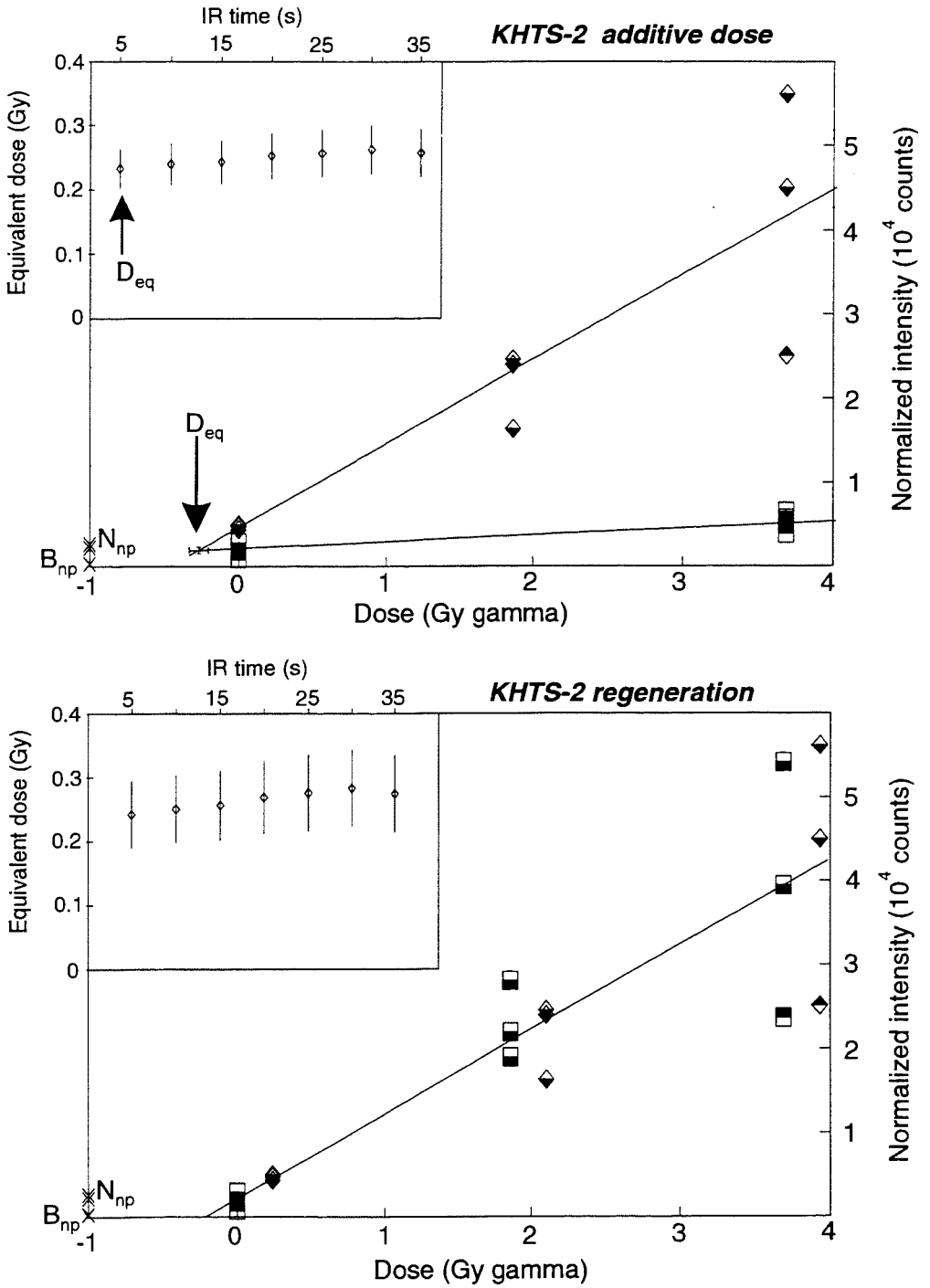

Figure 5.7: Additive dose *(top)* and regeneration *(bottom)* growth curves for KHTS-2. See Figure 5.3 for an explanation of the symbols used.

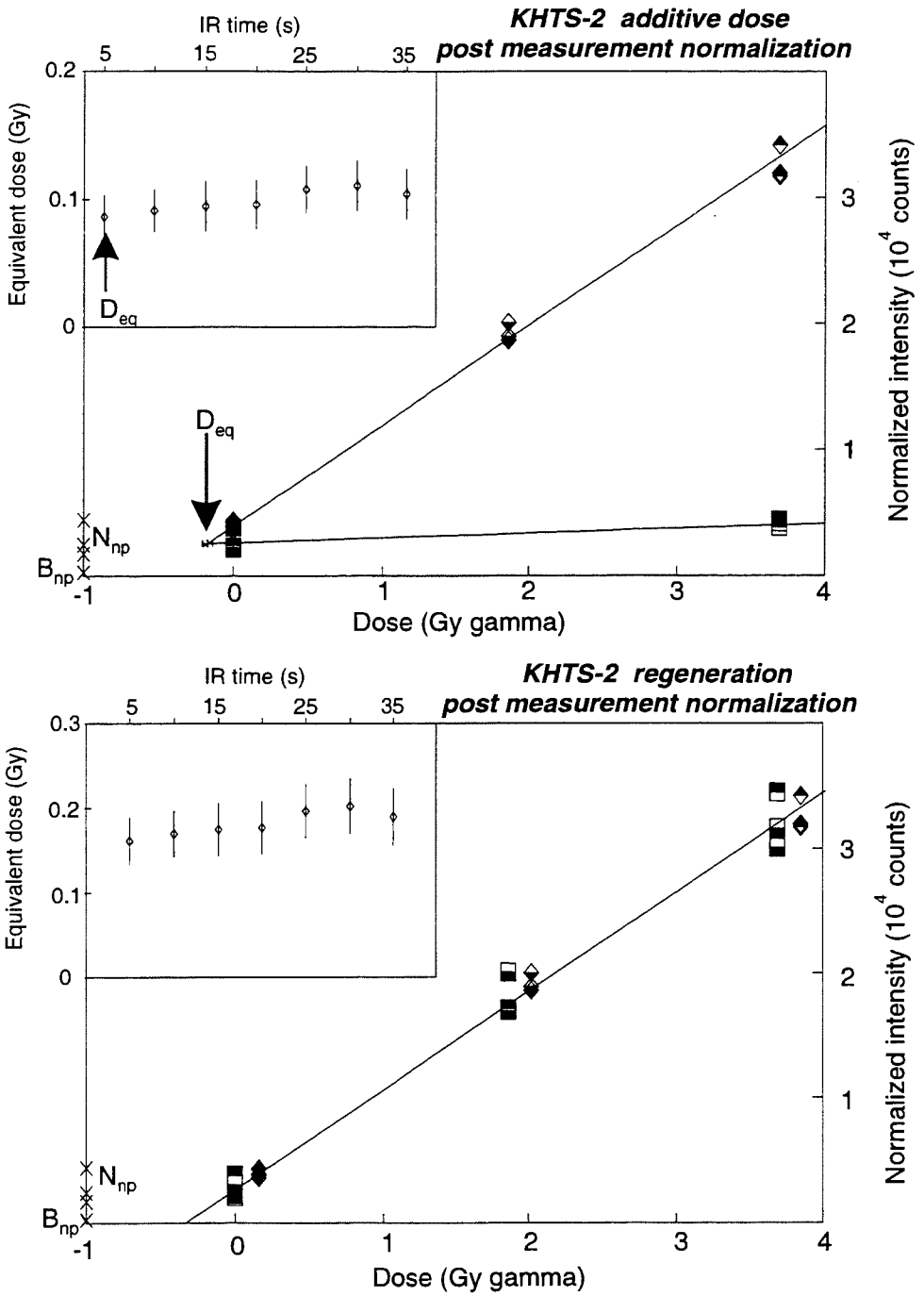

Figure 5.8: Additive dose (*top*) and regeneration (*bottom*) growth curves for KHTS-2 using the post-measurement normalization. See Figure 5.3 for an explanation of the symbols used.

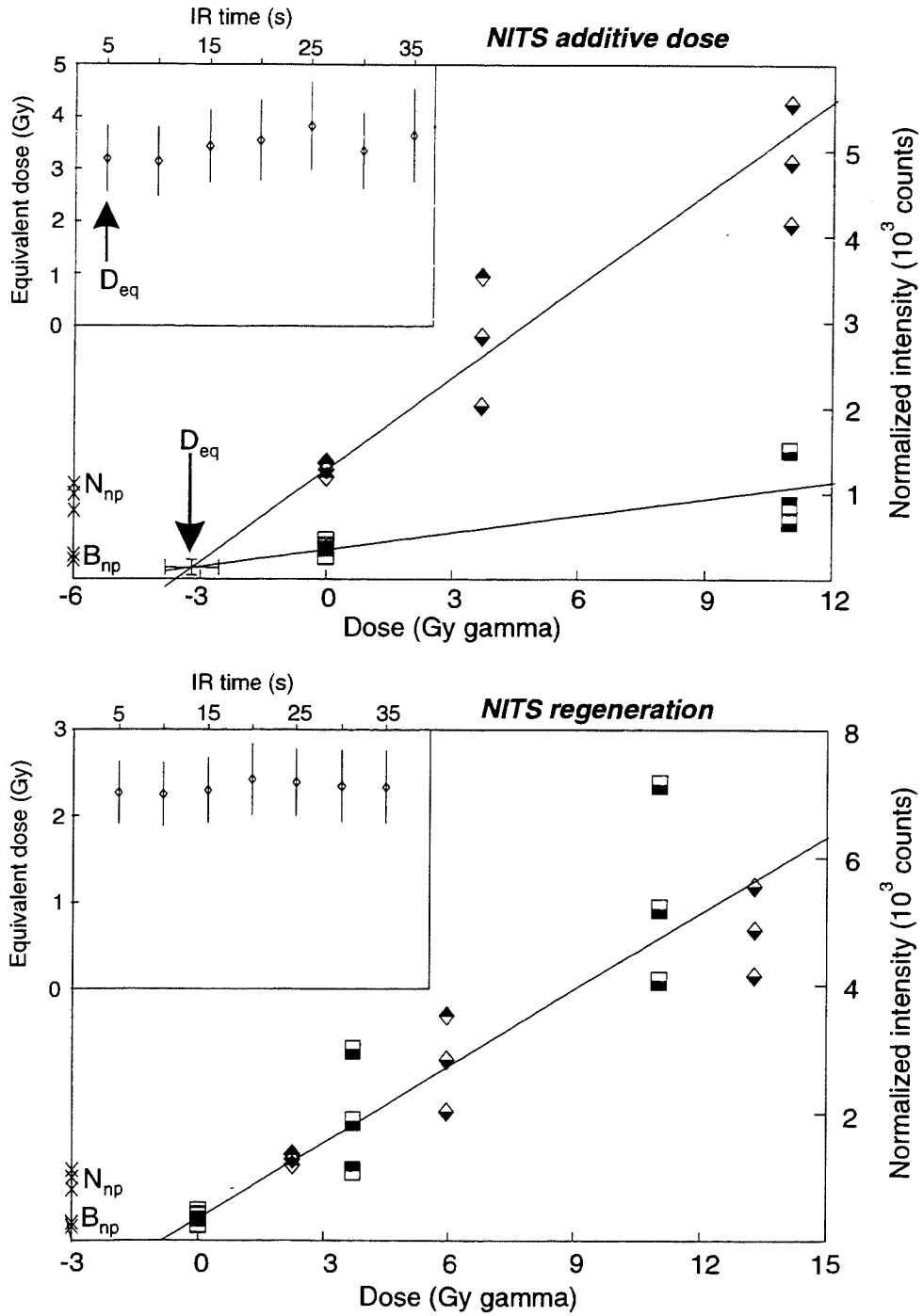

Figure 5.9: Additive dose (*top*) and regeneration (*bottom*) growth curves for NITS. See Figure 5.3 for an explanation of the symbols used.

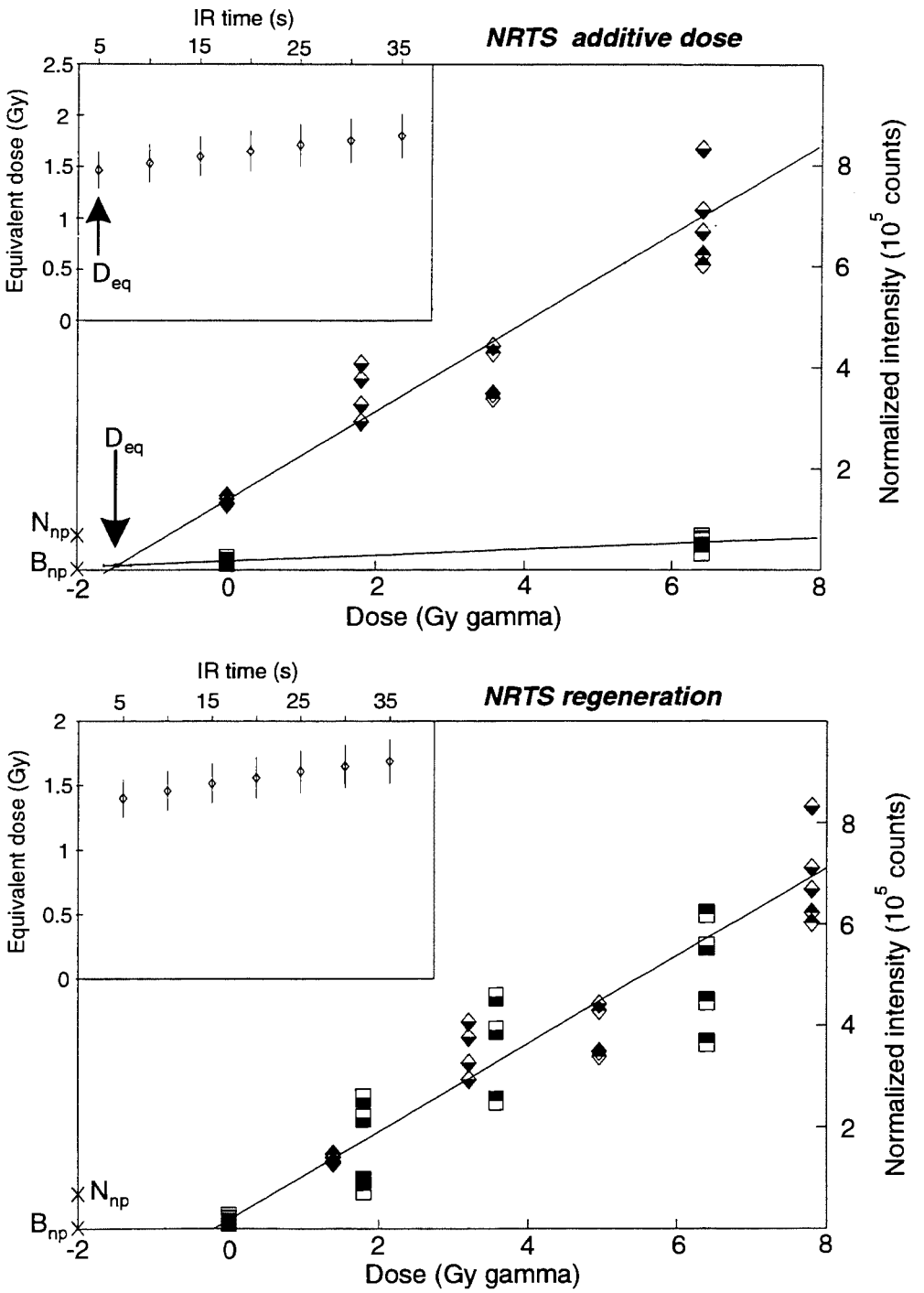

Figure 5.10: Additive dose (*top*) and regeneration (*bottom*) growth curves for NRTS. See Figure 5.3 for an explanation of the symbols used.

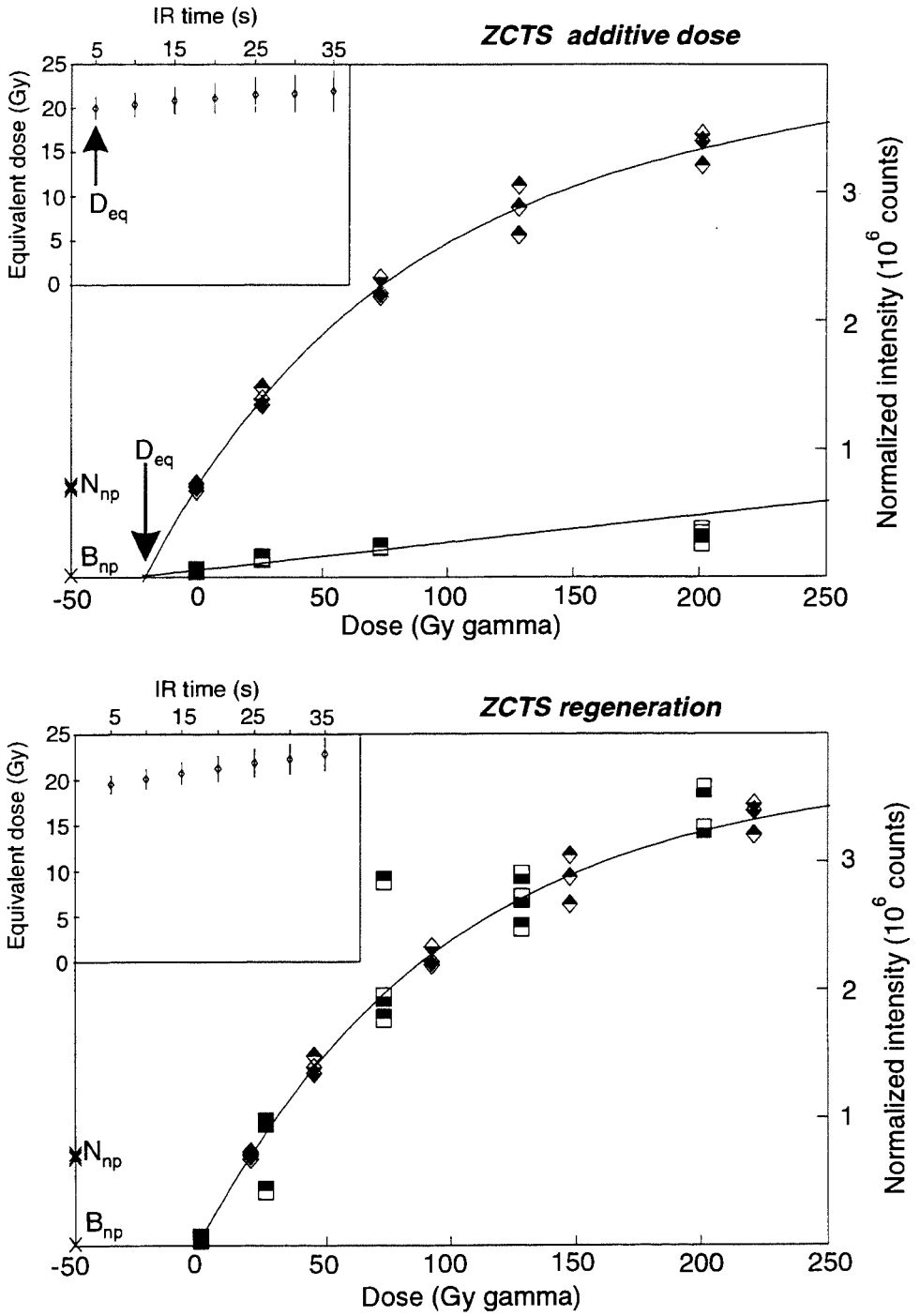

Figure 5.11: Additive dose (*top*) and regeneration (*bottom*) growth curves for ZCTS. See Figure 5.3 for an explanation of the symbols used.

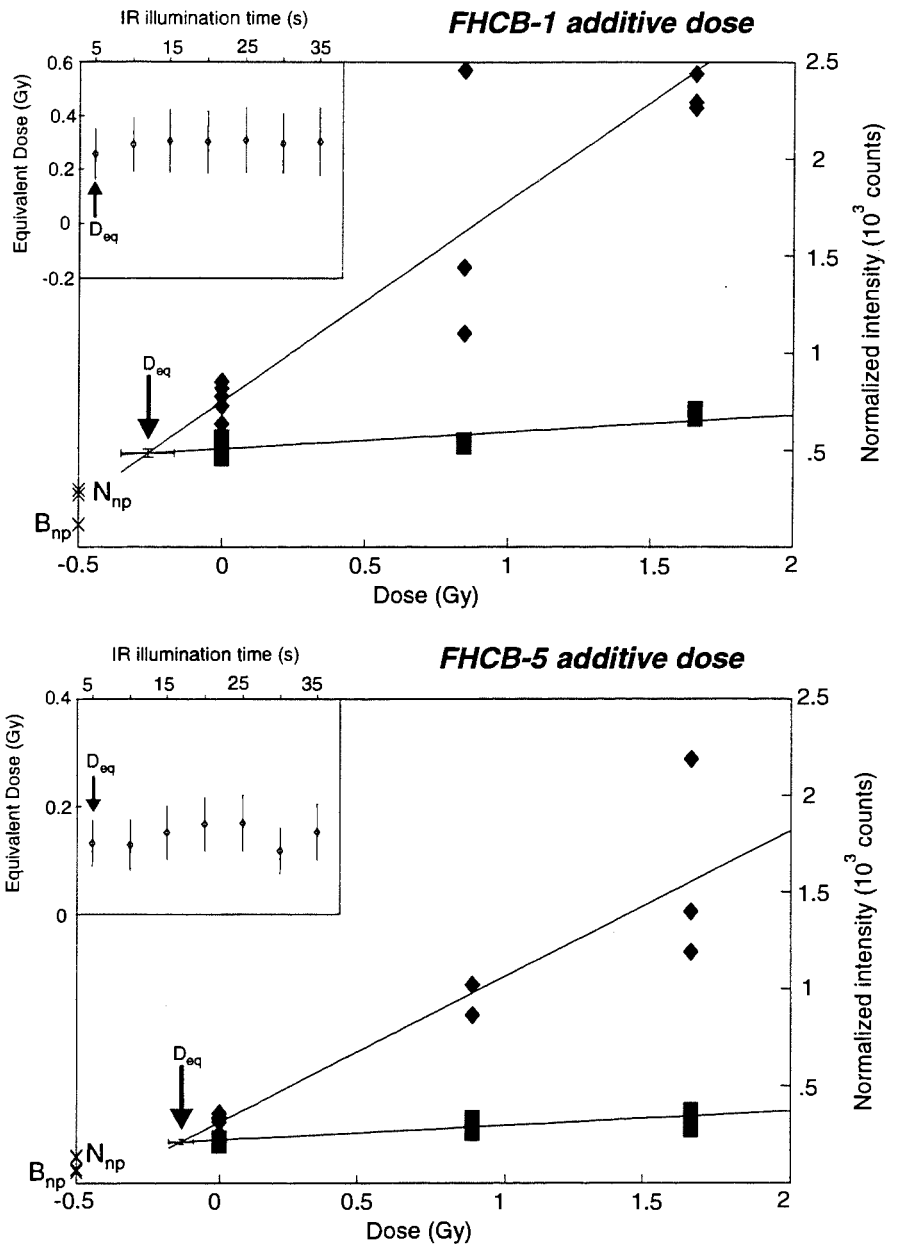

Figure 5.12: Additive dose growth curves for FHCB-1 (*top*) and FHCB-5 (*bottom*). FHCB-1 corresponds to the sand at 10–12 cm depth while FHCB-5 is the sand at 0–2 cm depth. The main plots show the intensity integrated over the first 5 seconds of diode illumination, D_{eq} is the equivalent dose. Insets show the variation of the D_{eq} with time along the luminescence decay curve. Diamonds represent the dosed aliquots, squares are the dose+bleached aliquots. N_{np} and B_{np} are the unpreheated natural and bleached samples respectively. Aliquots were normalized by mass due to the low count rates of the natural aliquots.

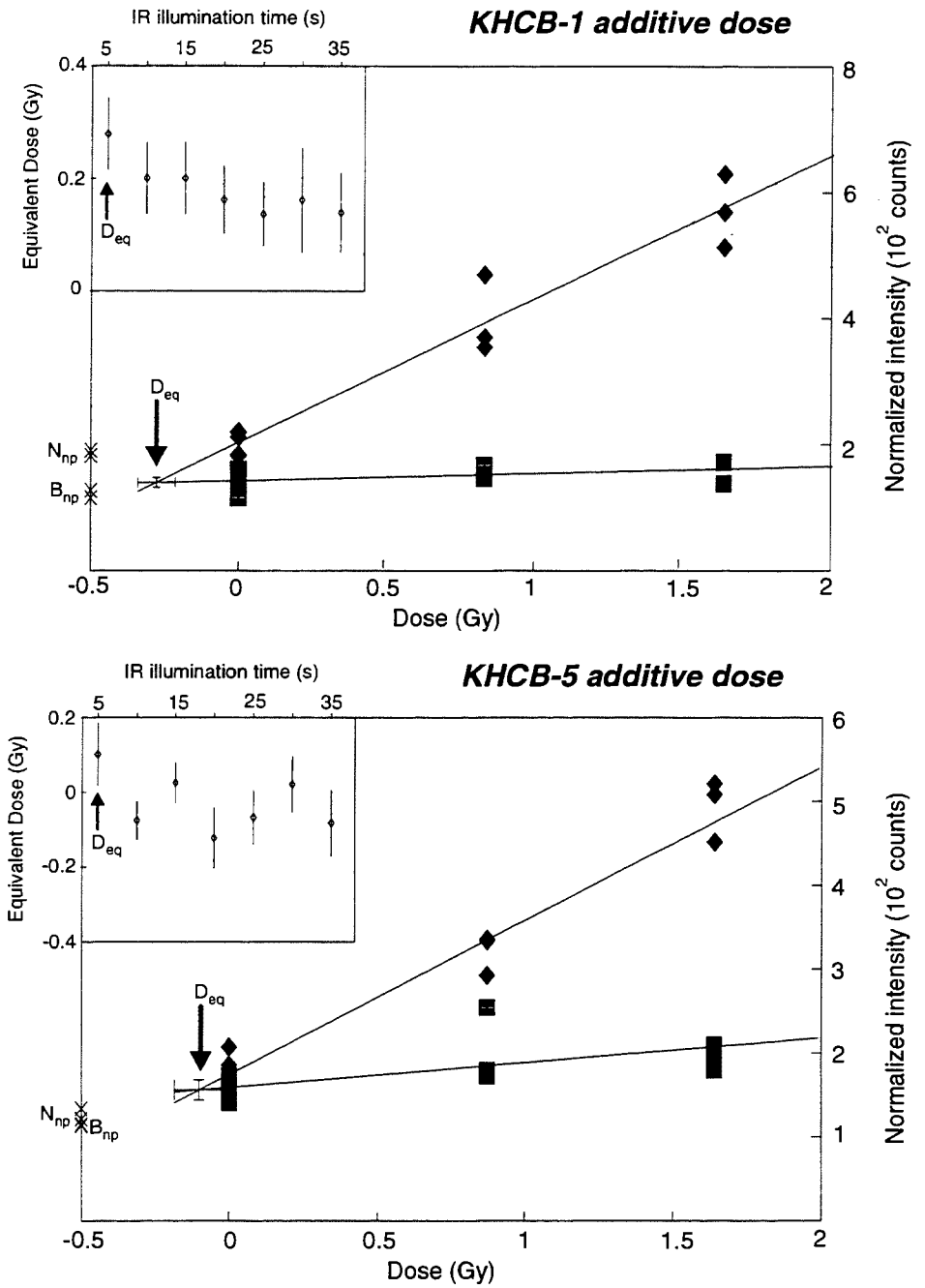

Figure 5.13: Additive dose growth curves for KHCB-1 (*top*) and KHCB-5 (*bottom*). KHCB-1 corresponds to the sand at 10–12 cm depth while KHCB-5 is the sand at 0–2 cm depth. See Figure 5.12 for an explanation of the symbols used.

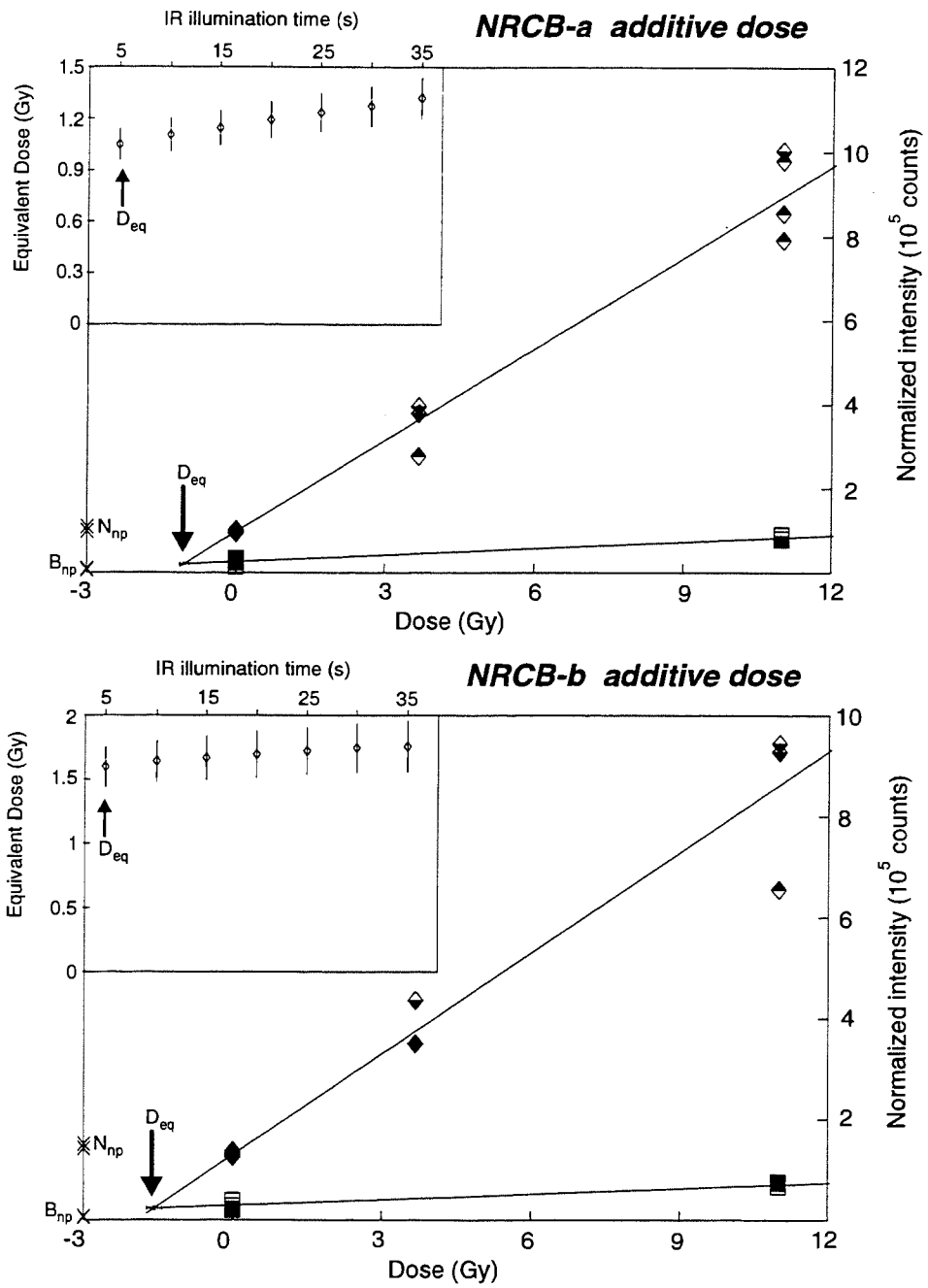

Figure 5.14: Additive dose growth curves for NRCB-a (*top*) and NRCB-b (*bottom*). NRCB-a corresponds to the sand at 0–7.5 cm depth while NRCB-b is the sand at 7.5–15 cm depth. See Figure 5.12 for an explanation of the symbols used.

luminescence decay.

How then does one determine which portion of the decay curve to use when determining a D_{eq} which accurately reflects the optical age? The goal during measurement is to select an excitation that only samples traps that were well bleached in the natural environment. If the natural bleaching is incomplete, in the sense that only the optically unstable traps were completely emptied, then a determination of the D_{eq} using the later portion of the decay curve would overestimate the age. If solar resetting was incomplete (the scatter in the N+dose data would suggest this, as we mentioned earlier), then it might be advisable to use the smallest D_{eq} (*i.e.* that obtained from the initial portion of the decay curve) as an accurate reflection of the past dose. For this reason, the D_{eq}'s used in computing the ages are those obtained from the initial portion of the luminescence decay curve.

One might ask whether the scatter in the normalized planchet intensities could be reduced by a post measurement-normalization, similar to that used for the anomalous fading data. Due to time constraints this procedure was performed only for sample KHTS-2. This sample was chosen for the particularly large scatter in its N+dose planchet intensities. As can be seen in Figure 5.8, the post-measurement normalization significantly reduced the scatter in the N+dose data. The increase in scatter in the post-normalized $N_{no\ preheat}$[4] intensities probably reflects the poor natural bleaching of the sand. By the same argument, one might expect an equivalent amount of scatter in the $N_{preheated}$[5] planchets. Curiously, this expected increase in the scatter was not observed. It is clear that this effect is related to the original preheat of the $N_{preheated}$ samples since this is the only treatment that differentiates the $N_{preheated}$ and $N_{no\ preheat}$ aliquots. However, the most significant effect of the post-normalization is to increase the level of the bleached planchet signal relative to the natural luminescence level; this results in a much smaller D_{eq} for the post-normalized data (0.10±0.04 Gy compared to 0.27±0.06 Gy) and the obtention of an age for the sample that is consistent with the known age.

Both of these discrepancies (the absence of scatter in the untreated planchets and

[4]Aliquots that received no treatment prior to measurement.

[5]Aliquots that were only subjected to a preheat before measurement.

the increase in the signal of the bleached planchet level relative to that of the untreated planchets) are difficult to resolve given our understanding of the preheating, bleaching and irradiation processes. An explanation of these results emerges on examination of the data. The natural normalization values for the untreated planchets are all lower than average: the average normalization factor for all five planchets is 0.79, but is 0.99 for the post-measurement normalization. This was to be expected from our previous explanation of low normalization values in terms of uneven bleaching of the grains. A similar increase in the normalization values is seen in the bleached aliquots, but here the effect is not as strong; the average normalization values are 0.90 and 0.95, respectively. It should also be noted that the scatter in the post-measurement normalized bleached planchets is much less than that obtained by the original normalization. The combination of all of these effects explains the increase of the bleached planchet luminescence intensities relative to those of the untreated aliquots; it is not due to the different treatments given to the bleached and untreated aliquots.

This leads to a problem of deciding which equivalent dose is correct. The only argument against the post-measurement normalization is that there is a possibility that different treatment histories affect the normalization values subsequently obtained. An example of this in the $N_{no\ preheat}$ planchets was noted earlier; the post-measurement normalization significantly increases the scatter in these aliquots relative to the natural normalization intensities. This effect, however, does not affect the equivalent dose. On the other hand, the post-measurement normalization did not appear to systematically treat the aliquots which had been given a dose and preheat differently from the aliquots which had been dosed, bleached and preheated, at least not in a way which could be explained on the basis of the original normalization values. Given the interpretation that unintended bias resulted from the original aliquot selection, there is no reason not to take the post-measurement normalized intensities as being more accurate than those obtained from the natural normalization. Thus it can be concluded that the post-measurement normalized equivalent dose provides a better estimate of the paleodose than the natual normalized value.

5.2.3 The optical ages

The optical ages calculated for the tsunami sands are tabulated in Table 5.2. The equivalent doses used in determining these ages are those obtained from the initial portion of the luminescence decay curves. An average of the D_{eq} values from the regeneration and additive dose experiments was used. All but two of the optical ages, *i.e.* those from Koprino Harbour (KHTS-1, KHTS-2), are significantly older than the true ages ages for the tsunami deposits. There appears to be little correlation between the level of solar resetting in the channel bottom sands and the accuracy of the ages obtained at a particular site. This is most evident for the Niawiakum River sample (NRTS) where the equivalent dose of the upper layers of the channel bottom mud and that of the tsunami sand are of the same magnitude. Samples ZCTS and FHTS-2 both yielded significantly older ages than the other samples; 11700±700 years and 5300±700 years, respectively. The results for each sample site are discussed separately in the following sections.

Fair Harbour (FHTS-1, 2 & 3) and Neroutsos Inlet (NITS)

The modern sand from the channel bottom at Fair Harbour yielded a non-zero equivalent dose that increases with depth. The equivalent dose for the top two centimetres of sand is 0.15±0.05 Gy whereas that for sand at 10–12 cm depth is 0.3±0.1 Gy. Tsunami samples FHTS-1 and FHTS-3 at Fair Harbour gave ages several hundred years older than expected, 900±170 years and 650±170 years, respectively, for the 300 and 32 year old layers. Solar resetting of the channel bottom sand cannot explain these anomalous ages given our hypothesis that the modern channel bottom material is analogous to the original source material for the tsunami deposits. Specifically, subtraction of the D_{eq} obtained for the deepest section of channel bottom sand (0.3±0.1 Gy) from the D_{eq} for FHTS-1 yields an age of 830±150 years. This age "corrected" for the incomplete solar resetting of the source sand still exceeds the expected age by several hundred years. This indicates that either the tsunami sands were not sourced from the channel-bottoms or that the depth of scour exceeded 10–12 cm.

Table 5.2: Dose rates, equivalent doses and optical ages for the tsunami sands. The data of Huntley and Clague (1996) (marked by a †) are included for comparison. Results from post-normalized data are marked by a ‡. All ages are calendar years before AD 1996 and were determined using the combined regeneration (Reg.) and additive dose (a.d.) D_{eq}'s. Errors are quoted at 1 σ.

Sample	Dose rate (Gy/ka)	D_{eq} (Gy) a.d.	Reg.	Age (ka)	Geological estimate (ka)
"Tsunami"					
FHTS-1	2.44±0.12	2.4±0.3	2.0±0.2	0.92±0.17	0.3
FHTS-2	1.81±0.12	9.8±1	8.5±0.7	5.3±0.7	<0.5
FHTS-3	1.82±0.10	1.4±0.03	1.0±0.1	0.65±0.17	32
KHTS-1	1.85±0.10	0.53±0.08	0.47±0.05	.27±0.05	300
KHTS-2	2.04±0.11	0.27±0.06	0.24±0.05	0.12±0.04	32
‡ KHTS-2		0.10±0.04	0.16±0.03	0.60±0.02	32
NITS	1.21±0.03	3.2±0.6	2.3±0.4	2.1±0.5	300
NRTS	2.46±0.09	1.3±0.2	1.3±0.1	0.54±0.09	300
ZCTS	1.69±0.05	20±1	20±1	11.7±0.7	300
† PATS1	1.84±0.11	0.62±0.07	—	0.360±0.045	300
† TTS	1.76±0.07	0.50±0.02	—	0.26±0.02	300
† TTS3	1.74±0.06	0.57±0.02	—	0.325±0.025	300
† CBTS2	1.59±0.06	2.1±0.1	—	1.3±0.1	1.0–1.1
Modern					
FHCB					
0–2 cm depth		0.15±0.05			
10–12 cm depth		0.3±0.1			
KHCB					
0–2 cm depth		-0.06±0.07			
10–12 cm depth		.18±0.06			
NRCB					
0–7.5 cm depth		1.03±0.09			
7.5–15 cm depth		1.6±0.2			
†Cultus Bay					
1 cm depth		0.03±0.03			
5 cm depth		0.05±0.03			
11 cm depth		0.08±0.015			
†Tofino					
1 cm depth (TFS)		0.03±0.01			
1 cm depth (TMFS)		-0.015±0.03			

It is interesting to note that the dates for FHTS-1 and FHTS-3 are at least consistent in the sense that if one were to subtract the equivalent dose of the young, A.D. 1964 sand (FHTS-3) from that of the older sand (FHTS-1), the age for the older sand would be 410±240 years. However, this interpretation relies on the assumption that the level of solar resetting in both deposits was identical and that the depositional process, *e.g.*: depth of the tsunami scour, was similar for both events.

Sample FHTS-2, which was buried 20 cm deeper than FHTS-1, gave an age of 5300±700 years. This layer is known to be less than ~550 years old since the marsh at Fair Harbour younger than this (see Section 2.1.2). Consultation with the geologists involved in this project indicated that this sample is probably fluvial material washed out of a nearby gully[6]. No evidence of this sand layer was found elsewhere in the Fair Harbour marsh, whereas both the A.D. 1964 and 300 year old layers are widespread.

The optical age of the Neroutsos Inlet tsunami sand, 2100±500 years, is at least 1500 years older than the true age of the deposit.

Koprino Harbour (KHTS-1, KHTS-2)

The level of solar resetting of the top two centimetres of sand in the channel bottom at Koprino Harbour is nearly complete; an equivalent dose of -0.06±0.07 Gy was obtained for this sand. The sand at 10–12 cm depth gave a non-zero equivalent dose of 0.18±0.06 Gy. This is the only site where the optical ages agree with the geological estimates. KHTS-1 gave an age of 270±50 years for the 300 year old tsunami layer and the post-measurement normalized age for KHTS-2 is 60±20 years. The latter date is consistent with the interpretation that the upper sand was deposited by the tsunami of the 1964 Alaska earthquake. The equivalent dose obtained from the natural normalized data for KHTS-2 gives an anomalous age of 120±40 years.

Niawiakum River (NRTS)

The Niawiakum River sample yielded an age of 540±90 years. This was surprising given the low amount of solar resetting in the channel bottom mud found at this site;

[6]Boyd Benson, personal communication, 1996.

D_{eq} for the top 7.5 cm of mud was 1.03±0.09 Gy. The optical age for the tsunami sand is far too young if the channel bottom is the source of the material deposited by the tsunami. Specifically, the equivalent dose of the channel bottom mud is similar to that of the tsunami sand. This result suggests that the channel bottom is not the source of the tsunami deposit. It is possible that the source of the tsunami sands was further away, in Willapa Bay where the water is clearer and the solar resetting of the bottom sediments is consequently closer to complete. This possibility is supported by the fact that many diatom fossils typical of the diatoms living in the modern tidal flats of Willapa Bay are found in the tsunami sands (B. F. Atwater, written communication, 1997).

Zeballos (ZCTS)

The Zeballos sand yielded an age of 11,700±700 years, suggesting that it may consist of material deposited at the end of the last glaciation. There are no known deposits of this age within a few kilometres of Zeballos[7] which means that if the sand layer was not deposited by a tsunami, this material must have been washed down the Zeballos River, perhaps during a flood. This raises the question as to why this sediment was not reset during its few kilometres of fluvial transport.

Ditlefsen (1992) found that for suspensions of fine silt >0.05 g/l, 20 hours of sunlamp exposure only reduced the natural luminescence signal in K-feldspar by 10were placed over a silty column of water 60 cm deep. The column was illuminated with a sunlamp which gave a light intensity of 50 mW/cm^2 (the average solar intensity at the earth's surface is 65 mW/cm^2).. Berger and Luternauer (1987) have shown that the spectral irradiance at depths of 4 metres in a turbid river[8] is over 10^4 less than that at the water surface and that irradiance for wavelengths above 700 nm and below 500 nm is the most strongly attenuated. During a flood in a small river such as the Zeballos, sediment contents in the water may be expected to at least meet, if not exceed, the sediment contents typical of Berger and Lutenauer's study. Several

[7] J.J. Clague, personal communication, 1997

[8] In the mouth of the Fraser River main channel – near the end of Jetty at Steveston, British Columbia.

hours of fluvial transport may not have led to sufficient sunlight exposure to reset the source materials for the Zeballos deposit.

5.2.4 Dating the tsunami sands: the larger picture

How do we account for these unexpectedly old optical ages? Either the geological age estimates are incorrect or the level of solar resetting present at these sites is not sufficient to provide accurate optical ages. The first possibility can be ruled out given that radiocarbon ages from Fair Harbour, Neroutsos Inlet and Koprino Harbour indicate that the older tsunami layer is no older than 350 years (Benson, 1996). Furthermore, the younger sand at Fair Harbour has been dated to the period A.D. 1955–1965 by ^{137}Cs analysis (Benson, 1996).

The level of solar resetting in the modern tidal marsh channels at Fair Harbour, on the other hand, cannot entirely account for the old ages obtained at this site; the equivalent dose of the channel sand is much lower than that of the tsunami sand. Assuming a tsunami origin for the latter sand, this indicates that either the tsunami scoured the channel bottom significantly deeper than 10 cm, or that the sand was derived from sediment farther out in the inlet where the water is deeper and the solar resetting is correspondingly weaker. At the other extreme, the channel-bottom mud at the Niawiakum River shows very little solar resetting whereas the tsunami sand appears to have received a more complete "zeroing" prior to deposition (*i.e.* equivalent doses of the channel bottom mud and the tsunami sand are of the same magnitude). It is also noteworthy that the modern channel bottom sands at Fair Harbour and Koprino Harbour have similar equivalent doses at the same depth, but the optical ages of the tsunami layers differ considerably[9].

In short, there appears to be little correlation between the level of solar resetting of channel-bottom material and the optical ages of the tsunami deposits. This might indicate that the hypothesis that the channel floor is the source of the tsunami sands is incorrect and that these sands were scoured from sediment farther out in the inlet.

[9]Although channel-bottom D_{eq}'s at Fair Harbour are slightly larger than those at Koprino Harbour, this is not significant considering the magnitude of the uncertainties involved.

This certainly appears to have been the case at the Niawiakum River; the channel bottom material here is too poorly bleached to have been the source of the tsunami deposit. The other possible source for the tsunami sands at this site is in the extensive tidal shallows in Willapa Bay at the mouth of the Niawiakum River. The lower turbidity of the water in these shallows could result in a greater level of solar bleaching in the bay bottom sediments than in the river bottom. The anomalously old optical age for NRTS may indicate that the level of solar resetting of the bay sediments is marginal and/or that the tsunami sand consists of a mixture of "optically old" and new grains derived from the river bottom as well as farther out in the bay.

With this last possibility in mind, the following correlation between the geomorphologic setting of the sample sites and the apparent reliability of the dates of the optical ages is noted. Sites that have yielded accurate ages have marshes that are bordered by extensive mud flats (Koprino Harbour, Tofino, Port Alberni and Cultus Bay)[10], whereas sites such as Fair Harbour and Port Alice do not have extensive mud flats. At these latter locations water depths increase rapidly at the edge of the marsh. It is possible that the sediment in deeper water near these sites is not sufficiently exposed to sunlight to allow accurate ages to be obtained from tsunami deposits derived from this material. Sediment eroded from the mud flats, on the other hand, is expected to be well bleached, as has been verified for the Tofino and Cultus Bay tidal flats (Huntley and Clague, 1996; see D_{eq}'s for these in Table 5.2).

This interpretation is problematic in that the erosional force of a tsunami is expected to be concentrated in the narrow and shallow tidal channels of the marsh rather than the deep inlet bottom. Furthermore, at Fair Harbour and Koprino Harbour Benson (1996) finds that the tsunami sands thin and fine away from the tidal channels. This indicates that most of the sand in the deposits was scoured from the channels rather than deep in the inlet.

One possibility which accounts for the discrepancy between the optical ages at Fair Harbour and Koprino Harbour is the possible attenuation of the 300 year old tsunami towards the north. Benson (1996) noted that the sand sheet at Fair Harbour was thicker (2 cm on average) than at Koprino Harbour (0.5 cm on average) – Fair

[10]See Huntley and Clague (1996) for a description of the last three sites.

Harbour being the southernmost of the two sites. If the depth of tsunami scour during the 300 year old event was deeper at Fair Harbour, then it is possible that the 300-year-old sand layer contained sand which had not received sufficient light exposure before deposition.

This argument does not, however, withstand scrutiny. It does not explain the discrepancy between the optical ages of the A.D. 1964 sand layers at these two sites, the deposits being roughly of the same thickness. This argument also fails to explain the old optical age at Neroutsos Inlet. The marsh at this site is 50 km inland from Koprino Harbour along Quatsino Sound and Neroutsos Inlet. It must be borne in mind that comparisons of tsunami bores based on tsunami deposit thickness at far removed sites are of limited validity. Tsunami propagation depends strongly on local geography, so that proximity of a marsh to the open ocean does not necessarily imply greater erosional force or deposit thicknesses.

Chapter 6

Conclusion

This study has shown that optical dating of tsunami deposits is not as straightforward as one might have hoped. The key assumption that near-to-complete solar bleaching of the luminescence was present in the source materials did not hold for two of the study sites, Fair Harbour and Neroutsos Inlet. These sites yielded optical ages that are several hundred years older than radiocarbon estimates. One of the Fair Harbour samples, FHTS-2, was not a tsunami deposit, as was thought when it was collected. The optical age for the Zeballos sample, ZCTS, suggests that it was derived some sediments deposited near the end of the last glaciation. Only one site, Koprino Harbour, gave optical ages that agree with expectations. At the 2σ limit, the optical age of the Niawiakum River deposit also comes close to its expected age.

If we include the sites from Huntley and Clague's (1996) pilot study, we have the following list of sites at which satisfactory optical ages have been obtained: Cultus Bay, Port Alberni, Tofino and Koprino Harbour. Sites that did not yield the expected ages are Fair Harbour, Neroutsos Inlet and Niawiakum River. The differences in optical ages obtained for these two groups of sites may be correlated to their different geomorphology. Specifically, sites from which correct optical ages were obtained are salt marshes fringed by extensive tidal flats. The sites which yielded discordant ages lack extensive tidal flats, the slope at the seaward edge of the marsh being steeper. If the tsunami sands have sources farther out in the inlet, then material at sites distinguished by shallow mud flats would be more readily bleached than at sites with a steeper seaward slope.

However, the above interpretation conflicts with Benson's (1996) observation that the sand deposits are concentrated near the tidal channels. This interpretation is also unlikely on energetic grounds; tsunami erosion is concentrated in the shallows, not in the deeper parts of the inlet. A more likely explanation for the discordant ages of the Vancouver Island sites is that the tsunami scoured the channel bottoms deeper at some sites than others. This may possibly be related to the geomorphological differences mentioned above.

The interpretation that sand was eroded from deeper water, farther out in the inlet, may be valid at the Niawiakum River. This site is geomorphologically very different from the Vancouver Island sites, being situated in a much higher energy, coastal environment. The low level of solar resetting in the channel bottom mud at the Niawiakum River cannot explain the relatively young optical age obtained for the ca. 300-year-old tsunami sand layer. It is clear in this case that the channel bottom could not have served as a significant source of material in the tsunami deposit. The only other possible source for the tsunami sand is further out in Willapa Bay, which contains extensive shallows and mud flats which are exposed at low tide; here it is likely that the bleaching of the sediments is closer to complete.

The use of the natural aliquot intensities for normalization, the customary practice in the past, may need re-evaluation for dating young, poorly bleached samples. The natural normalization does not accurately reflect the luminescence-producing sensitivity of the aliquots due to the admixture of optically young and old grains in the sample. In young samples this produces a pronounced scatter in the normalized luminescence intensities. Use of a post-measurement normalization technique on a young (30 year old) sample led to a significant decrease in the scatter of the aliquot luminescence intensities when compared to the "natural" normalized data. The main objection to the post-normalization procedure is the possibility that there might be a systematic change in the luminescence-producing sensitivity among groups of aliquots with different treatment histories. Results for KHTS-2 do not suggest that such a sensitivity change occurred in our post-normalized aliquots. A careful study of the effects of repeated exposure of the aliquots to a radiation dose, bleaching and preheating is required to determine the validity of the post-normalization procedure.

Further research directions

In the course of this project several ideas for future research have arisen which, although not immediately relevant to the project at hand, would improve our understanding of the photo-excited luminescence mechanism and hopefully lead to improvements in optical dating techniques. An investigation of the temperature dependence of the photo-excited luminescence over a wide range of temperatures and excitation energies (possibly using a bleaching experiment similar to Bailiff and Poolton's, 1991) would help elucidate the difference between the "optical" and "thermal" traps discussed in Section 1.3.1. Such an experiment may also help identify the most useful range of preheat temperatures; at present there appears to be no consensus as to which preheat temperature one should use (preheats used by different research groups range from 100° to 200°C). A systematic investigation of the effect of the bleaching spectrum on the equivalent doses obtained for young samples would also be useful, given the possibility of charge transfer from deep traps during the bleach. In particular, one might be justified in using a bleach spectrum similar to that of the excitation spectrum used during the measurement (*i.e.* during the bleach one would only empty the traps which are subsequently sampled by the excitation photons). Finally, the development of an empirical model that takes into account the different types of traps, defined in terms of their response to different types of treatment, is required to justify the use of the thermal transfer correction. Even a crude model neglecting the details of the trapping/de-trapping mechanism would be useful at this stage, if only to clarify the assumptions behind the use of this correction.

Appendix

Grain size effects in the α dose rate

The rate $\dot{L}$ at which α track length is produced per unit volume in a thick sample may be expressed as,

$$\dot{L} = \sum_i A_i R_i \rho \tag{6.1}$$

where the sum is over the contributing α emitting radionuclides, A_i is the specific α activity of the i^{th} radionuclide, R_i is the average α range and ρ is the density. Combining this equation with Equation 4.7, the track length generation rate may be expressed in terms of the TSAC count rate as,

$$\dot{L} = 4\lambda \tag{6.2}$$

In a large grain, edge effects may be ignored so that the previous expression for $\dot{L}$ is the relevant one for internal dose. However, if the range approaches the size of the grain the α self dose will be significantly lower; in this case a large fraction of the internally generated track length is outside the grain. A correction for this effect may be applied for a given grain geometry. However, even for the simplest grain shape (a sphere) the calculation of this correction factor proves to be complicated. A more practical approach to this problem is to use a Monte-Carlo routine to statistically determine the ratio of track length in the grain to the total track length produced by the grain.

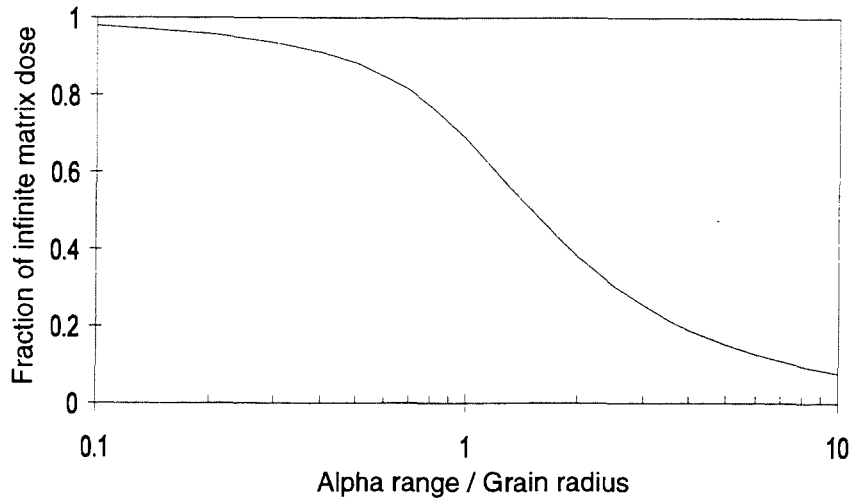

Figure 6.1: Self α track length generation rate $\dot{L}$ for a spherical grain as a function of the fraction of the α range over the grain radius. $\dot{L}$ is expressed as the fraction of the track length generation rate for a sample of infinite extent.

The procedure used was to select a random point within the grain, choose a ranodom direction from this point and, compute the distance along this direction to the edge of the grain. If the distance to the edge of the grain was larger than the range, then the track length was simply the range; otherwise the deposited track length was the distance along the track to the edge of the grain. This procedure was repeated for several points and random directions until a statistically accurate ratio of the track length within the grain to the total track length was obtained. This technique has the advantage of being easily applied to arbitrary grain geometries with very little computational difficulty.

The results of computations for spherical grains are shown in Figure 6.1 and show that edge effects are almost negligable for large grains as anticipated. For example, a grain size of 100 μm diameter with an average alpha range of 25 μm would have a value of $\dot{L}$ (internal α) lower than the large grain rate by 7%. Expressing the track

length fraction as $\Gamma(\bar{R})$[1], where $\bar{R}$ is the average α range, the equivalent gamma dose rate $D_{\alpha\rightarrow\gamma}$, in terms of the measured TSAC rate λ, is,

$$\dot{D}_{\alpha\rightarrow\gamma} = \lambda b \Gamma(\bar{R}) \tag{6.3}$$

The bulk of the α dose delivered to the grain from *external* radiation occurs within a thin surficial layer of the order of the α range. If the surface of the grain is etched away then a significant portion of this layer may be removed and the contribution of the external α dose rate may be neglected. Therefore a portion of the material that received the external alpha dose is lost during the HF etch of the feldspar grains.

The error introduced by neglecting the external α contribution altogether may be easily estimated given $\Gamma(\bar{R})$. $\Gamma(\bar{R})$ represents the fraction of the track length within the grain (due to the grain) to that deposited in an equal volume of material of infinite extent. If the grain were embedded in a much larger volume of similarly active material then $\Gamma(\bar{R})$ would be 1. By superposition the fraction of the track length deposited in the grain *due to external α's* to that in an equal volume of thick external material is simply, $1 - \Gamma(\bar{R})$. For a 100 μm grain and an α range of 25 μm, the dose fraction would be 8%. For this reason, the external α dose rate was ignored in the dose rate calculations for the samples.

[1]The correction factor that is used must be that for the average α range in order to relate the TSAC rate to the track deposition rate; this approximation is insignificant in practice.

References

Adams, J. (1990). Paleoseismicity of the Cascadia subduction zone: Evidence from turbidites off the Oregon–Washington margin. *Tectonics*, 9:569–583.

Aitken, M. J. (1985). *Thermoluminescence Dating.* Academic Press, London.

Aitken, M. J. (1994). Optical dating: a non-specialist review. *Quaternary Science Reviews*, 13(5/7):503.

Aitken, M. J. and Xie, J. (1992). Optical dating using infrared diodes: young samples. *Quaternary Science Reviews*, 11:147–152.

Atwater, B. F. (1987). Evidence for great Holocene earthquakes along the outer coast of Washington State. *Science*, 236:942–944.

Atwater, B. F. (1992). Geologic evidence for earthquakes during the past 2000 years along the Copalis River, southern Coastal Washington. *Journal of Geophysical Research*, 97:1901–1919.

Atwater, B. F. and Moore, A. L. (1992). A tsunami about 1000 years ago in Puget Sound, Washington. *Science*, 258:1614–1617.

Atwater, B. F., Nelson, A. R., Clague, J. J., Carver, G. A., Yamaguchi, D. K., Bobrowsky, P. T., Bourgeois, J., Darienzo, M. E., Grant, W. C., Hemphill-Haley, E., Kelsey, H. M., Jacoby, G. C., Nishenko, S. P., Palmer, S. P., Peterson, C. D., and Reinhart, M. A. (1995). Summary of coastal geologic evidence for past great earthquakes at the Cascadia subduction zone. *Earthquake Spectra*, 11(1):1–18.

Atwater, B. F., West, D. O., and McCrumb, D. R. (1988). Comment and reply on "Coastline uplift in Oregon and Washington and the nature of Cascadia subduction-zone tectonics". *Geology*, 16:952–953.

Atwater, B. F. and Yamaguchi, D. K. (1991). Sudden, probably coseismic submergence of trees and grass in coastal Washington State. *Geology*, 19:706–709.

Bailiff, I. K. and Poolton, N. R. J. (1991). Studies of charge transfer mechanisms in feldspars. *Nuclear Tracks and Radiation Measurements*, 18(1/2):111–118.

Benson, B. E. (1996). The stratigraphy and neo-tectonic significance of tsunami deposits beneath tidal marshes on Vancouver Island, B.C. Master's thesis, University of British Columbia.

Berger, G. W. and Luternauer, J. L. (1987). Preliminary fieldwork for thermoluminescence dating studies at the Fraser River delta, British Columbia. *Current Research, Part A, Geological Society of Canada*, Paper 87-1A:901–904.

Berger, G. W., Pillans, P. J., and Palmer, A. S. (1992). Dating loess up to 800 ka by thermoluminescence. *Geology*, 20:403–406.

Bucknam, R. C., Hemphill-Haley, E., and Leopold, E. B. (1992). Abrupt uplift within the past 1700 years at southern Puget Sound, Washington. *Science*, 258:1611–1614.

Clague, J., Harper, J. R., Hebda, R., and Howes, D. (1982). Late quaternary sea levels and crustal movements, coastal British Columbia. *Canadian Journal of Earth Sciences*, 19:597–618.

Clague, J. J. (1995). Early historical and ethnographical accounts of large earthquakes and tsunamis on western Vancouver Island, British Columbia. *Current Research 1995-A; Geological Society of Canada*, pages 47–50.

Clague, J. J. and Bobrowsky, P. T. (1994). Evidence for a large earthquake and tsunami 100–400 years ago on western Vancouver Island, British Columbia. *Quaternary Research*, 41:176–184.

Clague, J. J., Bobrowsky, P. T., and Hamilton, T. (1994). A sand sheet deposited by the 1964 Alaska tsunami at Port Alberni, British Columbia. *Estuarine, Coastal and Shelf Science*, 38:413–421.

Clarke, S. H. and Carver, G. A. (1992). Late holocene tectonics and paleoseismicity, southern Cascadia subduction zone. *Science*, 255:188–192.

Darienzo, M. E. and Peterson, C. D. (1990). Episodic tectonic subsidence of late holocene salt marshes, northern Oregon, central Cascadia margin. *Science*, 255:188–192.

Deer, W. A., Howie, R. A., and Zussman, J. (1973). *An introduction to the rock forming minerals.* Wiley, New York.

Ditlefsen, C. (1992). Bleaching of K-feldspars in turbid water suspensions: a comparison of photo- and thermoluminescence signals. *Quaternary Science Reviews*, 11:33–38.

Ditlefsen, C. and Huntley, D. J. (1994). Optical excitation of trapped charges in quartz, potassium feldspars and mixed silicates: The dependence on photon energy. *Radiation Measurements*, 23(4):675–682.

Dragert, H. and Hyndman, R. D. (1995). Continuous GPS monitoring of elastic strain in the northern Cascadia subduction zone. *Geophysical Research Letters*, 22(7):755–758.

Duller, G. A. T. (1994). Luminescence dating of poorly bleached sediments from Scotland. *Quaternary Science Reviews*, 13:521–524.

Faure, G. (1991). *Principles and Applications of Inorganic Geochemistry.* MacMillan, New York.

Friele, P. A. and Hutchinson, I. (1993). Holocene sea-level change on the central west coast of Vancouver island, British Columbia. *Canadian Journal of Earth Sciences*, 30:832–840.

Fuller, I. C., Wintle, A. G., and Duller, G. A. T. (1994). Test of the partial bleach methodology as applied to the infra-red stimulated luminescence of an alluvial sediment from the Danube. *Quaternary Science Reviews*, 13:539–543.

Godfrey-Smith, D. I., Huntley, D. J., and Chen, W.-H. (1988). Optical dating studies of quartz and feldspar sediment extracts. *Quaternary Science Reviews*, 7:373–380.

Guilbault, J.-P., Clague, J. J., and Lapointe, M. (1995). Amount of subsidence during a late Holocene earthquake — evidence from fossil tidal marsh foraminifera at Vancouver Island, west coast of Canada. *Palaeogeography, Palaeoclimatology, Palaeoecology*, 118:49–71.

Guilbault, J.-P., Clague, J. J., and Lapointe, M. (1996). Foraminiferal evidence for the amount of coseismic subsidence during a late holocene earthquake on Vancouver Island, west coast of Canada. *Quaternary Science Reviews*, 15:913–937.

Heaton, T. H., Snavely, P. D., and Jr (1985). Possible tsunami along the northwestern coast of the United States inferred from Indian traditions. *Bulletin of the Seismological Society of America*, 75(5):1455–1460.

Huntley, D. J. and Berger, G. W. (1995). Scatter in luminescence data for optical dating – some models. *Ancient TL*, 13:5–9.

Huntley, D. J., Berger, G. W., and Bowman, S. G. E. (1988). Thermoluminescence responses to alpha and beta irradiations, and age determination when the high dose response is nonlinear. *Radiation Effects*, 105:279–284.

Huntley, D. J. and Clague, J. J. (1996). Optical dating of tsunami-laid sands. *Quaternary Research*, 46:127–140.

Huntley, D. J., Godfrey-Smith, D. I., and Thewalt, M. L. W. (1985). Optical dating of sediments. *Nature*, 313(5998):105–107.

Huntley, D. J., Hutton, J. T., and Prescott, J. R. (1993a). Optical dating using inclusions within quartz grains. *Geology*, 21:1087–1090.

Huntley, D. J., Hutton, J. T., and Prescott, J. R. (1993b). The stranded beach-dune sequence of south-east South Australia: a test of thermoluminescence dating, 0-800 ka. *Quaternary Science Reviews*, 12:1–20.

Hütt, G., Jaek, I., and Tchonka, J. (1988). Optical dating: K-feldspars optical response stimulation spectra. *Quaternary Science Reviews*, 7:381–385.

Hyndman, R. D. and Wang, K. (1993). Thermal constraints on the zone of major thrust earthquake failure: The Cascadia subduction zone. *Journal of Geophysical Research*, 98(B2):2039–2060.

Hyndman, R. D. and Wang, K. (1995). The rupture zone of Cascadia great earthquakes from current deformation and thermal regime. *Journal of Geophysical Research*, 100(B11):22133–22154.

Jacoby, G. C., Williams, P. L., and Buckley, B. M. (1992). Tree ring correlation between prehistoric landslides and abrupt tectonic events in Seattle, Washington. *Science*, 258:1621–1623.

Lang, A. (1994). Infra-red stimulated luminescence dating of holocene reworked silty sediments. *Quaternary Science Reviews*, 13:525–528.

Li, S.-H. (1994). Optical dating; insufficiently bleached sediments. *Radiation Measurements*, 23(2/3):563–567.

Li, S.-H. and Wintle, A. G. (1992). A global view of the stability of luminescence signals from loess. *Quaternary Science Reviews*, 11:133–137.

Lian, O. B., Hu, J., Huntley, D. J., and Hicock, S. R. (1995). Optical dating studies of Quaternary organic-rich sediments from southwestern British Columbia and northwestern Washington State. *Canadian Journal of Earth Sciences*, 32:1194–1207.

Mathewes, R. W. and Clague, J. J. (1994). Detection of large prehistoric earthquakes in the Pacific northwest by microfossil analysis. *Science*, 264:688–691.

Mejdahl, V. (1979). Thermoluminescence dating: beta-dose attenuation in quartz grains. *Archaeometry*, 21:61–72.

Mitchell, C. E., Vincent, P., Weldon II, R. J., and Richards, M. A. (1994). Present-day vertical deformation of the Cascadia margin, Pacific Northwest, United States. *Journal of Geophysical Research*, 99(B6):12257–12277.

Mott, N. F. and Gurney, R. W. (1948). *Electronic processes in ionic crystals.* Oxford University Press, London, second edition, pp 160-162.

Musson, F. M. and Wintle, A. G. (1994). Luminescence dating of the loess profile at Dolní Vestonice, Czech Republic. *Quaternary Science Reviews*, 13:411–416.

Nambi, K. S. V. and Aitken, M. J. (1986). Annual dose conversion factors for TL and ESR dating. *Archaeometry*, 28(2):202–205.

Nelson, A. R. (1992). Discordant ^{14}C ages from buried tidal-marsh soils in the Cascadia subduction zone, southern Oregon coast. *Quaternary Research*, 38:74–90.

Nelson, A. R., Atwater, B. F., Bobrowsky, P. T., Bradley, L.-A., Clague, J. J., Carver, G. A., Darienzo, M. E., Grant, W. C., Krueger, H. W., Sparks, R., Stafford, Jr., T. W., and Stuiver, M. (1995). Radiocarbon evidence for extensive plate-boundary rupture about 300 years ago at the Cascadia subduction zone. *Nature*, 378:371–374.

Ollerhead, J., Huntley, D. J., and Berger, G. W. (1994). Luminescence dating of sediments from Buctouche Spit, New Brunswick. *Canadian Journal of Earth Sciences*, 31:523–531.

Parkhomenko, E. I. (1967). *Electrical properties of rocks.* Plenum Press, New York.

Prescott, J. R. and Fox, P. J. (1993). Three-dimensional thermoluminescence spectra of feldspars. *Journal of Physics D: Applied Physics*, 26:2245–2254.

Prescott, J. R. and Hutton, J. T. (1988). Cosmic ray and gamma ray dosimetry for TL and ESR. *Nuclear Tracks and Radiation Measurements*, 14(1/2):223–227.

Prescott, J. R. and Stephan, L. G. (1982). The contribution of cosmic radiation to the environmental dose for thermoluminescence dating: latitude, altitude and depth dependences. In *PACT 6*, Second specialist seminar on thermoluminescence dating, Oxford.

Reinhart, M. A. and Bourgeois, J. (1989). Tsunami favored over storm or seiche for sand deposit overlying buried Holocene peat, Willapa Bay, Washington [abs.]. *EOS (Transactions, Americain Geophysical Union)*, 70:1331.

Rendell, H., Webster, S., and Sheffer, N. (1994). Underwater bleaching of signals from sediment grains: new experimental data. *Quaternary Geochronology*, 13:433–435.

Satake, K., Shimazaki, K., Tsuji, Y., and Ueda, K. (1996). Time and size of a giant earthquake in Cascadia inferred from Japanese tsunami records of January 1700. *Nature*, 379:246–249.

Savage, J. C. and Lisowski, M. (1991). Strain measurements and the potential for a great subduction earthquake off the coast of Washington. *Science*, 252:101–103.

Schuster, R. L., Logan, R. L., and Pringle, P. T. (1992). Prehistoric rock avalanches in the Olympic Mountains, Washington. *Science*, 258:1620–1621.

Shennan, I., Long, A., Rutherford, M., Green, F., Innes, J., Lloyd, J., Zong, Y., and Walker, K. (1996). Tidal marsh stratigraphy, sea-level change and large earthquakes, I: A 5000 year record in Washington, U.S.A. *Quaternary Science Reviews*, 15:1023–1059.

Spooner, N. A. (1992). Optical dating: preliminary results on the anomalous fading of luminescence from feldspars. *Quaternary Science Reviews*, 11:139–145.

Spooner, N. A. (1993). *The validity of optical dating based on feldspar.* D. Phil. thesis, Linacre College, Oxford.

Spooner, N. A. (1994). The anomalous fading of infrared-stimulated luminescence from feldspars. *Radiation Measurements*, 23(2/3):625–632.

Sproat, G. M. (1987). *The Nootka: scenes and studies of savage life.* Sono Nis Press, Victoria, British Columbia.

Welford, W. T. and Winston, R. (1989). *High Collection Nonimaging Optics.* Academic Press, Inc.

Wells, D. R. and Coppersmith, K. J. (1994). New empirical relationships among magnitude, rupture length, rupture width, rupture area and surface displacement. *Bulletin of the Seismological Society of America*, 84:974–1002.

West, D. O. and McCrumb, D. R. (1988). Coastline uplift in Oregon and Washington and the nature of Cascadia subduction-zone tectonics. *Geology*, 16:169–172.

Wolfe, S. A., Huntley, D. J., and Ollerhead, J. (1995). Recent and late Holocene sand dune activity in southwestern Saskatchewan. *Current Research 1995-B; Geological Survey of Canada*, pages 131–140.